



**HAL**  
open science

# Descente en échelle de la ressource en énergie éolienne de la mésoéchelle à l'échelle locale par imbrication et assimilation de données à l'aide d'un modèle de CFD

Venkatesh Duraisamy Jothiprakasham

► **To cite this version:**

Venkatesh Duraisamy Jothiprakasham. Descente en échelle de la ressource en énergie éolienne de la mésoéchelle à l'échelle locale par imbrication et assimilation de données à l'aide d'un modèle de CFD. Sciences de l'environnement. Université Paris-Est, 2014. Français. NNT : 2014PEST1017 . tel-01124275

**HAL Id: tel-01124275**

**<https://pastel.hal.science/tel-01124275>**

Submitted on 6 Mar 2015

**HAL** is a multi-disciplinary open access archive for the deposit and dissemination of scientific research documents, whether they are published or not. The documents may come from teaching and research institutions in France or abroad, or from public or private research centers.

L'archive ouverte pluridisciplinaire **HAL**, est destinée au dépôt et à la diffusion de documents scientifiques de niveau recherche, publiés ou non, émanant des établissements d'enseignement et de recherche français ou étrangers, des laboratoires publics ou privés.



ÉCOLE DES PONTS PARISTECH / UNIVERSITÉ PARIS-EST

# PHD THESIS

to obtain the title of

## PhD of the University of Paris-Est

**Specialty: SCIENCE, ENGINEERING AND ENVIRONMENT**

Defended by

Venkatesh DURAISAMY JOTHIPRAKASAM

# Downscaling wind energy resource from mesocale to local scale by nesting and data assimilation with a CFD model

Date of defense: 14<sup>th</sup> May 2014

### Jury

President / Reviewer:	Pr. François CAUNEAU	École des Mines de Paris
Reviewer:	Pr. Jeroen VAN BEECK	The Von Karman Institute for Fluid Dynamics
Examiner:	Dr. Javier SANZ RODRIGO	CENER
Advisor:	Dr. Bertrand CARISSIMO	CEREA
Co-advisor:	Dr. Eric DUPONT	CEREA



## **Acknowledgement**

This research work was performed in the framework of FP7/ITN Marie Curie WAUDIT project. It's a consortium, which aims at developing new methodologies of added value to the wind industry, such that they can contribute to new levels of standardization of wind assessment activities. I thank Javier Sanz Rodrigo for successfully organizing and completing the project.

I would like to express my gratitude to my advisors, Eric Dupont and Bertrand Carissimo for their suggestion and guidance in completing the PhD thesis. I would like to express my sincere gratitude to François Cauneau, Jeroen Van Beeck and Javier Sanz Rodrigo who took their precious time off from their tight schedule to be reviewer and been part of the jury. I am greatly indebted to Denis Wendum, Maya Milliez, Cédric Dall'ozzo, Yongfeng Qu, Raphaël Bresson and Hanane Zaïdi for their many helpful suggestions, comments and technical assistance.

I would like to thank Luc Musson-Genon and Christian Seigneur for hosting me in CEREAs. I am grateful to MFEE department of EDF R&D for hosting me in Chatou and providing technical facilities during my stay. Also I would to thanks to Paris-Est University and Doctoral school for their kind support during my stay.

Special thanks goes to my friends and colleagues who have supported me throughout my research: George Fitton, Hubert Baya Toda, Raghu Krishna, Maxime Fortin, Virginie Hergault, Marie Garo, Johnathan Compaore, Xiao Wei, Noëlie Daviau-Pellegrin, Sébastien Rozborski and many others.



**I would like to dedicate this thesis to my family**



## **Abstract**

The development of wind energy generation requires precise and well-established methods for wind resource assessment, which is the initial step in every wind farm project. During the last two decades linear flow models were widely used in the wind industry for wind resource assessment and micro-siting. But the linear models inaccuracies in predicting the wind speeds in very complex terrain are well known and led to use of CFD, capable of modeling the complex flow in details around specific geographic features. Mesoscale models (NWP) are able to predict the wind regime at resolutions of several kilometers, but are not well suited to resolve the wind speed and turbulence induced by the topography features on the scale of a few hundred meters. CFD has proven successful in capturing flow details at smaller scales, but needs an accurate specification of the inlet conditions. Thus coupling NWP and CFD models is a better modeling approach for wind energy applications.

A one-year field measurement campaign carried out in a complex terrain in southern France during 2007-2008 provides a well documented data set both for input and validation data. The proposed new methodology aims to address two problems: the high spatial variation of the topography on the domain lateral boundaries, and the prediction errors of the mesoscale model. It is applied in this work using the open source CFD code Code\_Saturne, coupled with the mesoscale forecast model of Météo-France (ALADIN). The improvement is obtained by combining the mesoscale data as inlet condition and field measurement data assimilation into the CFD model. Newtonian relaxation (nudging) data assimilation technique is used to incorporate the measurement data into the CFD simulations. The methodology to reconstruct long term averages uses a clustering process to group the similar meteorological conditions and to reduce the number of CFD simulations needed to reproduce 1 year of atmospheric flow over the site. The assimilation procedure is carried out with either sonic or cup anemometers measurements. First a detailed analysis of the results obtained with the mesoscale-CFD coupling and with or without

data assimilation is shown for two main wind directions, including a sensitivity study to the parameters involved in the coupling and in the nudging. The last part of the work is devoted to the estimate of the wind potential using clustering. A comparison of the annual mean wind speed with measurements that do not enter the assimilation process and with the WAsP model is presented. The improvement provided by the data assimilation on the distribution of differences with measurements is shown on the wind speed and direction for different configurations.

**Keywords:** Wind resource assessment, Coupling mesoscale and CFD model, Data assimilation, Complex terrain.

## Résumé

Le développement de la production d'énergie éolienne nécessite des méthodes précises et bien établies pour l'évaluation de la ressource éolienne, étape essentielle dans la phase avant-projet d'une future ferme. Au cours de ces deux dernières décennies, les modèles d'écoulements linéaires ont été largement utilisés dans l'industrie éolienne pour l'évaluation de la ressource et pour la définition de la disposition des turbines. Cependant, les incertitudes des modèles linéaires dans la prévision de la vitesse du vent sur terrain complexe sont bien connues. Elles conduisent à l'utilisation de modèles CFD, capables de modéliser les écoulements complexes de manière précise autour de caractéristiques géographiques spécifiques. Les modèles méso-échelle peuvent prédire le régime de vent à des résolutions de plusieurs kilomètres mais ne sont pas bien adaptés pour résoudre les échelles spatiales inférieures à quelques centaines de mètres. Les modèles de CFD peuvent capter les détails des écoulements atmosphériques à plus petite échelle, mais nécessitent de documenter précisément les conditions aux limites. Ainsi, le couplage entre un modèle méso-échelle et un modèle CFD doit permettre d'améliorer la modélisation fine de l'écoulement pour les applications dans le domaine de l'énergie éolienne en comparaison avec les approches opérationnelles actuelles.

Une campagne de mesure d'un an a été réalisée sur un terrain complexe dans le sud de la France durant la période 2007-2008. Elle a permis de fournir une base de données bien documentée à la fois pour les paramètres d'entrée et les données de validation. La nouvelle méthodologie proposée vise notamment à répondre à deux problématiques: le couplage entre le modèle méso-échelle et le modèle CFD en prenant en compte une forte variation spatiale de la topographie sur les bords du domaine de simulation, et les erreurs de prédiction du modèle méso-échelle. Le travail réalisé ici a consisté à optimiser le calcul du vent sur chaque face d'entrée du modèle CFD à partir des valeurs issues des verticales du modèle de méso-échelle, puis à mettre en œuvre une assimilation

de données basée sur la relaxation newtonienne (nudging). La chaîne de modèles considérée ici est composée du modèle de prévision de Météo-France ALADIN et du code de CFD open-source Code\_Saturne. Le potentiel éolien est ensuite calculé en utilisant une méthode de clustering, permettant de regrouper les conditions météorologiques similaires et ainsi réduire le nombre de simulations CFD nécessaires pour reproduire un an (ou plus) d'écoulement atmosphérique sur le site considéré. La procédure d'assimilation est réalisée avec des mesures issues d'anémomètre à coupelles ou soniques. Une analyse détaillée des simulations avec imbrication et avec ou sans assimilation de données est d'abord présentée pour les deux directions de vent dominantes, avec en particulier une étude de sensibilité aux paramètres intervenant dans l'imbrication et dans l'assimilation. La dernière partie du travail est consacrée au calcul du potentiel éolien en utilisant une méthode de clustering. La vitesse annuelle moyenne du vent est calculée avec et sans assimilation, puis est comparée avec les mesures non assimilées et les résultats du modèle WAsP. L'amélioration apportée par l'assimilation de données sur la distribution des écarts avec les mesures est ainsi quantifiée pour différentes configurations.

**Mots-clés:** Evaluation de la ressource éolienne, Couplage de modèle méso-échelle et CFD, Assimilation de données, Terrain complexe.





## Contents

<b>1. Introduction.....</b>	<b>1</b>
<b>1.1. Global Wind Energy Outlook .....</b>	<b>3</b>
<b>1.2. European Wind Energy Outlook.....</b>	<b>4</b>
<b>1.3. Nature of wind .....</b>	<b>7</b>
<b>1.4. Atmospheric Boundary Layer .....</b>	<b>10</b>
<b>1.5. Flow over Complex Terrain.....</b>	<b>12</b>
<b>1.6. Annual Energy Production of Wind farm .....</b>	<b>14</b>
<b>1.7. Objective and motivation .....</b>	<b>15</b>
<b>2. Wind Resource Assessment .....</b>	<b>18</b>
<b>2.1. Regional wind resource .....</b>	<b>18</b>
<b>2.2. Local wind resource .....</b>	<b>19</b>
<b>2.3. Types of wind flow models .....</b>	<b>22</b>
2.3.1. Conceptual models.....	22
2.3.2. Physical models.....	22
2.3.3. Statistical models.....	24
2.3.4. Numerical models.....	24
2.3.4.1. Mass-Consistent model.....	25
2.3.4.2. Jackson-Hunt models.....	25
2.3.4.3. CFD modeling .....	28
2.3.4.4. Mesoscale modeling .....	37
2.3.4.5. Coupling mesoscale and microscale modeling .....	43
2.3.4.6. Coupling mesoscale and microscale model and field measurements assimilation.....	52
<b>3. Modeling procedure for coupling mesoscale and microscale models .....</b>	<b>55</b>
<b>3.1. Measurement Campaign .....</b>	<b>55</b>
3.1.1. Site description .....	55
3.1.2. Measurement campaign .....	57
3.1.3. Meteorological conditions .....	58
<b>3.2. ALADIN - Mesoscale data extraction .....</b>	<b>59</b>

<b>3.3. Coupling mesoscale and microscale models .....</b>	<b>62</b>
<b>3.4. Clustering .....</b>	<b>63</b>
<b>3.5. Microscale CFD Model .....</b>	<b>65</b>
3.5.1. Topography and domain.....	66
3.5.2. Mesh.....	69
3.5.3. <i>Code_Saturne</i> - Atmospheric Module .....	71
3.5.4. Turbulence model.....	72
3.5.5. Coupling methods - Imposing mesoscale boundary condition on microscale CFD grid .....	74
3.5.5.1. Translation .....	75
3.5.5.2. Extrapolation .....	76
3.5.5.3. Cressman interpolation .....	77
3.5.6. Data assimilation – nudging .....	79
<b>4. Results: Sensitivity and parameteric analysis.....</b>	<b>82</b>
4.1. Case description.....	82
4.2. Grid Independence .....	83
4.3. Cressman Sensitivity - Radius of influence .....	87
4.4. Coupling method - Translation, Extrapolation, Cressman interpolation	91
4.5. Data assimilation at M80 mast location.....	95
4.6. Analysis of two situations .....	107
4.6.1. Northwesterly direction .....	107
4.6.2. Southeasterly direction .....	112
<b>5. Computation of the annual average wind speed .....</b>	<b>116</b>
5.1. CFD simulations with sonic and cup anemometer assimilation.....	122
5.2. Comparisons of CFD simulation without and with assimilation on the yearly average.....	131
<b>6. Conclusion and Future work .....</b>	<b>147</b>
<b>References</b>	



## Nomenclature

### Roman Symbols

$P$	Power in the wind	$kg.m^2.s^{-3}$
$A$	Area swept by the wind turbine blade	$m^2$
$V$	Velocity at the turbine hub height	$ms^{-1}$
$u_*$	Frictional velocity	$ms^{-1}$
$C_\mu$	Turbulence model coefficient	-
$z_0$	Roughness length	$m$
$z$	Height above ground level	$m$
$g_i$	gravity	$ms^{-1}$
$P$	Pressure	$Pa$
$k$	Turbulent kinetic energy	$m^{-2}s^{-2}$
$Pr_t$	Prandtl number.	-
$V_{interpolate}$	Cressman interpolated velocity component	$ms^{-1}$
$V_i$	ALADIN velocity component for the vertical $i$	$ms^{-1}$
$W_i$	Weight functions for distance between the CFD and ALADIN grid points	-
$n_{aladin}$	Number of available ALADIN verticals	-
$r_i$	Total radius of influence	$m$
$x_{value}, y_{value}, z_{value}$	Coordinates of CFD grid point	-
$x_i, y_i, z_i$	Coordinates of ALADIN grid points	-
$r_L$	Longitudinal radius of influence	$m$
$r_Z$	Vertical radius of influence	$m$
$u_{obs}$	Observed velocity	$ms^{-1}$
$u_s$	Simulated velocity	$ms^{-1}$

$W(x, y, z, t)$	Cressman spreading function	-
$R_i$	Richardson number	-

### Greek Symbols

$\rho$	density	$kg.m^{-3}$
$\varepsilon$	dissipation rate	-
$\kappa$	von Karman constant	0.4
$\theta$	potential temperature	$K, ^\circ C$
$\tau_u$	Time scale	$s$
$\mu$	Viscosity of the fluid	$kg.m^{-1}s^{-1}$

### Acronyms

1D, 2D, 3D, 4D	One, Two, Three, Four Dimension
3DDA	Three Dimensional Data Assimilation
3D-Var	Three-Dimensional Variational Data Assimilation
4DDA	Four Dimensional Data Assimilation
ABL	Atmospheric Boundary Layer
ADM-NR	Actuator Disk Model Without rotation
ADM-R	Actuator Disk Model With Rotation
AEP	Annual Energy Prediction
ALADIN	Aire Limitée Adaptation dynamique Développement InterNational
ALM	Actuator-Line Model
AROME	Applications of Research to Operations at MESoscale
ASBM	Algebraic Structure-Based Turbulence Model
CAD	Computer Aided Design
CEREA	Centre d'Enseignement et de Recherche en Environnement Atmosphérique
CFD	Computational Fluid Dynamics

CWE	Computational Wind Engineering
DEM	Digital elevation map
DNS	Direct Numerical Simulation
EDF EN	Électricité de France - Énergies Nouvelles
EDF R&D	Électricité de France - Research and Development
EEC	European Economic Community
EU	European Union
FEM	Finite Element Method
FVM	Finite Volume Method
GW	Giga Watt
IGN	Institut Géographique National
LDA	Laser Doppler Anemometer
LES	Large Eddy Simulation
LIDAR	Light Detection and Ranging
MCEL	Model Coupling Environmental Library
MMM	Mesoscale Meteorological Model
NW	North Westerly
NWP	Numerical Weather Prediction
PBL	Planetary boundary Layer
PIV	Particle Image Velocimetry
RAMS	Regional Atmospheric Modeling System
RANS	Reynolds Averaged Navier Stokes
RIX	Ruggedness Index
RTFDDA	Real-Time Four Dimensional Data Assimilation
SGS	Subgrid-Scale model
SIMPLE	Semi-Implicit Method for Pressure-Linked Equations
SODAR	SONic Detection And Ranging
TDMA	Tridiagonal Matrix Algorithm
TKE	Turbulent Kinetic Energy
TWh	TeraWatt-Hour
URANS	Unsteady Reynolds Averaged Navier-Stokes
UTC	Coordinated Universal Time

WAsP	Wind Atlas Analysis and Application Program
WRF	Weather Research Forecast
WT	Wind Turbine



# 1. Introduction

The present thesis contributes to the scientific activities in the field of wind resource assessment research. The motivation of the thesis is application-oriented for wind energy using Numerical Weather Prediction (NWP) and Computational Fluid Dynamics (CFD) model. It is focused on improvement of wind resource assessment using coupled mesoscale and microscale CFD models and assimilating field measurements into the CFD model. Data assimilation is a NWP modeling technique and this thesis addresses the field measurement assimilation process in CFD model for near surface wind over a complex topography.

The development of wind energy generation requires precise and well-established methods for wind resource assessment, which is the initial step in every wind farm project. During the last two decades linear flow models were widely used in the wind industry for wind resource assessment and micro-siting. But the linear models inaccuracies in predicting the wind speeds in very complex terrain are well known and led to use of CFD, capable of modeling the complex flow in fine details around specific geographic features. NWP or mesoscale models use mathematical models of the atmosphere and oceans to predict the weather by assimilating observation of the current weather conditions to predict the flow characteristics and have been extensively used in weather prediction and forecasting. NWP are able to predict the wind regime at resolutions of several kilometers, and cannot resolve the wind speed and turbulence induced by the topography features finer than about 1 km. However, CFD has proven successful in capturing flow details at smaller scales. Hence combining NWP and CFD models can result in a better modeling approach for wind energy applications.

The thesis is structured into six chapters. Chapter 1 is focused on outlook of worldwide wind energy development, background of atmospheric physics,

objective and motivation of the thesis. Chapter 2 gives an overview of wind flow modeling and the basic concepts of wind resource assessment using different modeling technique: conceptual model, physical model, statistical model and numerical model. The state-of-the-art models for various numerical wind flow models used for wind resource assessment are detailed. Uncertainties of linearized flow model (WAsP) in estimating wind resource in complex terrain are depicted. The advantages of using CFD models in complex terrain and mesoscale models prediction of wind regime in large domain are explained. Very recently mesoscale and CFD models were coupled and wind speed predictions are now realistic in comparison with measurements.

Chapter 3 describes the site of application, data extraction from mesoscale model and choice of the microscale model used. It presents the modifications and improvements provided by this work compared to the methodology proposed in a previous PhD work and tested on the same site. Different coupling methods used for imposing the inlet boundaries and implementation of data assimilation technique into the CFD model are explained. Chapter 4 provides sensitivity analysis for the grid independence, the interpolation method used at inlet boundaries and implementation and validation of nudging for data assimilation. Comparisons of results for CFD simulation without assimilation and CFD simulation with assimilation are presented for 2 main wind directions of the site.

In Chapter 5, a computation of the wind potential over one year is presented, based on a selection of 64 meteorological situations using a clustering method. CFD simulation results for the 64 cluster centers without assimilation and with assimilation are presented. The annual average wind speed is calculated for CFD simulations without assimilation and with assimilation, and these results are compared with measurements, WAsP results and previous PhD work carried out at EDF R&D. Comparison of CFD simulation with assimilation results with two different data sources is shown. Conclusion and future work are explained in chapter 6.

## 1.1. Global Wind Energy Outlook

Worldwide there are now over two hundred thousand wind turbines operating, with a total installed capacity of 282 GW at the end 2012 growing by 44 GW over the preceding year (GWEC, 2012). Figure 1.1 shows the global cumulative installed wind capacity grown from 6 GW in 1996 to 282 GW in 2012. The European Union alone passed more than 100 GW installed capacity in September 2012 (EWEA, 2013) while the United States surpassed 50 GW in August 2012 and China passed 50 GW the same month (GWEC, 2012). World wind generation capacity more than quadrupled between 2000 and 2006, doubling about every three years. The United States pioneered wind farms and led the world in installed capacity in the 1980s and into the 1990s. In 1997 Germany installed capacity surpassed the U.S. and led until once again overtaken by the U.S. in 2008. China has been rapidly expanding its wind installations in the late 2000s and passed the U.S. in 2010 to become the world leader.

According to the World Wind Energy Association, an industry organization, in 2010 wind power generated 430 terawatt-hour (TWh) or about 2.5% of worldwide electricity usage (WWEA, 2011) up from 1.5% in 2008 and 0.1% in 1997. Between 2005 and 2010 the average annual growth in new installations was 27.6 percent. Wind power market penetration is expected to reach 3.35 percent by 2013 and 8 percent by 2018.

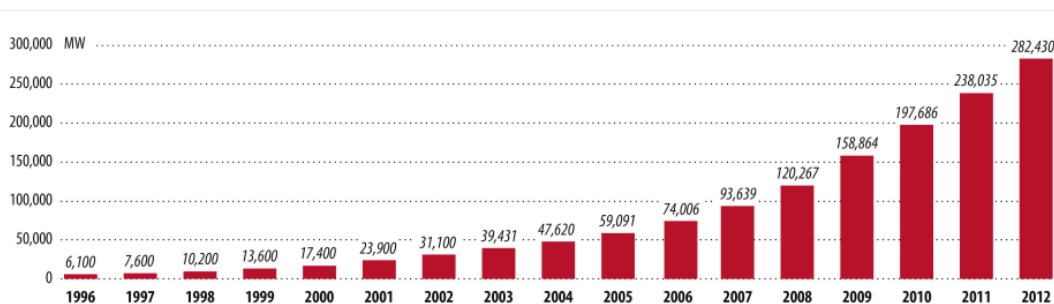


Figure 1.1: Global cumulative installed wind capacity 1996-2012, Source: GWEC

Several countries have already achieved relatively high levels of penetration, such as 28% of stationary electricity production in Denmark (2011), 19% in Portugal (2011), 16% in Spain (2011), 14% in Ireland (2010) and 8% in Germany (2011). As of 2011, 83 countries around the world were using wind power on a commercial basis. Figure 1.2 gives the world top 10 countries share of total installed wind capacity at the end of 2012.

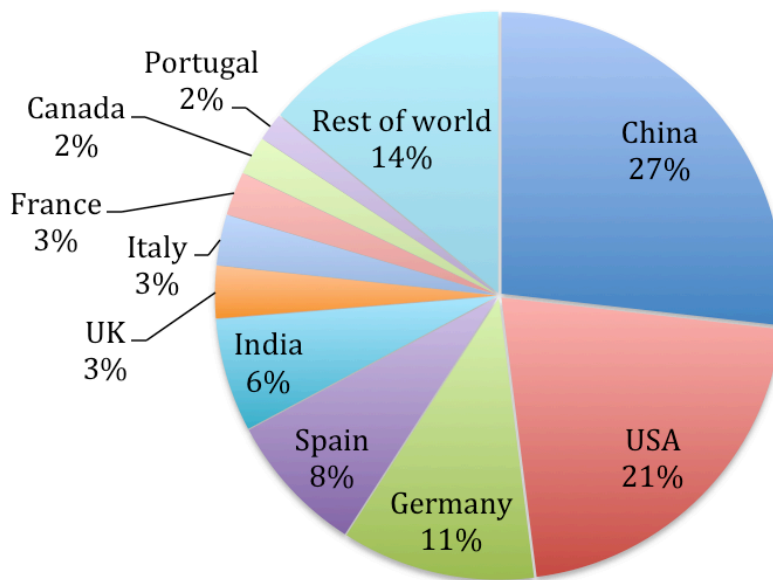


Figure 1.2: World top 10 countries cumulative capacity in 2012, Source: GWEC

## 1.2. European Wind Energy Outlook

The 20-20-20 EU targets represent an integrated approach to climate and energy policy that aims to combat climate change, increase the European Union's (EU) energy security and strengthen its competitiveness. They are also headline targets of the Europe 2020 strategy for smart, sustainable and inclusive growth. It is estimated that meeting the 20% renewable energy target will help achieve the 20% energy efficiency improvement in 2020. Wind and

Solar power are the main contributors to achieve the EU target. Wind power's share of total installed power capacity has increased five-fold since 2000; from 2.2% in 2000 to 11.4% in 2012. During the same period, renewable capacity increased by 51% from 22.5% of total power capacity in 2000 to 33.9% in 2012.

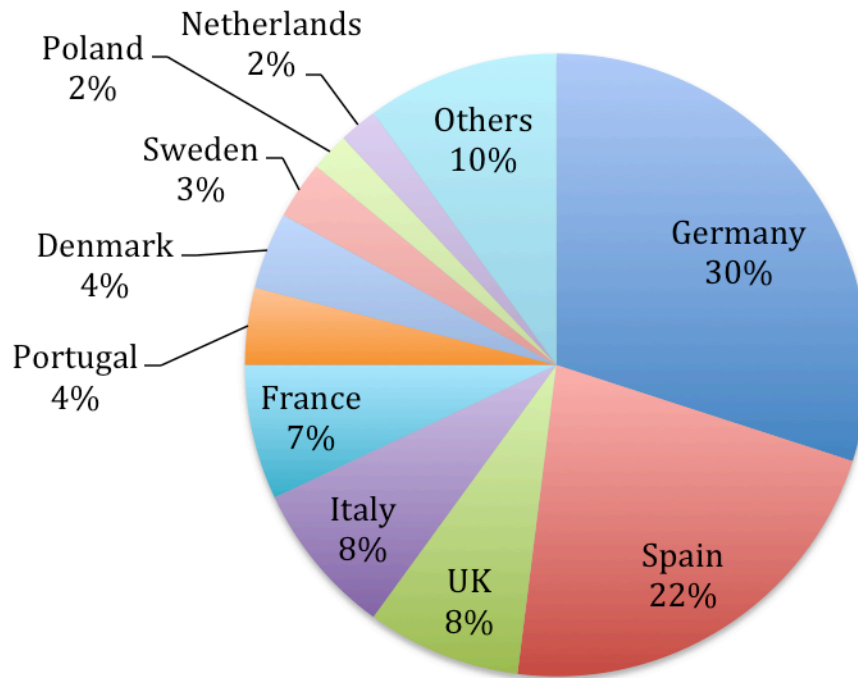


Figure 1.3: EU member state market share for total installed capacity, Source: EWEA

Figure 1.3 gives the Europe top 10 countries share of total installed wind capacity at the end of 2012. A total of 106 GW was installed until the year 2012 in European Union with a growth of 12.6% compared to the previous year. This growth rate is similar to the growth recorded in 2011. Germany remains the EU country with the largest installed capacity, followed by Spain, Italy, UK and France. Austria, Belgium, Denmark, Ireland, Netherlands, Poland, Portugal, Romania and Sweden have over 1GW of installed capacity. Germany (31.3GW) and Spain (22.8 GW) have the largest cumulative installed wind energy capacity in Europe. Together they represent 52% of the total EU capacity. The UK, Italy and France have 8.4 GW, 8.1 GW and 7.6 GW respectively. Poland has 2.5

GW of cumulative capacity ahead of Netherlands (2GW) and Romania (1.9 GW) (EWEA, 2013).

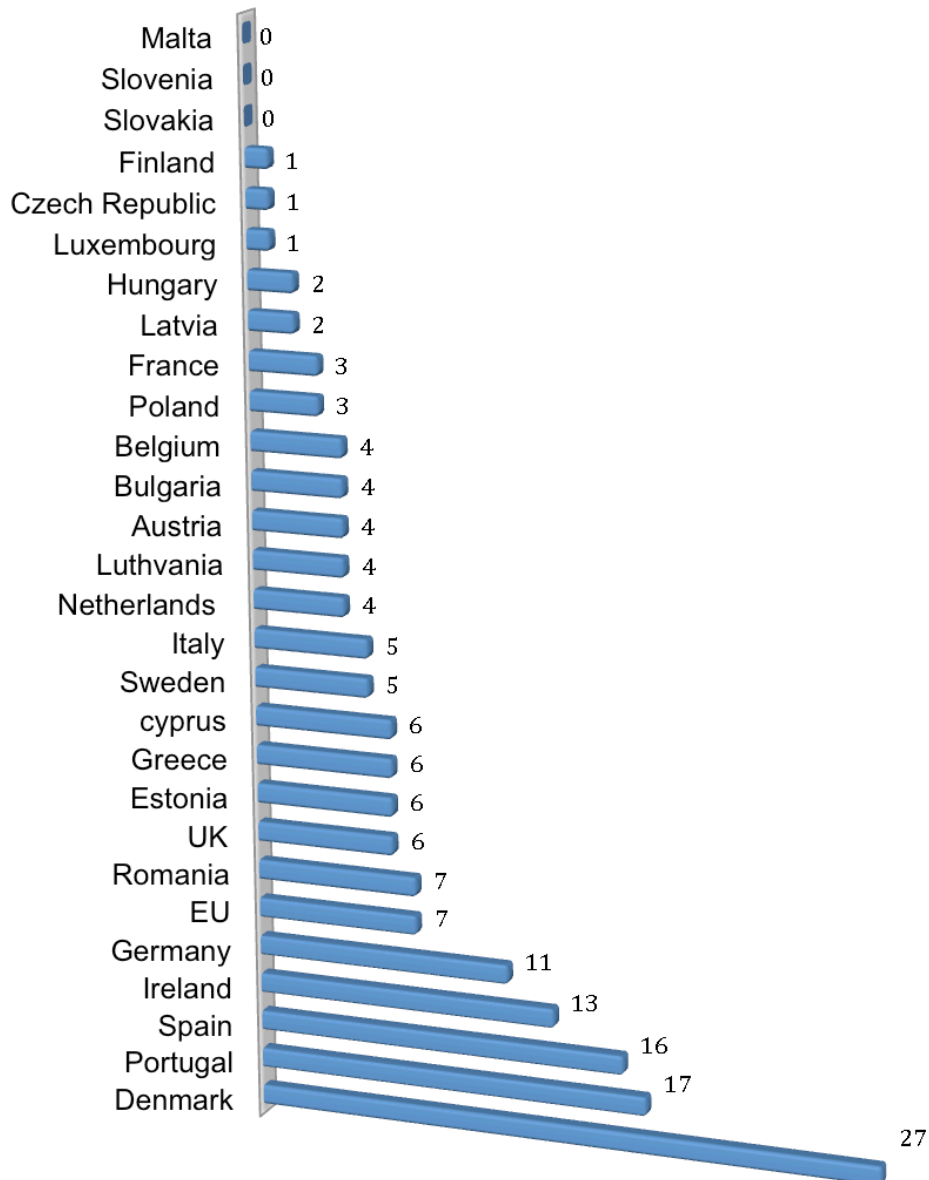


Figure 1.4: Wind power share of total electricity consumption in EU (7%) and in member states in 2010, Source: EWEA

The wind capacity installed at the end of 2012 will, in a normal wind year produce 231 TWh of electricity, representing 7% of the EU's gross final consumption. Figure 1.4 gives the wind power share of total electricity

consumption in EU and in member states in 2012. According to the sources (EWEA, 2010), Denmark remains the country with highest penetration of wind power in the electricity consumption (27%), followed by Portugal (17%), Spain (16%), Ireland (13%) and Germany (11%). In the newer member states, Romania has the highest wind energy penetration (7%).

### **1.3. Nature of wind**

The energy available in the wind varies as the cube of the wind speed, so understanding the characteristics of the wind speed is necessary in all aspect of wind energy exploitation, site identification and prediction of the economical viability of wind projects and understanding their effects on electricity distribution networks. The most striking characteristic of the wind resource is its high variability, both geographically and temporally. This variability persists over a very wide range of scales, both in space and time and the importance is amplified by the cubic relationship to available energy.

#### **Geographical variation in wind resource**

The wind is driven almost entirely by the sun energy, causing differential surface heating. The heating is most intense on landmasses closer to the equator and occurs during the daytime. This heated region moves around the earth surface as it spins on its axis. Warm air rises and circulates in the atmosphere to sink back to the surface in cooler areas. This large-scale motion of the air is strongly influenced by Coriolis force due to the earth's rotation.

The non-uniformity of the earth's surface ensures that this global circulation pattern is distributed by smaller-scale variations on continental scales. These variations interact in a highly complex and non-linear fashion to produce chaotic results. Local topographical and thermal effects temper these differences more. Hills and mountains increase the wind speed locally; this is partly a result of altitude as the boundary layer flows over the earth's surface which means that wind speeds generally increase with height above the ground. And partially a

result of the acceleration of the wind flow over and around hills and mountains and funneling through passes or along valley aligned with the flow.

Thermal effects also result in considerable local variations. Coastal regions are often windy because of differential heating between land and sea. While the sea is warmer than the land, a local circulation develops in which surface air flows from land to the sea, with warm air rising over the sea and cool air sinking over the land. When the land is warmer this pattern reverses. Thermal effects may also be caused by differences in altitude. Thus the cold air from the high mountains can sink down to the plains below, causing quite strong and highly stratified down slope wind.

#### **Long term wind speed variation – Annual and seasonal**

There is evidence that the wind speed at any particular location may be subjected to very slow long-term variations, which might be linked to long-term temperature variation. This might be caused by the human activity (global warming), on climate and this will undoubtedly affect wind climate in the coming decades. Apart of these long term trends there may be considerable changes in the windiness at a given location from one year to the next. These changes have many causes, such as global climate phenomena (*el Niño*), changes in atmospheric particulates resulting from volcanic eruptions and sunspot activity (Burton, 2011). These add uncertainty in predicting the energy output of a wind farm at a particular location during its projected lifetime.

Temporal variability on a large scale means that the amount of wind may vary from one year to the next, with even longer scale variation on a scale of decades or more. These long-term variations are not well understood, and may make it difficult to make accurate prediction of the economic variability of particular wind farm project. But seasonal variations are much more predictable, although there are large variations on shorter timescale, which are often not predictable more than few days ahead.

### Synoptic and diurnal variation

Wind speed variations are somewhat more random and less predictable at shorter timescales than the seasonal change. The synoptic variations, which are associated with large-scale weather patterns such as area of high and low pressure and associated weather fronts as they move across the earth's surface. This large-scale atmospheric circulation patterns takes few days to pass over certain location or may occasionally stick one place for longer time before finally moving or dissipating. These variations have definite patterns, the frequency content of these variations typically peak at around four days or so. Depending on location, there may also be considerable variations with the time of the day, which again are usually fairly predictable this is usually driven by local thermal effects. Intensive heating in the daytime causes large convection zone in atmosphere that dissipate at night.

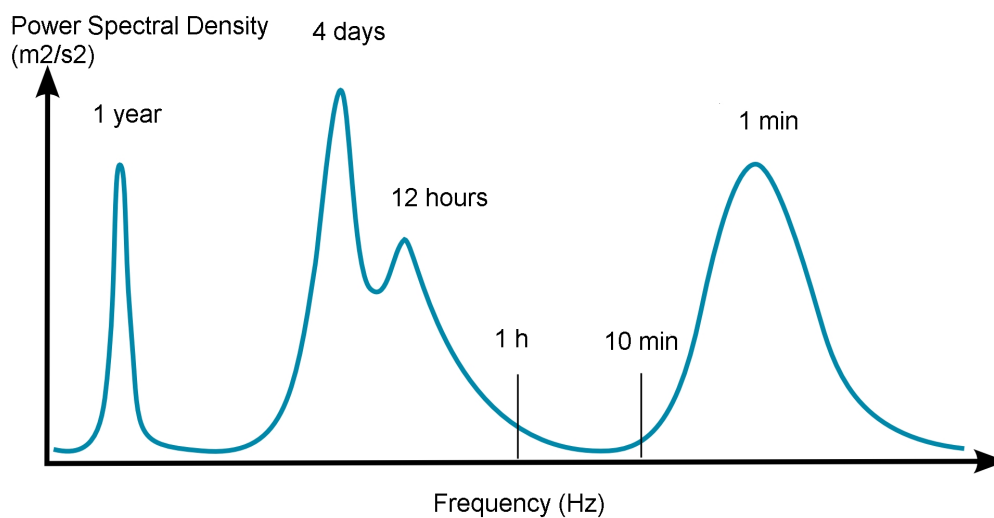


Figure 1.6: Wind spectrum, Source: [Van Der Hoven \(1957\)](#)

[Van Der Hoven \(1957\)](#) identified two main peaks of power spectrum: one at a period of 4 days which corresponds to the passage of large pressure systems at synoptic scale, and one at a period of about one minute which corresponds to a mechanical and convective type of turbulence in horizontal wind spectrum. (Figure 1.6). A large spectral gap separates those two peaks, and the ABL

study under the steady-state assumption corresponds to an averaging of the small-scale turbulence.

#### **1.4. Atmospheric Boundary Layer**

The atmospheric boundary layer (ABL) is the part of the troposphere which is directly influenced by the presence of the earth's surface, and responds to surface forcing with a time scale of an hour or less (Stull, 1988). In general, the height of the boundary layer can be taken as the height above the surface at which the fluid's velocity returns to 99% of the undisturbed velocity. In the atmosphere, where the wind is interacting with the planet's surface, this region extends to a height of approximately 1-2 km. Along with a decrease in velocity; this region is also characterized by an increase in turbulence, which creates both vertical and horizontal fluxes of momentum, heat and water vapor. This region of complex flow is where the vast majority of human activities occur and all wind turbines are placed. Thus, the ABL has been subject to intense scrutiny over the past decades and so in recent years both measurement and simulation technologies begin to develop to a stage where they can deal with its almost stochastic nature.

Zdunkowski and Bott (2003) suggested dividing the ABL in three sublayers: roughness sublayer, inertial sublayer and Eckman layer. The layer of interest in the wind energy domain is the inertial sublayer and Eckman layer. Prandtl layer (combines roughness sublayer and inertial sublayer) extends from the roughness height  $z_0$ , where the mean wind is assumed to vanish, to about 100 m. The ground surface friction and the heating or cooling from the ground influences it. Atmosphere is qualified as thermally stable, unstable or neutral depending on the temperature profile through the Prandtl layer (Azad, 1993). The flow in the Prandtl layer is used in many applications such as wind loads on structures, dispersion of pollutants, weather forecast and wind turbine or building siting.

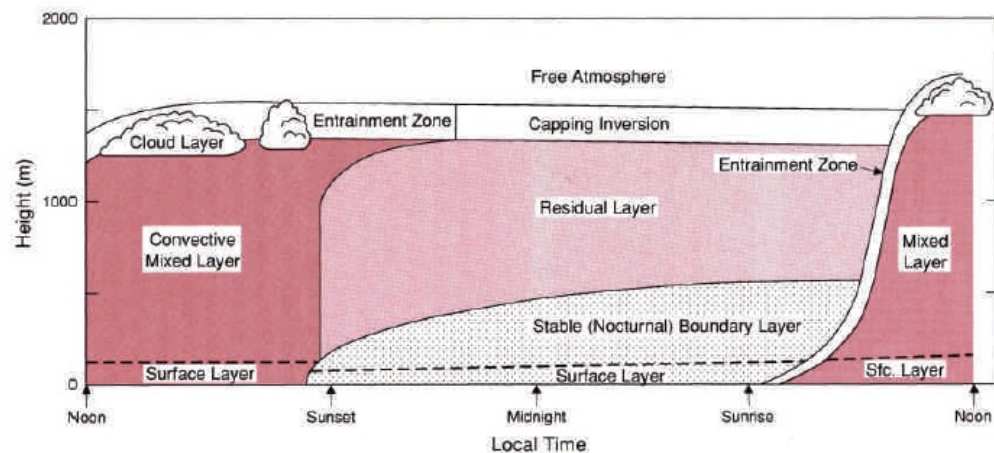


Figure 1.5: Schematic of the diurnal variation of the planetary boundary layer height and structures in fair weather condition, Source: [Stull, \(1988\)](#)

In the land surface in high-pressure regions the boundary layer has well defined structure that evolves with diurnal cycle. The boundary layer consists in a convective mixed layer capped by an entrainment zone during the day and in a stable layer with a residual layer above during the night. The schematic of diurnal variation of the boundary layer height and structure in fair weather condition is shown in figure 1.5. The surface layer is typically 10% of the boundary layer and is characterized by large vertical gradient of temperature and wind speed, a constant wind direction, and nearly constant fluxes of heat and momentum above the tops of dominant surface roughness elements ([Stull, 1988](#)). The daytime mixed layer is characterized by uniform and vigorous turbulent mixing, which is caused by surface heating and convection. The nocturnal stable boundary layer, on the other hand, is much shallower and is characterized by weaker turbulent mixing associated with wind shear and wave activity. The nocturnal boundary layer is more appropriate in modeling for wind energy and pollutant dispersion from near surface sources. The residual layer is essentially disconnected from the surface at night but it may still have some patchy turbulence, confined to certain shear layer or region of wave breaking.

## 1.5. Flow over Complex Terrain

Complex terrain can be defined as the landscape that normally contains mountains and valleys. This kind of terrain is made by systems of crests and valleys that can be characterized by steep slopes, gives rise to thermally induced circulations like mountain-valley breezes, generates mountain waves, and strongly modifies the characteristics of synoptic flow (Atkinson, 1981; Whiteman, 1990; Durran, 1990; Whiteman and Doran, 1993; Finardi, 1997). The mountain/valley breezes are more easily observed during anticyclone weather in summer. In such conditions the differential warming of the mountainsides gives rise to horizontal temperature and pressure gradients that generate winds. Figure 1.7 shows the mountain and valley wind system by day and at night.

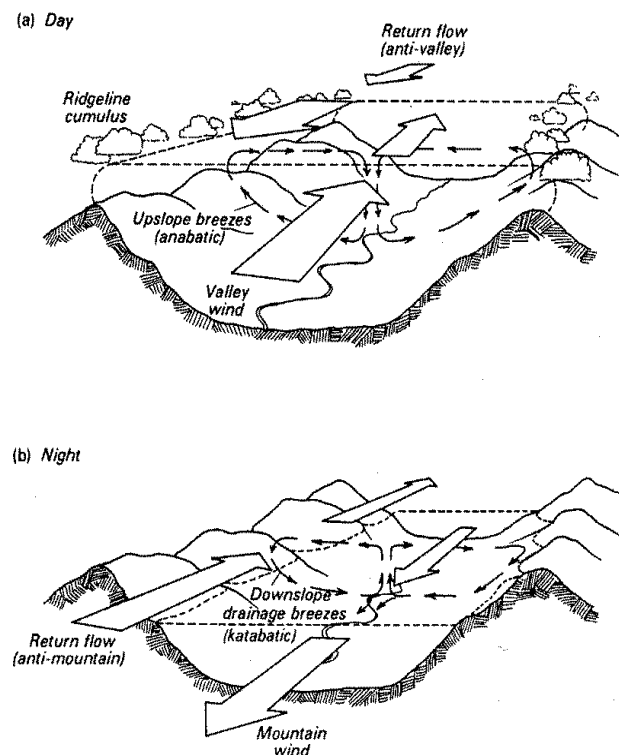


Figure 1.7: Mountain and valley wind system by day and at night (Source: Oke, 1987)

The characteristics of the wind systems depend on the geometry and orientation of the valley. The mountain winds can be roughly divided in two classes: slope winds and valley winds. The slope winds are produced by buoyancy forces induced by temperature differences between the air adjacent to the slope and the ambient air at the same height far from the slope (e.g. over the center of the valley): slope winds blow up-slope during daytime and down-slope during night-time. To maintain continuity a closed circulation develops across the valley, involving air moving downward in the valley center during the day and upward during the night. The cross-valley circulation transports heat across the valley, heating (or cooling) the whole valley atmosphere, and therefore contributes to the development of valley winds.

The actual development of thermally driven winds is often complicated by the presence of other wind systems developed on different scales as described by [Whiteman and Doran \(1993\)](#). These thermal winds show important seasonal variation both in frequency and intensity, generally being strongest during summer, while during winter snow-covering slopes can generate cold breezes that can last also during the daytime. This type of terrain and circulation spans a wide range of scales, from local to sub-synoptic scale. On this kind of topography simple assumptions are no more valid and only extensive measurements or simulations employing models of proven capability can describe the flow.

Terrain effects play very important role in modifying wind speed and direction on the site ([Sreevalsa, 2010](#)). Wind profile and turbulence are not well understood in these regions and steps are taken to understand and predict the wind flow over complex terrains. The maximum wind speed obtained at the hilltop is induced by topographic features, which can double the available power ([Sreevalsa, 2010](#)). Assessment of wind resource in complex terrain is complicated by highly unsteady conditions and turbulence in the wind and large horizontal gradients. Accuracy of predicting the wind resource assessment for complex terrains depends on the solved equations. Linear wind flow models

solve the linearized form of Navier-stokes equation and cannot capture the complex flows with recirculation and separation and influence of topography on the wind. While nonlinear CFD model using proper turbulence modeling with appropriate lateral wind boundary condition are able to predict complex flow in such terrain.

## 1.6. Annual Energy Production of Wind farm

Every wind farm developer requires an estimate of how much wind energy is available at potential development sites. The correct estimation of the energy available can decide the existence of the wind farm. The Annual Energy Production (AEP) gives a measure of this energy estimation. Wind maps developed from the late 1970's to the early 1990's provided reasonable estimates of the region in which good wind energy resources could be found. A more accurate wind resource assessment is difficult and it is gaining importance during the planning of future wind farms. Development of new computing tools and new meteorological data sets allow creating even more accurate and detailed wind maps of a particular region (EWEA, 2009).

The AEP of the wind farm is calculated as product of wind turbine power curve and wind speed distribution at the site. The power  $P$  available in wind can be expressed as:

$$P \propto \frac{1}{2} \rho v^3 A \quad (1.1)$$

Where,  $\rho$  is density,  $A$  is the area swept by the wind turbine blade and  $v$  is the velocity at the turbine hub height. The energy produced from turbine varies mainly with wind speed and is also affected by the vertical wind shear and the turbulence. The cubed dependency on the wind speed amplifies the uncertainties in the energy production by a factor between 2 and 3 (Sreevalsa, 2010). In complex terrain, the assessment of wind energy resource is difficult

because of the high spatial variability of the wind and turbulence fields and the uncertainties associated with AEP vary significantly depending on the location. (Montes et al., 2009) showed the influence of wind shear and seasonality on the power curve and AEP of wind turbine. Wind resource assessment uses generic power curve provided by the manufacturer, which is not adapted to the site conditions. Instead, site-specific power curves that consider site wind characteristics should be used. Otherwise, the wind farm energy yield results can be misleading (NREL, 1997). To calculate the net energy production of a wind farm, the following additional factors are applied to the gross energy production: wind turbine wake loss, wind turbine availability, electrical losses, blade degradation, high/low temperature shutdown, high wind speed shutdown and curtailments due to grid issues.

## **1.7. Objective and motivation**

The main objective of this PhD thesis is to improve the accuracy of wind resource assessment in complex terrain. Many models were developed in the past decades for wind resource assessment but the uncertainties in wind speed predictions were high in complex terrain. In previous work (Laporte, 2008) carried out at EDF R&D and CEREAs a 4-step methodology was developed for wind resource assessment in complex terrain. The meteorological mast was used as a link between the mesoscale model data and CFD simulation. Clustering of meteorological condition was used to reduce the number of simulation needed to reproduce 1 year of atmospheric flow over the particular site. A significant reduction of the error in the annual mean wind calculation was shown with the CFD approach compared to the classical operational approach (WAsP).

The present research work focuses on improving the coupled mesoscale and microscale CFD methodology. Developing an improved coupling method between mesoscale and microscale CFD models and assimilating field measurement data into the CFD domain can obtain the improvement. This

methodology uses the operational ALADIN mesoscale model as input for the microscale CFD model *Code\_Saturne*. The main steps of this work are as follows:

- Coupling method: To use the operational mesoscale model data on the microscale CFD grid, new coupling methods such as extrapolation and Cressman interpolation were developed and implemented in *Code\_Saturne*. CFD simulations were carried out to test and validate the new coupling methods along with the existing translation coupling method.
- Data assimilation: Nudging, a 4DDA technique is developed and implemented into *Code\_Saturne*. It is used to assimilate the field measurements at the measurement location inside the CFD domain.
- Sensitivity test were carried out for: grid independence, to determine the optimum radius of influence for the Cressman interpolation at inlet boundary, to determine the radius of influence of the volumetric Cressman interpolation for nudging the field measurement data, nudging coefficient and Cressman spreading function.
- Validation: For the initial validation sonic anemometer measurements were used for nudging. CFD simulation without assimilation and CFD simulation with assimilation were carried out for 2 main wind directions. Comparisons between field measurements, CFD simulations without and with assimilation were carried out at 3 measurement mast locations.
- Annual wind speed prediction: Cluster center from the clustering process of Laporte (2008) were used to carry out the microscale CFD simulations. Assimilation is performed with operational measurement data such as cup anemometer (available for 1 whole year). CFD simulations were carried out without assimilation and with assimilation for

64 clusters. Annual average wind speed is then calculated and compared with measurements and WASP result for CFD simulation without and with assimilation.

## 2. Wind Resource Assessment

The accurate prediction of wind resource and optimal design of a wind project depends on the obtaining accurate and detailed understanding of spatial distribution of wind characteristic across the project area. The last two decades have seen the rise of different wind flow models: conceptual models, physical model, statistical model and numerical models. Numerical linear models have biggest share of wind resource assessment and non-linear CFD models are now starting to be used widely as flows become complex with steep topography and wind farm wake interaction in onshore and offshore. More recently mesoscale and microscale CFD models were combined. This chapter gives an overview of these different wind flow models.

### 2.1. Regional wind resource

Prior to the planning of a wind farm, it is essential to determine where the abundant wind resources exist, understand their characteristics, and validate their quality. Regional wind resource assessment gives the large-scale picture of wind speeds available at global and national level. Regional wind resource assessment may be determined using both existing measurements and mesoscale modeling approaches to produce wind resource maps. These wind maps cover spatial scales of hundreds or thousands of kilometers. For the wind farm developer, the regional wind maps are valuable preliminary tools for site finding, but are not accurate locally (EWEA, 2009). Regional wind maps are used to select the potential area for a wind farm site. The site is then characterized in order to assess the local conditions and to decide whether the wind resource in a given region of interest is sufficient. Detailed local wind assessment is then carried out for the precise turbine siting.

Figure 2.1 shows the wind resource availability in Europe at 80 m height. AWS Truepower (2012) used coupled mesoscale and microscale models for the

prediction of wind resource and color map shows the mean wind speed magnitude (AWS Truepower, 2012). North sea regions, Greece, coastal regions of United Kingdom and Southern coast of Spain have higher annual wind speed. Every European country has a substantial technically and economically exploitable wind resource (EWEA, 2009).

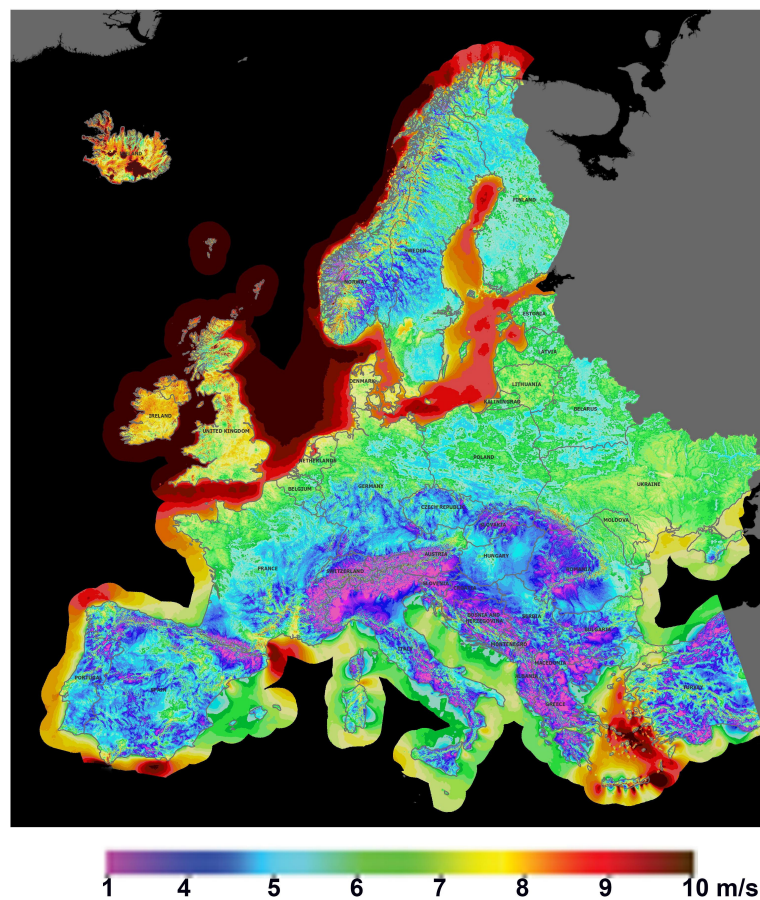


Figure 2.1: Wind resource map of the Europe, Source: AWS Truepower, (2012)

## 2.2. Local wind resource

In the previous section the wind resource map of Europe was discussed and in this section the wind resource at local scale is presented. The purpose of this section is to consider the wind resource assessment and modeling at a local wind farm. The single most important characteristic of a site is its wind speed,

and the performance of a wind farm is very sensitive to uncertainties and errors in the basic wind speed estimate. Turbulence in the wind is another major characteristic that affect the power performance, turbine load, fatigue and wake effects.

For the majority of prospective wind farms, the developers undertake a wind resource measurement and analysis program. This provides a robust prediction of the expected energy production over its lifetime. The main issues are to record an appropriate set of wind data, and develop the methodologies that can be used to predict the expected long-term energy production of a project. It is noted that a prediction of the energy production of a wind farm is possible using only off-site data from nearby meteorological stations, as sometime done with the WAsP model. However, if the meteorological stations used have only data from low level, such as 10 m height and/or the stations are located far from the site, such analyses are generally used only to assess the initial feasibility of wind farm sites. It is also possible to make predictions of the wind speed at a site using a numerical Wind Atlas Methodology, based on a data source such as the “reanalysis” of NWP model data sets (EWEA, 2009; NYSERDA, 2010; Brower, 2012). Micro-siting has been increasingly performed using microscale models for the wind, which is a promising tool for the local wind resources assessment. More recently, advanced modeling techniques are revealed such as coupling mesoscale (WRF) and microscale models (CFD or WAsP) for local wind resource assessment.

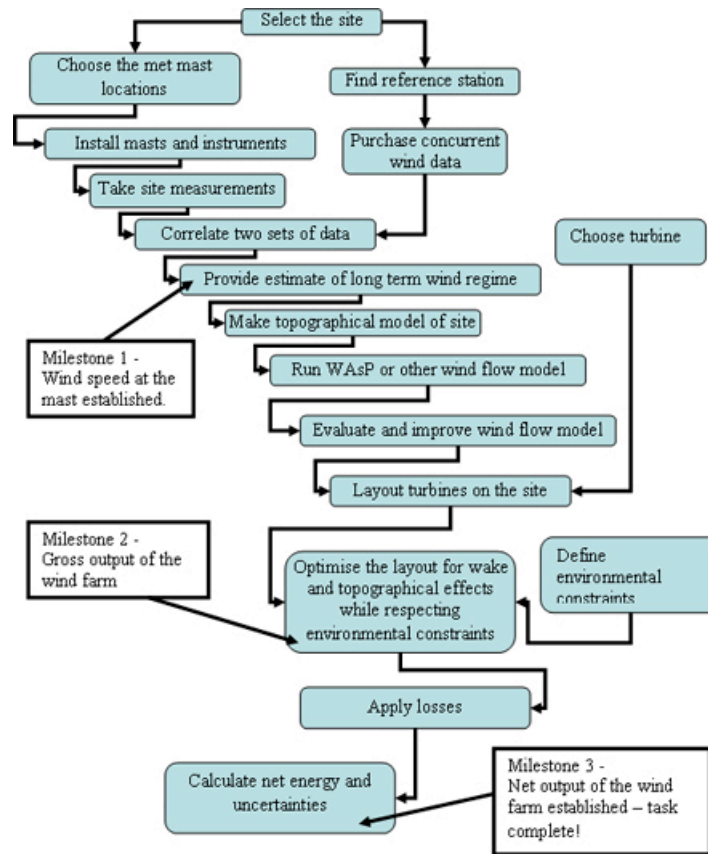


Figure 2.2: Overview of the energy prediction process, Source: Garrad Hassan

Figure 2.2 represents the flow chart of the local wind resource assessment process. Meteorological towers equipped with anemometers, wind vanes, and temperature, pressure, and relative humidity sensors are installed at the selected site to provide input data for the assessment. Remote sensing devices (LIDAR, and SODAR) are also more and more considered as valuable tools as they are able to give vertical profiles up to the rotor top. Once all the necessary data are available, wind flow model (WAsP, CFD) are carried out. It is also necessary to iterate the turbine selection and layout design process, based on environmental conditions such as turbine noise, compliance with electrical grid requirements, commercial considerations associated with contracting for the supply of the turbines and detailed turbine loading considerations (EWEA, 2009).

## **2.3. Types of wind flow models**

### **2.3.1. Conceptual models**

Conceptual models of wind resource assessment are theories derived from the practical experience and theoretical understanding of boundary layer meteorology. Conceptual models are simple and state that the wind resource at one location is the same as that measured at a different location and describes how the wind resource is likely to vary across the terrain. [Brower \(2012\)](#) suggested that conceptual models includes theories concerning the influence of elevation on the mean wind speed, the relationship between upwind and downwind slope and speed-up, channeling through a mountain gap, and the impact of trees and other vegetation. These concepts are then applied into practical recommendations for the placement of wind turbines, accompanied by estimates of the wind resource they are likely to experience.

The wind projects are becoming larger and built in more varied wind climates, it becomes more and more difficult to use conceptual approach alone for wind turbine siting. These models could be good in relatively flat terrain or along a fairly uniform ridgeline but when the terrain and land cover vary substantially, complex mathematical models are required. But a good conceptual understanding is better than a bad numerical model, or a good numerical model that is wrongly applied ([NYSERDA, 2010](#)).

### **2.3.2. Physical models**

In physical model, a small-scale model of a wind project area is tested in a wind tunnel. The conditions in the wind tunnel such as the speed and turbulence are matched to the scale of the model to replicate the real conditions as closely as possible with compliance to some similitude rules. When the wind tunnel is running, the wind speeds are measured at various points on the scale model using hot wire anemometers or Laser Doppler Anemometer (LDA) or Particle

Image Velocimetry (PIV). The results form a picture of how the wind varies across the site. The relative speeds between points are then usually related to a mast where the speeds have been measured in the field. The method has some limitations such as the separated flow regions which cause problems in the use of hot-wire anemometer, difficulty of modeling thermally stable conditions, and the challenge of appropriately matching atmospheric parameters to the physical scale. Numerical models can be used along side with wind tunnel to provide solution for wind engineering problems. Figure 2.3 shows some examples of scaled model of physical modeling tested in wind tunnel.

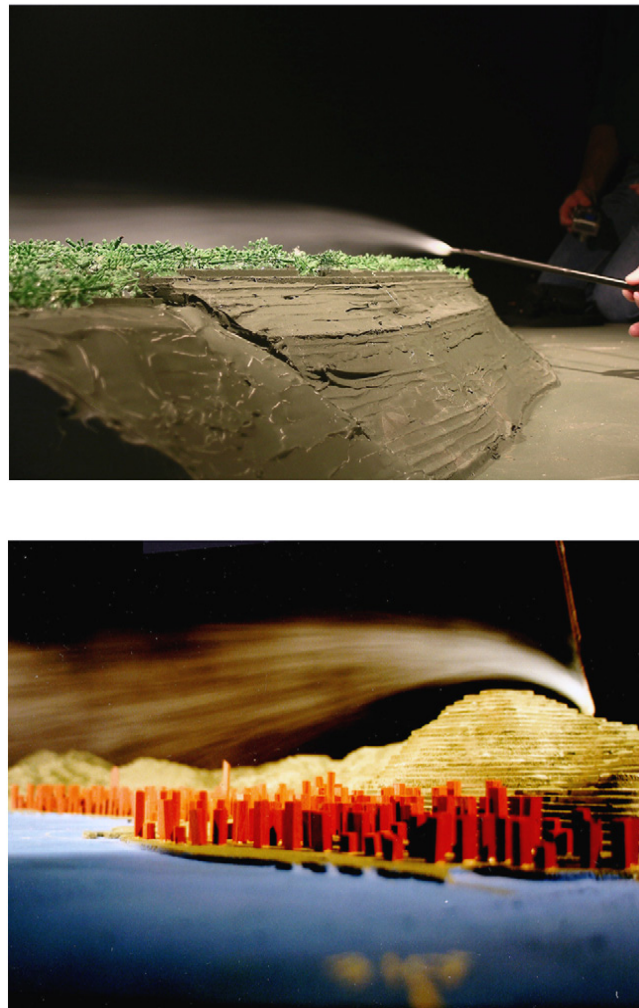


Figure 2.3: Flow separation on a model site for potential wind farm site (top) and Victoria Park on Hong Kong for wind structure at central in the boundary layer wind tunnel (bottom) Source: [Cochran et al. \(2011\)](#)

### 2.3.3. Statistical models

Statistical models use relationship derived from on-site wind measurements for wind resource assessment. Statistical models are fairly simple and well grounded in measurements. They use parameter such as elevation, slope, surface roughness and forest to derive the relationship from the observed wind resource at meteorological masts. Wind speed measurements from several masts in a wind project area are plotted against elevation. A relationship could be derived to predict the speed at any point within the project area. Good understanding of wind flows is necessary to choose the parameter that has reasonable theoretical relationship. Ruggedness Index (RIX) correction is a good example that is sometimes used with the WAsP model. RIX is a parameter that has been found through statistical modeling to be a good predictor of WAsP errors in some circumstances (NYSERDA, 2010). These models work well for wind climates driven by synoptic-scale winds, which tend to have clear relationship between wind speed and certain topography indicators such as elevation (Brower, 2012).

Statistical model produces large error, when the predictions are made outside the range of condition of model parameters. They are very less reliable when the measurement masts are installed at different elevation along slope, while the numerical models are designed to produce plausible results in wide range of conditions.

### 2.3.4. Numerical models

Numerical wind flow models are spatial modeling methods widely used for wind resource assessment in wind energy sector. These models are based on the various theoretical approaches and solve some of the physical governing equation of motion of the atmosphere. Numerical models are classified into five categories: mass-consistent, linear (Jackson-Hunt), microscale CFD,

mesoscale models and coupling mesoscale and microscale models. Numerous research works are focused towards coupling of mesoscale and microscale model for wind resource assessment in complex terrain and interaction of wind turbine wakes in onshore and offshore.

#### **2.3.4.1. Mass-Consistent model**

Mass consistent models developed in 1970 and 1980 solve just one of the physical equations of motion that governing mass conservation and gives rather a simple description of real flow. Mass conservation implies wind forced higher terrain must accelerate so that same volume air passes through the region at the same time (NYSERDA, 2010; Brower, 2012). The usual resolutions of these models are medium to high and computational requirements are low. NOABL (Philips, 1979) is the basis of all the mass-consistent models and several modification of this model exist commercially.

The solutions of mass-consistent models are not unique and they cannot handle thermally driven wind patterns, such as sea breezes and mountain-valley circulations, and flow separations on the lee side of hills. Tammeli et al. (2001) showed that mass consistent model results often show quite similar behavior to the European Wind Atlas results and also have similar limitation to the European Wind Atlas.

#### **2.3.4.2. Jackson-Hunt models**

These models were developed in the 1980s and 1990s and are based on a theory by Jackson and Hunt (1975). In addition to mass conservation they also solve momentum conservation by solving a linearized form of the Navier-Stokes equations governing fluid flow. Hence they are also called as linear models. The simplification of the Jackson-Hunt theory is that the terrain causes a small perturbation to an otherwise constant background wind. This assumption allows

the equations to be solved using a very fast numerical technique and typically a few minutes on standard personnel computer for a calculation (Probst et al., 2010). WAsP (Troen, 1989; Troen, 1990), MS-Micro (Walmsley, 1982), Raptor (Ayotte, 1995), Raptor NL (Ayotte, 2002) and MS3DJH (Beljaars, 1987; Taylor, 1983) were based on the Jackson-Hunt theory.

## WAsP

The Wind Atlas Analysis and Application Program (WAsP), is a computer program for predicting wind climates. WAsP was developed and distributed by Risoe National Laboratory, Denmark, now part of the Wind Energy Division at DTU, Denmark ([www.wasp.dk](http://www.wasp.dk)). WAsP is a well-established industrial standard flow-modeling tool. WAsP is used for: wind farm production, wind farm efficiency, micro-siting of wind turbines, power production of wind turbines, wind resource mapping, wind climate estimation, wind atlas generation, wind data analysis, map digitations & editing, and power & thrust curve editing (Bowen et al., 2004). It remains the most widely used numerical wind flow model in the wind industry. WAsP is based on linearized form of the fluid flow equations and its most fundamental assumptions do not differ much from other approaches such as MS3DJH, both being built on the seminal work of Jackson and Hunt (1975). It has two stages: the observed wind at a mast is used to derive the background wind field, which represent the wind resource in the absence of terrain and the process is reversed using the background wind as input to predict the wind profile at other points (figure 2.4).

It forms the basis of much of the wind resource assessment that was done previously. The main advantages of WAsP are the relatively easy model inputs and fast computational speed. In addition WAsP also includes the ability to incorporate the effect of surface roughness change and sheltering obstacles. The sources and magnitude of error in the model are estimated in many applications and well understood. Errors are small for simple flat terrain, while the errors are significantly higher for complex terrain as shown by Bowen et al.

(2004), Laporte et al. (2008), Cabezón et al. (2006), Politis et al. (2008), Palma et al. (2008) and Abiven et al. (2011). This limitation is caused by linearization of the governing equations.

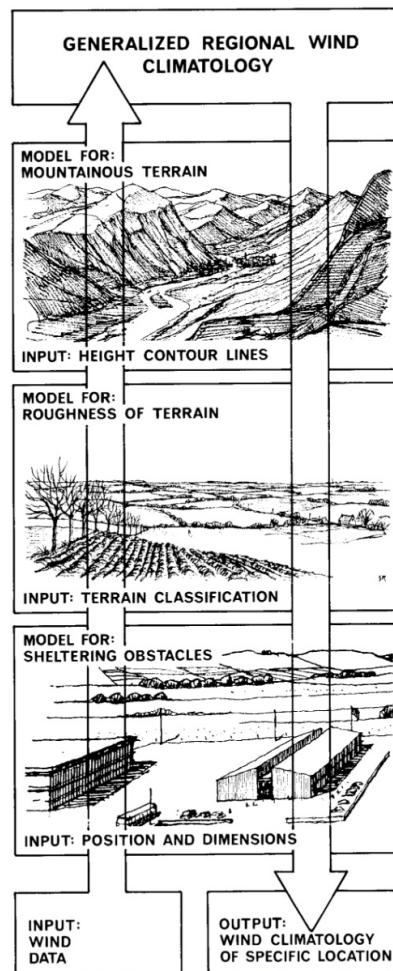


Figure 2.4: The WASP mapping process, Source: Risoe National Laboratory

Like other Jackson-Hunt models, WASP is not equipped with to handle complex terrain. Complex refers to the context where the slope exceeds 30% over a significant area. WASP problem is that steep terrain induces change in wind flow, which may include flow separation at abrupt change in slope, vertical wind and recirculation behind cliff. One major problem with WASP is that it overestimates the speed-up at top of hills when the input data is a wind measurement on a near flat terrain. The WASP model also ignores the effect of

thermal stability and temperature gradients. Thermal stratification and buoyancy forces can have a large influence on the response of wind to the terrain.

Despite the numerous limitations, WAsP remained very popular. This is because the initially wind farms were developed in relatively flat terrain but increasingly more wind farms are proposed in complex terrain. However, a simple terrain correction called RIX-analysis is available in WAsP for complex terrain and the results are satisfactory (Bowen, 1996 and Berge et al., 2006).

#### **2.3.4.3. CFD modeling**

Computational fluid dynamics (CFD) uses numerical methods and algorithms to solve and analyze problems that involve fluid flows. Numerical CFD modeling provides large amount of details about the flow in the whole domain under varied conditions. Also it allows flow investigation where experimentation is not possible. CFD modeling has very wide range of application and Navier-Stokes equation is used to solve the flow field. The main limitation of CFD modeling is that it requires more expertise than simpler models, and that it is much more computationally expensive.

CFD modeling is increasingly used in the wind industry for wind resource assessment in complex terrain and in wake analysis of wind farm but it still requires more validation and guidelines for a correct application. It aims at detailed analysis of the specific area that shows high capability for wind farm site. It predicts the magnitude of the available wind energy resource and provides the site assessment and optimizes the location of wind turbine in a wind farm. Like linear models, microscale CFD models require digital elevation map, roughness map and wind climatology of the site as input data. As results wind resource map of site is obtained, which includes magnitude and direction of wind, turbulent kinetic energy, dissipation and wind power density.

Several methods were developed for predicting the turbulent flow using CFD. Three most popular simulation methods are: Direct Numerical Simulation (DNS), Large Eddy Simulation (LES) and Reynolds-Average Navier-Stokes simulation (RANS) are briefly discussed.

### **Direct Numerical Simulation (DNS)**

Direct numerical simulation (DNS) solves turbulent velocity field without the use of turbulence modeling. This means that Navier-Stokes momentum equation for fluid must be solved exactly, which includes whole range of spatial and temporal scales of the turbulence to be resolved. So all the spatial scales of the turbulence must be resolved in the computational mesh, from the smallest dissipative scales (Kolmogorov microscales), up to the integral scale, associated with the motions containing most of the kinetic energy. DNS can examine fully developed turbulence flow fields at a microscale and perform accurate turbulence calculation of flow properties. When DNS are properly carried out it would be comparable in every way with quality measurements (Ferziger, 1993). However practically it is applicable only to simple geometries, Low Reynolds numbers flows and most unlikely used for engineering application tool (Speziale, 1998).

Also three-dimensional DNS requires a high number of mesh points satisfying the Reynolds number. And the memory storage requirement in a DNS grows very fast with the Reynolds number. In addition, given the very large memory necessary, the integration of the solution in time must be done by an explicit method. This means that in order to be accurate, the integration must be done with a time step,  $\Delta t$ , small enough such that a fluid particle moves only a fraction of the mesh spacing in each step. Therefore, the computational cost of DNS is very high, even at low Reynolds numbers. In most industrial flows, the Reynolds numbers are usually high and DNS requires high computational resource and even could exceed the capacity of most powerful computers.

DNS is used to compute the process of transition from laminar to turbulent flows, specific fluid flow state, transient evolution that occurs between one state and another. DNS is stressed as a research tool, aiming to solve at a nearly exact solution to specific turbulent flows. By using DNS it is possible to perform numerical experiments and extract information difficult or impossible to obtain in the physical experiments, allowing a better understanding of the physics of turbulence. Also, direct numerical simulations are useful in the development of turbulence models for practical applications, such as sub-grid scale models for Large Eddy Simulation (LES) and models for the Reynolds-Averaged Navier-Stokes equations (RANS).

### **Large Eddy Simulation (LES)**

**Smagorinsky (1963)** developed LES, a popular technique for simulating turbulent flows. It solves “filtered” Navier-Stokes equation to resolve the large-scale motion in a turbulent flow and model the small-scale motion. It is based on the implication of Kolmogorov's theory of self-similarity, the large eddies of the flow are dependent on the geometry while the smaller scales are more universal and easier to model using subgrid-scale model (SGS model). LES is a transient turbulence model that falls in between DNS and RANS. Compared to DNS, LES is not an exact solution but is less computationally demanding. However, the application of LES to wall-bounded flows, particularly at high Reynolds numbers, is severely restricted owing to the grid resolution requirements for LES to resolve the viscous small-scale motions near the wall. Unlike RANS, LES is not yet applicable to all engineering problems. Several studies have applied LES for ABL flow for wind energy and urban dispersion application.

LES application research for wind resource assessment and over wind farm flows are very limited, **Ivanell (2009)**, **Calaf et al. (2010)**, and **Stovall et al. (2010)** works are limited to neutrally-stratified conditions. The wind farm LES framework of **Porté-Angel et al. (2010, 2011)** is clearly capable of simulation in a variety of stability conditions and interaction between wind turbine wakes.

### Reynolds-Averaged Navier-Stokes simulation (RANS)

Reynolds-averaged Navier-Stokes (RANS) solves the “averaged” Navier-Stokes equation. The time averaging of the equations leads to the introduction of the Reynolds stresses tensor. This is a second order tensor of unknowns for which various models provide different levels of closure. It is a common misconception that the RANS equations do not apply to flows with a time-varying mean flow because these equations are time-averaged. In fact, statistically unsteady flows can equally be treated and it is referred as URANS. The turbulence closure models used to close the equations are valid only as long as the time over which these changes in the mean flow occur is large compared to the time scales of the turbulent motion containing most of the energy. The classical approach to model Reynolds stress term is to adopt eddy viscosity concept proposed by [Boussinesq \(1877\)](#) and another approach is to solve these stress terms.

Boussinesq suggested that Reynolds stress is directly related to the mean shear stress. This is based on the idea that the viscous and Reynolds stresses have similar effects on the main flow. This method uses an algebraic equation for the Reynolds stresses which includes the turbulent viscosity and mean rate of deformation. The number of transport equations associated with the method often refers to the type of models available in this approach. As addition of equations, several types of turbulence models allow to obtain an estimate for the Reynolds stresses in the RANS equations: Zero-equation model ([Smith and Cebeci, 1967](#)), mixing-length model ([Prandtl, 1925](#)),  $k$ - $\epsilon$  model ([Launder and Spalding, 1974](#)). For example, the Mixing Length model is a zero equation model because no transport equations are solved; the  $k$ - $\epsilon$  as two equation model because two transport equations (one for  $k$  and one for  $\epsilon$ ) are solved. The computational cost of RANS is independent of the Reynolds number.

Models based on the Boussinesq approximation poorly simulate flows that have sudden changes in mean strain rate. This sudden change in mean strain rate because the Reynolds stress to adjust at a different rate to the mean flow

processes, so the Boussinesq approximation fails (Wilcox, 1994). Some of the most common flow situations where this occurs are flow over curved surface and flows with boundary layer separation, all regularly seen in wind engineering.

Reynolds stress model approach attempts to actually solve transport equations for the Reynolds stresses. This means introduction of several transport equations for all the Reynolds stresses and hence this approach is much more costly in CPU effort and time consuming. Algebraic stress models (Baldwin and Lomax, 1978) and Reynolds stress models (Launder et al. 1975) are available in this approach. Although RANS is often less accurate, because of its computational efficiency, RANS is the most commonly used CFD methodology for the simulation of turbulent flows encountered in industrial and engineering applications. Note that there is no turbulence model that is universally valid for any flow.

Standard commercial CFD codes like ANSYS Fluent, ANSYS CFX and Star-CD are generally capable of modeling wind resource assessment, turbine siting and wake modeling although these codes requires some adaptation for atmospheric flows. Specialized CFD codes on wind modeling like WindSim, Meteodyn, 3Dwind and WindieTM are available. Wind farm modeling simulates farm behavior and energy output. Meteodyn WT, openWind, WindFarm, WindFarmer, WindPRO, Resoft and WindSim are currently available as wind farm modeling tools. Open sources CFD codes are also available; OpenFOAM and *Code\_Saturne* have atmospheric module for modeling environmental flows and wind resource assessment. Different methodologies, which have been proposed in the past using CFD to achieve wind resource assessment, are discussed below.

### **Review of wind resource assessment using CFD modeling**

CFD modeling is a complex, computationally expensive, expertise and local wind resources assessment tool. Some CFD models have shown very good agreement to wind tunnel experiments for 2D and 3D flows around idealized cliff

and steep hills, even on the lee side with the recirculation zone (Murakami et al., 2003 and Bitsuamlak., 2004). But the success of CFD modeling is not assured, and there is a continuing need to validate CFD results with high-quality wind measurements. This is due to various factors, especially inaccuracies in initial and boundary conditions (which are usually assumed to be homogeneous and follow a neutrally stratified, logarithmic profile), limited grid resolution, and turbulence closure. The Bolund experiment carried out by Risø DTU involved more than 35 different CFD models. The top ten (RANS) models results showed that the average error in predicted mean velocity was on the order of 13-17% for principal wind direction (Sumner et al. 2010).

Non-linear CFD models are recommended by Cabezon et al. (2006), Hong et al. (2011), Politis et al. (2008), Palma et al. (2008), Hanjalic et al. (2008), Rodrigo et al. (2009), Bechmann et al. (2007), Abvien et al. (2011), Wakes et al. (2010), O'Sullivan et al. (2010) for wind resource assessment in complex terrain in comparison with linear model WAsP. The development and choice of turbulence models for wind resource assessment are discussed by Hanjalic et al. (2008), Sullivan et al. (2010), Rodrigo et al. (2009) and Bechmann et al. (2007). Research showed advanced turbulence modeling is necessary for predicting the wind flow over complex terrain.

In complex terrain modeling Hong et al. (2011) showed the importance of the topography resolution in CFD modeling. Hong et al. (2011) presents few methodologies for simplifying the topographical modeling of complex terrain for CFD analysis. The investigation used the tools CAD, SketchUp, Rhinoceros, GAMBIT and Tgrid. SketchUp along with Rhinoceros method resulted in clear resolution and short computational times. The computed air flow driven by the complex topography, appeared to be reasonable for detailed analysis of the dispersion of air-induced matter.

The comparison between linear models and non-linear models for a complex terrain located in the north of Spain (Alaiz hill) was conducted by Cabezon et al.

(2006). CFD simulated wind speed accurately with absolute error significantly less compared to WAsP and turbulence intensity obtained from both models had absolute error over 35%. **Cabezon et al. (2006)** analysis indicates that the non-linear CFD model captured recirculation areas downwind Alaiz hill as well as other remarkable topographic elements.

**Politis et al. (2008)** showed that linear model result in identical flow fields for two opposite wind directions, while non-linear CFD model results are highly asymmetrical in complex terrain. Linear model has difficulty in turbine siting where terrain influences flow field. **Politis et al. (2008)** emphasis the use of CFD in complex terrain for the enhancement of the accuracy of the simulation and for modeling features of the flow that is necessary in the classification of wind turbines.

**Palma et al. (2008)** suggest that nonlinear CFD modeling is appropriate and necessary for installation of a wind farm. They emphasized the attention needed to flow details, making use of higher resolution field data and non-linear time-dependent flow models. Conventional measurements for wind resource assessment showed sudden variation of the wind speed and direction, this indicated the presence of complex wind pattern. Sonic anemometer revealed discrete peak in energy spectrum related with periodic events of duration inferior to the 10 min averaging of cup anemometers. CFD model results compared favorably with field measurements and showed reverse flow regions and high turbulence intensity in vicinity of future turbine locations and conventional linear models and experiments will be insufficient under these conditions. **Palma et al. (2008)** studied the wind resource assessment and possible installation of a wind farm, also proves the need for more detailed determination of the wind conditions, compared with the standard practice in wind turbine siting.

**Wakes et al. (2010)** detailed an initial two-dimensional numerical model developed in order to test various modeling assumption against experimental

field wind data of Mason Bay, New Zealand. [Wakes et al. \(2010\)](#) suggest the following: replicating the roughness pattern at surface is important, the inlet profile should be built with care, modeling only a portion of the domain can have effect on the flow patterns due to outflow effects, modeling decision to be made between the complexity of the topography and the sophistication of the turbulence model and degree to which vegetation and sand transportation are modeled.

[Hanjalic et al. \(2008\)](#) discussed the development of turbulence modeling and treatment of wall boundary condition for wind and environmental flows. LES is reliable but computationally long and not convenient for large-scale simulation in wind and environment flows. Novel developments in transient RANS and RANS/LES approach were discussed; they aimed at improving accuracy of complex flows over terrain and urban areas. [Hanjalic et al. \(2008\)](#) recommended transient RANS simulation for flows where thermal buoyancy is dominant in diurnal dynamics of air circulation and pollution dispersion in urban canopy and complex topography.

To reduce the LES computational cost, [Bechmann et al. \(2007\)](#) proposed model combines LES and RANS. The hybrid RANS/LES model is capable of simulating neutral atmospheric wind over complex terrain. Close to wall, where LES is expensive, RANS  $k-\epsilon$  model is used. This model is tested for familiar Askervein hill and results showed that RANS/LES was capable of capturing the flow separation while RANS models doesn't capture. Also results show the velocity speed-up was under predicted but the turbulence intensity was well predicted in RANS/LES while RANS alone resulted in underestimated turbulence.

[O'Sullivan et al. \(2010\)](#) highlighted important features of wind flow over complex terrain, flow separation and anisotropy of turbulence. The most commonly used  $k-\epsilon$  turbulence model has difficulty in estimating flow separation and turbulence anisotropy. The algebraic structure-based turbulence model (ASBM) and  $v^2f$

(similar to  $k$ - $\epsilon$  model and instead of turbulent kinetic energy  $k$ , the  $v^2f$  model uses velocity scale  $v^2$  and relaxation function,  $f$ ) closure model were used to calculate the flow over hill and results were compared with experimental data. ASBM and  $v^2f$  models demonstrated a good ability to predict the flow including separated region. New wall function was developed and implemented for  $v^2f$  and comparisons with experiments showed good agreement.

Rodrigo et al. (2009) compared the  $k$ - $l$  mixing-length and limited-length-scale  $k$ - $\epsilon$  model. The structure of the ABL is modeled with the limited-length-scale  $k$ - $\epsilon$  model; it imposes a maximum mixing length, which is derived from the boundary layer height for neutral and unstable atmospheric situations or from Monin-Obukhov length when the atmosphere is stably stratified. The performance of the model was tested with measurements from FINO-1 platform using sonic anemometer. Rodrigo et al. (2009) showed that mixing-length models could be more competitive than limited-length scale  $k$ - $\epsilon$  models, as they are more flexible in the way mixing length profile is defined and this can introduce shallower boundary layers.

Cochran et al. (2011) highlight the historical evolution of physical modeling and suggest a similar path for CFD so that it may play a larger role in the wind-load assessment. CFD is likely to replace the physical modeling of the bluff bodies, but more research and analysis need to be done before it. CFD has made useful inroad into siting wind farms in complex terrain, particularly when thermal stratification plays a crucial role. A Large Eddy Simulation (LES) for thermally neutral flow over terrain did not do well in simulating flow at location downwind of the peak, even with vertical grid stretching for better spatial resolution near surface. Cochran et al. (2011) discussed the importance of flow separation over complex terrain. The wind stays attached only to the gentle, smooth terrain and moderately complex terrain does not yield clearly defined points of flow separation. Complex terrain and buildings possess more angular features that establish precise location of flow separation. The proper capture of flow separation and reattachment with CFD lies in adequate grid resolution and

effective treatment of sub-grid scale turbulence (when using LES). Currently CFD codes are improving rapidly, but still have trouble in accurately simulating some flows. With faster computers, great memory and better turbulence closure schemes, CFD will eventually be able to address the answer for wind engineering. Wind tunnel and CFD with cross comparison validation between results will be essential to gain confidence in the methodology.

Abvien et al. (2011) investigated the wind flow characteristics by analyzing the field measurements of cup anemometer and computer simulation. Analysis of wind rose showed very low wind occurrence for specific wind direction, for which steady state simulation predicted large veering values. Abvien et al. (2011) emphasized the further attention to flow details, making use of higher resolution field data and non-linear time-dependent flow models.

Porté-Angel et al. (2011) focused on research effort to develop and validate an LES framework for wind energy application. The tuning-free Lagrangian scale dependent dynamic models are used to parameterize the SGS stress tensor and SGS heat flux. Three models were used to parameterize turbine-induced forces: actuator disk model without rotation (ADM-NR), actuator disk model with rotation (ADM-R) and actuator-line model (ALM). The characteristics of the simulated turbine wake are in good agreement with the measurements collected from the miniature wind turbine placed in wind tunnel boundary layer flow. The turbulence statistics obtained with LES and ADM-NR have some difference with respect to the measurement in the near-wake region. The ADM-R and ALM yield more accurate prediction of the different turbulence statistics in the near-wake region. In far wake region all three models produces reasonable results.

#### **2.3.4.4. Mesoscale modeling**

Mesoscale modeling is a Numerical Weather Prediction (NWP) model adapted to predictions on limited areas. Mesoscale models are being used to generate wind maps for large area screening. Mesoscale in atmospheric science is

defined as the horizontal scale between the global/synoptic and micro-scales (Orlanski, 1975). The global/synoptic scales have horizontal scale of 2000 km and higher up to cover the entire globe. Micro-scales are horizontal scale smaller than 2 km. Further mesoscale are divided into meso- $\alpha$  (200-2000 km), meso- $\beta$  (20-200 km) and meso- $\gamma$  (2-20 km). Meso- $\alpha$  and larger region is termed as synoptical scale by Pielke (1984). Schlünzen et al. (2011) presented a chart showing the relationship between the spatial and temporal scale of the atmospheric phenomena and how they are treated in the Computational Wind Engineering (CWE) models. Figure 2.5 shows how the atmospheric phenomena are treated in mesoscale or obstacle-resolving microscale models Reynolds-averaged Navier-Stokes (RANS) in the right columns. The characteristic scales are based on Orlanski (1975) and Randerson (1976), the model scales are an update of diagrams by Schlünzen (1996) and Moussiopoulos et al. (2003). Dashed areas in the right column indicate the currently used RANS model resolutions and the resulting possibly resolvable minimum phenomena sizes.

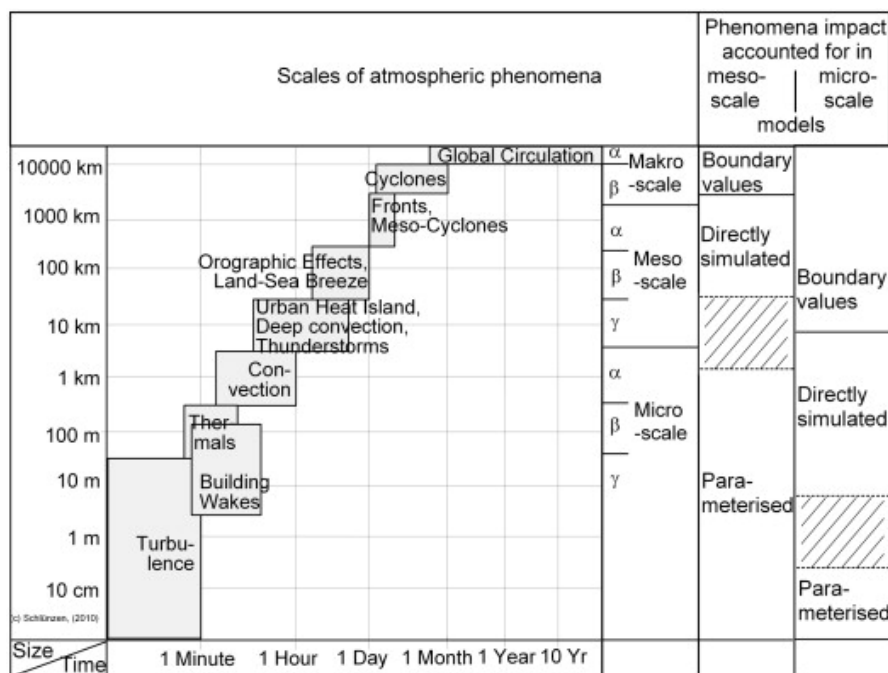


Figure 2.5: Spatial and temporal scales of atmospheric phenomena, Source: Schlünzen et al. (2011)

This kind of model has been developed primarily for weather forecasting and prediction. Like CFD models, mesoscale models also solve the Navier-Stokes equations. Unlike most of CFD models, they include parameterization schemes for solar and infrared radiation, cloud microphysics and convection, soil model, and moreover produce prediction for large domain. In mesoscale modeling, also in the real world, the wind is never in equilibrium with the terrain because of the constant flow of energy into and out of the region, through solar radiation, radiative cooling, evaporation and precipitation, the cascade of turbulent kinetic energy down to the smallest scales and dissipation into heat (Pielke, 1984). They incorporate the dimensions of both energy and time, and are capable of simulating such phenomena as thermally driven mesoscale circulations, tornadoes, boundary layer eddies, sub-microscale turbulent flow over buildings and atmospheric stability. Mesoscale models are used for climate modeling, ocean surface modeling, tropical cyclone modeling, wildfire modeling and more recently in wind energy modeling.

Winds, heat transfer, solar radiation, relative humidity, and surface hydrology are calculated within each grid cell, and the interactions with neighboring cells are used to calculate atmospheric properties in the future. The process of entering observation data into the model to generate initial conditions is called initialization. On land, terrain maps available at resolutions down to 0.1 kilometer are used to help models of atmospheric circulations within regions of rugged topography. The input data are from the observation from measurement masts, weather balloons and weather satellites. Normally the observations are irregularly spaced in the atmosphere, data assimilation along with objective analysis method are used to process these data and obtain values at locations usable by the mesoscale model algorithms.

There are dozen or more mesoscale models currently being used and some of them are listed in the table 2.1. Global model cannot afford to increase the horizontal resolution at particular region of interest. The uses of regional models for weather predictions have arisen to reduce the model errors. Operational

regional models had been embedded or nested into coarser global models. Nesting of regional model requires the use of updated lateral boundary condition obtained from the global model. There are two approaches of nesting, one-way and two-way (Kalnay, 2007).

Table 2.1: List of some mesoscale models

<b>Models</b>	<b>Developers</b>
A2C	YSA Corporation
WRF/MM5	NCAR/Penn. State Univ.
RAMS	Colorado State Univ.
ALADIN	Météo France
SKIRON	University of Athens
BFM	Army Research laboratory
AROME	Météo France
METRAS	University of Hamburg, Germany

### **One-way nesting**

The host model, with coarser resolution provides information about the boundary values to the nested regional model, but it is not affected by the regional model solution. The majority of regional models use one-way lateral boundary conditions. They have some advantages: it allows for independent development of regional model, the host model can run for long integrations without being tainted by problems associated with non-uniform resolution or from nested regional model.

### **Two-way nesting**

Some regional models have been developed using two-way interaction in the boundary condition. The regional solution, in turn, also affects the global solution. This approach seems a more accurate approach than one-way boundary condition, but care has to be taken while the high resolution

information doesn't become distorted in the coarser resolution regions, which can result in worse results overall, especially at longer time scales.

**Berge et al. (2006)** compared and evaluated linear model (WAsP), CFD models (WindSim and 3Dwind) and mesoscale model for a complex terrain site in western Norway. WAsP simulation compared with measurements showed large deviation. Despite the complex terrain, WAsP compared better than the CFD-models to the measurements. Mesoscale simulation with a complete meteorological model indicated large wind variation with the island due to the mountains to the south. The disadvantage of WAsP and CFD models was that mesoscale wind variations were not taken into account in the modeling.

Global data sets are derived from instrumentation deployed on satellites and meteorological data collected by the measurement stations provide the input for mesoscale models (**Sempreviva et al. 2008**). Perhaps the best known of these approaches is the European Wind Atlas project by the European Economic Community (EEC). The European Wind Atlas is founded on meteorological data from a selection of monitoring stations, and shows the distribution of wind speeds at the regional to continental scale. It has been used extensively to estimate the wind resource and its regional variations.

The commercial CFD software for wind resource assessment uses logarithmic wind profile for calculating annual energy prediction for site assessment. Logarithmic wind profile are not site specific and don't have micrometeorological information of wind at the particular site. This causes major source error in AEP calculation. The mesoscale data from operational mesoscale model of a given region can be used as a realistic boundary condition for more detailed microscale modeling. This way the wind characteristics can be determined at a high resolution in an area of interest (**Sempreviva et al. 2008**).

**Badger et al. (2011)** discussed the ways of applying mesoscale modeling in the wind energy sector. They emphasized the need to have a valid link between

mesoscale modeling and microscale modeling, and this is essential for verification of modeling results. [Badger et al. \(2011\)](#) proposed new measurements and analysis that can be used to verify modeling output in new ways, not relying upon verification of wind speed or power density alone. To apply mesoscale model output to give meteorological conditions at a site various routes are proposed.

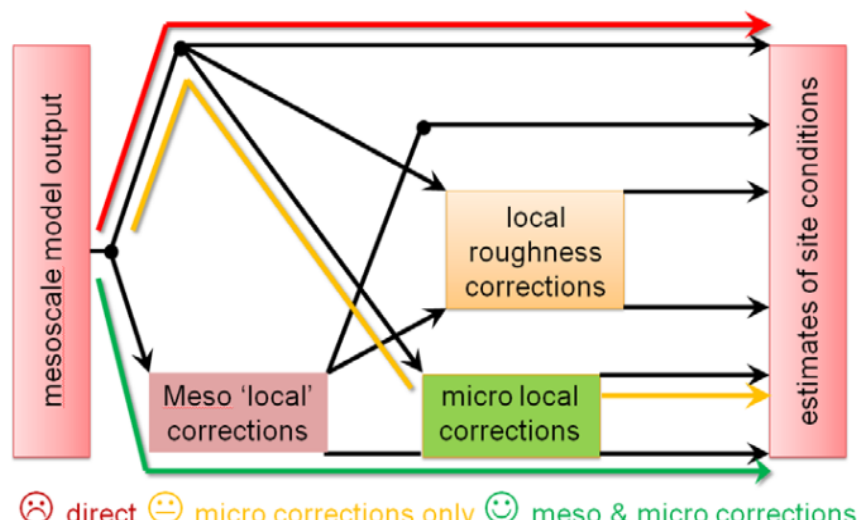


Figure 2.6: A schematic diagram showing the different ways to apply output from mesoscale models to give site conditions, source: [Badger et al. \(2011\)](#)

Figure 2.6 shows the different routes proposed by [Badger et al. \(2011\)](#) ranging from direct application to the more sophisticated route involving corrections at mesoscale and microscale. The route marked in red is a direct route. The route marked in yellow, is semi-direct, in that microscale corrections, as in WAsP, are applied. The green route applies mesoscale and microscale corrections before reaching site conditions. The green route is the recommended way to apply mesoscale model output; all other routes are not recommended. A new measurements technique gives the possibility to verify mesoscale modeling in new ways. [Badger et al. \(2011\)](#) suggested pulsed LIDAR which gives wind speed profiles up to 600 m, which can be used for determining errors and act as mesoscale correction and mast measurements can be used as microscale correction.

#### 2.3.4.5. Coupling mesoscale and microscale modeling

NWP are able to predict the hourly wind regime at resolutions of several kilometers and cannot resolve the wind speed-up and turbulence induced by the topography features finer than 1 km. However, CFD has proven successful in capturing flow details at smaller scales. Hence combining NWP and CFD models can result in a better modeling approach for wind energy applications.

Different methodologies were proposed in the recent past for coupling mesoscale with linear or nonlinear microscale models to predict the wind resource assessment. The application of coupled mesoscale and microscale modeling are used in wind energy resource assessment and in urban pollutant transport and dispersion. [Coirier et al. \(2007\)](#), [Cionco et al. \(2002\)](#), [Tewari et al. \(2010\)](#) and [Yamada et al. \(2011\)](#) used coupled mesoscale and microscale modeling for predicting the urban pollutant transport and dispersion. [Laporte et al. \(2009\)](#), [Rodrigues et al. \(2008\)](#), [Rodrigo et al. \(2010\)](#), [Liu et al. \(2011\)](#), [Badger et al. \(2011\)](#) and [Haupt et al. \(2011\)](#) used coupled mesoscale and microscale modeling for predicting the wind resource for wind energy applications.

[Cionco et al. \(2002\)](#) coupled a mesoscale and a microscale airflow model with the inclusion of surface morphology features which permits further analyses at the neighborhood scale. With the higher resolution mesoscale output, the microscale was then able to generate a very detailed airflow analysis in the localized area. During unstable condition, the results showed significant terrain influence. And with the inclusion of urban morphology, the microscale solution exhibits even greater variation in the flow field. [Cionco et al. \(2002\)](#) results reveal that the flow field is further influenced by the non-uniform urban structures.

Coirier et al. (2007) present the progress towards the development of coupled mesoscale-to-microscale modeling capability for the urban regime in which they couple the WRF model to high-resolution CFD model (CFD-ACE+/CFD-Urban) using the Model Coupling Environmental Library (MCEL). The MCEL utilizes a data flow approach where coupling information is stored in a centralized server and flows through processing routines called filters to the numerical models. Figure 2.7 shows the diagram illustrating the coupling approach envisioned for coupling WRF and CFD by Coirier et al. (2007). The lid-driven cavity computation performed by Ghia et al. (1982) have been used quite extensively to validate CFD models, where profiles of velocity at various locations are provided for Reynolds number based on lid length and speed. Computed results are validated with the recognized computational results of Ghia et al. (1982) and to the results of CFD-ACE+/CFD-Urban. The results are more accurate as well as more efficient with CFD-ACE+/CFD-Urban and match well with Ghia et al. (1982) results.

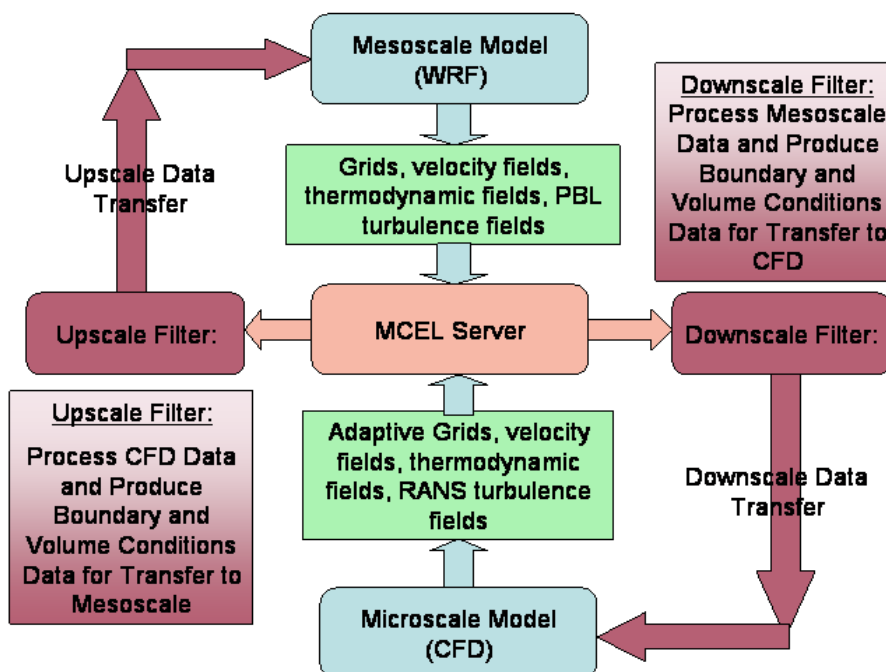


Figure 2.7: WRF-MCEL-CFD Coupling Conceptual: Initial model, Source: Coirier et al. (2007)

Rodrigues et al. (2008) presented an application of coupling a NWP model combined with CFD to improve power forecasting. The weather forecasts from the NWP are related to the power output of each turbine, using transfer function and a power curve. The wind velocity and direction from NWP are referred to a reference location within the wind farm. A transfer function establishes the relation between wind conditions at the reference location, with those at each turbine location. This transfer function was obtained from large set of CFD simulation of the flow field, covering several wind directions and velocities. Using NWP outputs, Rodrigues et al. (2008) evaluated the wind speed and the direction at the reference mast and were able to predict the production up to 72 hours ahead. Figure 2.8 shows the application of coupled methodology for power forecasting by Rodrigues et al. (2008).

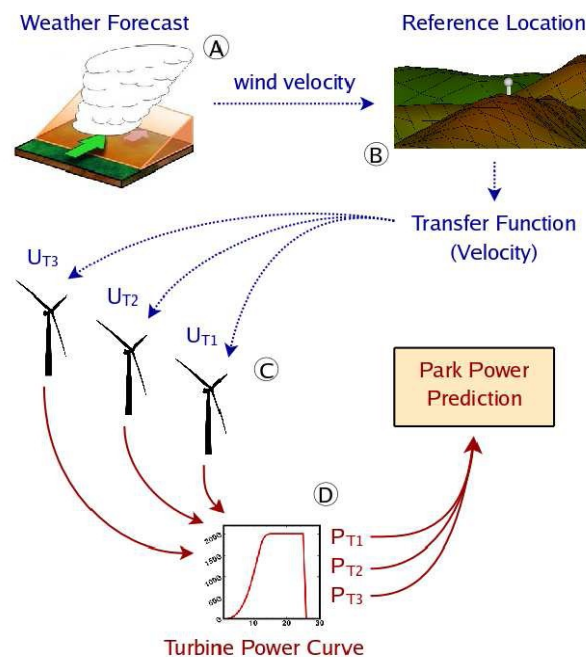


Figure 2.8: coupled methodology for power forecasting, Source: Rodrigues et al. (2008)

The methodology proposed by Laporte et al. (2009) is based on four steps: measurement campaign, mesoscale meteorological modeling database, clustering and microscale atmospheric CFD. Mesoscale model used in this

methodology is ALADIN (<http://www.cnrm.meteo.fr/aladin>) but it can be applied with any mesoscale model. Clustering is an unsupervised classification of patterns into groups. The clustering problem has been addressed in many contexts and in many disciplines; this reflects its broad appeal and usefulness as one of the steps in exploratory data analysis. The inlet conditions for the CFD simulations are built combining meteorological mast measurements with mesoscale model data. The microscale CFD model is then used to calculate the wind fields for the situations selected with the clustering. Figure 2.9 shows the four-step methodology used for the wind resource assessment. The *k-mean* clustering process is used, where the number of situation to simulate has been dramatically reduced in order to perform the entire computational in reasonable time.

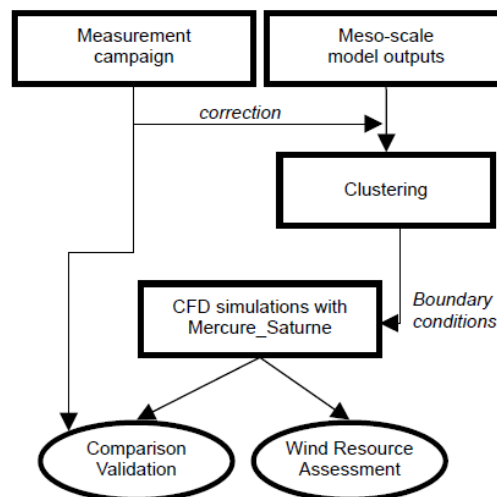


Figure 2.9: Wind resource assessment methodology, Laporte et al. (2009)

Tewari et al. (2010) conducted a very high-resolution numerical modeling study over the complex terrain and complex urban area in Salt Lake City. Tewari et al. (2010) studied the impact of coupling a microscale CFD with a NWP model on urban scale contaminant transport and dispersion. It was found out that microscale CFD model prediction was significantly improved when using the wind field produced by downscaling WRF output as initial and boundary

condition. The key reason for this significant improvement in the coupling is that turning of lower boundary layer wind and pressure gradient are well represented in the time varying 3D WRF fields.

**Rodrigo et al. (2010)** proposed a methodology for producing regional wind maps with horizontal resolution of 100m or lower from mesoscale meteorological database and CFD modeling. **Rodrigo et al. (2010)** methodology uses physical downscaling with CFD model that links geostrophic winds, from a meteorological database, with surface wind through a more detailed characterization of the topography and the vertical structure of the atmospheric boundary layer. This methodology was applied to obtain the wind atlas of Granada region in Spain and **Rodrigo et al. (2010)** showed the comparison with synoptic stations, the advantage of the increased resolution in predicting the wind speed in the exposed area using coupling method.

**Yamada et al. (2011)** addressed the differences in the purposes and approaches of mesoscale meteorological model (MMM) and CFD model and to identify issues and explore ways of coupling MMM and CFD modeling capabilities. The incorporation of meteorology into CFD is an important issue, assumption, such as steady state and thermal homogeneity needs improvement. The real atmosphere is never in steady state and temperature stratifications plays important roles. The MMM horizontal grid spacing is much larger than in CFD, and smaller grid spacing in CFD means more topographical features are included than in MMM. So linear interpolation of surface temperature distribution of MMM to CFD is not accurate; ideally ground temperature should be computed in CFD in a similar fashion as in MMM (i.e., 1D heat conduction equation solved for soil layer with appropriate boundary condition).

CFD adopts both structured and unstructured grid system but MMM uses the structured grids only. Interpolation of variables from the structured to unstructured introduces errors. **Yamada et al. (2011)** gave overview of possible

ways of application of mesoscale modeling in microscale model. Two-way coupling requires modification in programming for both MMM and CWE, which is difficult since it requires interaction between two different structures and hence one-way coupling is justified. Yamada et al. (2011) also performed nudging of winds and temperatures at all grid points in the typhoon simulation using WRF and A2C (MMM with CFD capabilities). A2C simulation couldn't simulate airflow around the building very well, if only winds and temperature are provided by WRF. But nudging changes the wind direction in A2C simulation by 300° with the movement of the typhoon.

Liu et al. (2011) implemented a multi-scale weather model, which is designed for simulation of weather process from synoptic scale to microscale with simultaneous nested grids. Figure 2.10 shows the configuration of multiple nested-grid model domains for simulation of microscale flow at the northeastern Colorado wind farm. Domain 1 covers large areas of the USA. Color shades in Domain 3 –7 represent the terrain height, red for highest terrain, blue and gray for lower terrain. The different color scales are used for different domains to emphasize the terrain features resolved by each domain.

Real-Time Four Dimensional Data Assimilation (RTFDDA) weather forecasting system was developed in WRF by Liu et al. (2011) to support regional and local application. RTFDDA system employs a Newtonian relaxation approach to continuously nudge the model state towards all available observations with weights specified as functions of space and time according to observation location and time. RTFDDA, built upon WRF is a rapid cycling weather forecasting system with the capability of effectively combining all available weather observation with the full physics WRF model to produce accurate multi-scale 4D weather information from synoptic scale to microscale.

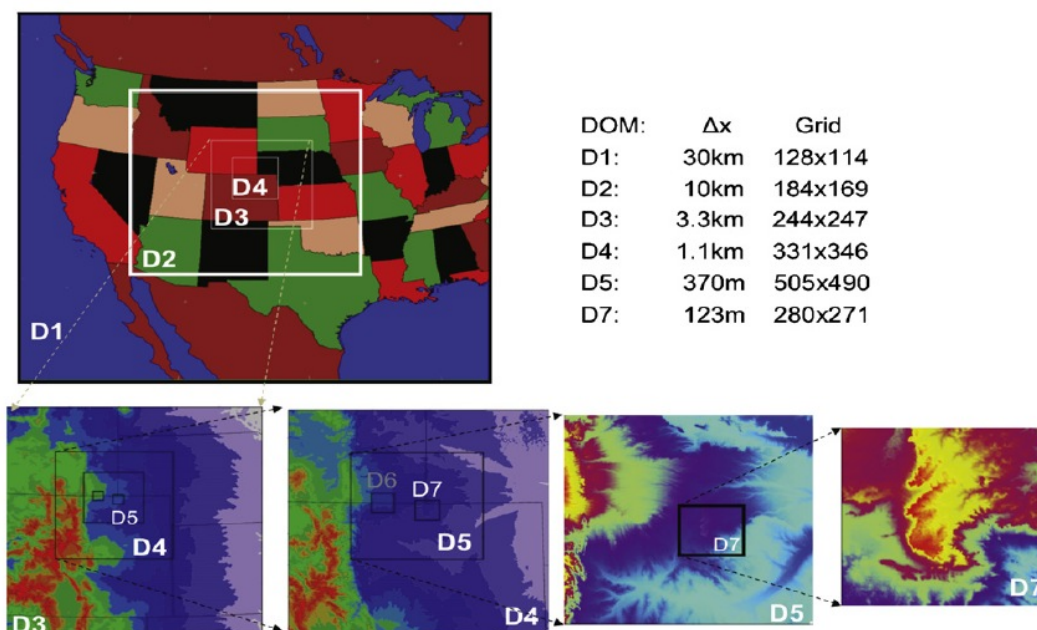


Figure 2.10: Configuration of multiple nested-grid model domains for simulation of microscale flows at the Northeastern Colorado wind farm, Source: Liu et al. (2011)

The system obtained dynamic balance and physical consistency between measured data and numerical solution of the model. WRF–RTFDDA has been further developed to simulate small- and micro-scale circulations on LES scale grid and the new system is referred to as WRF–RTFDDA–LES. It is designed for multi-scale modeling down to microscale weather processes for focused geographical areas. WRF–RTFDDA–LES makes use of simultaneous nest-down approach with fine-mesh domains running at LES scale. The model simulates mesoscale weather on the coarser grids ( $\Delta x=4.5$  km) with a planetary boundary layer (PBL) parameterization along with other model physics parameterizations and FDDA. The FDDA component of the model provides an advanced data assimilation algorithm that was capable of effectively assimilating diverse weather measurements on the mesoscale model grids, and thus produces accurate realistic initial conditions and continuous updates of the environmental forcing to the fine-scale LES modeling through the lateral boundaries.

Haupt et al. (2011) investigated the procedure for assimilating mesoscale model data into a CFD simulation. Haupt et al. (2011) used the spatially varying WRF data as inflow condition for Acusolve CFD code and assimilated vertical wind profiles of the fine-scale WRF data into the CFD model in order to nudge the CFD solution towards the WRF model data. Haupt et al. (2011) results of this study demonstrated that it's possible to nudge the wind profile towards the WRF while retaining the mass consistency of the CFD model.

Table 2.2 shows the list of publications that use coupled mesoscale and microscale modeling for the wind energy and urban pollutant transport and dispersion. Almost all of the articles mentioned here used simple turbulence model like RANS  $k-\epsilon$ , WRF mesoscale model is used in most of the cases, boundary conditions are downscaled using 1 way nesting approach and duration of the simulation is based on the availability of data and specific needs. Some articles used microscale correction for the mesoscale data and validations of the results are very limited. To conclude coupling mesoscale and microscale modeling can predict wind fields properly when compared to mesoscale and microscale modeling separately. Nudging used in microscale model showed good improvement in the prediction. But it seems that up to now there is not any published work for wind energy application in which field measurements have been nudged in a CFD simulation.

Table 2.2: List of publications that use coupling mesoscale and microscale modeling.

Author's	Mesoscale and microscale model	Mesoscale model	Microscale model	Turbulence model	Nesting/ Boundary condition- Correction/No Correction	Long term statistics or duration	Application
Berge et al. (2006)	Not - coupled	WRF	WindSim 3Dwind	RANS $k-\epsilon$	---	---	Wind energy
Coirier et al. (2007)	Coupled	WRF	Urban CFD	RANS $k-\epsilon$	1 way nesting	16/07/2003 1200 UTC	Urban
Laporte et al. (2008)	Coupled	ALADIN	Code-Saturne	RANS $k-\epsilon$	Correction BC	Clustering	Wind energy
Rodrigues et al. (2008)	Coupled	WRF	VENTOS	RANS $k-\epsilon$	1 way nesting	123 wind classes	Wind energy
Cionco et al. (2002)	Coupled	BFM	HRW	(RANS)	---	18/01/1998	Urban
Tewari et al. (2010)	Coupled	WRF	CFD-Urban	RANS $k-\epsilon$	1 way nesting	25/10/200 0000 UTC	Urban
Rodrigo et al. (2009)	Coupled	SKIRON	CFDWind	RANS Mixing $k-l$	1 way nesting	12 wind classes	Wind energy
Yamada et al. (2011)	Coupled	A2C	FITNAH	RANS, LES	1&2 way nesting	48 hours	Urban
Liu et al. (2011)	Coupled	WRF	NCAR-LES	LES	1&2 way nesting	14/11/2008 0000 UTC - 15/11/2008 1700 UTC	Wind energy
Haupt et al. (2011)	Coupled	WRF	AcuSolve	URANS Spalart-Alamaras	1 way nesting	31/12/2008 2100 UTC	Wind energy

#### **2.3.4.6. Coupling mesoscale and microscale model and field measurements assimilation**

The main objective of the methodology proposed in this work is to assess accurately the available wind energy potential for a wind farm site. This methodology is an improved version of the previous methodology used in the work carried out (Laporte, 2008) at EDF R&D. Main differences between the two methodologies are:

- A new coupling method is developed and implemented to impose the inlet boundary condition on the CFD domain.
- Field measurement data are assimilated inside the CFD domain.
- Wind resource assessment is carried out for CFD simulation without assimilation and CFD simulation with assimilation.

This methodology is specifically developed to handle very complex topography as more and more wind farm are developed in complex terrain but it can also be used for other flat terrain and moderately complex terrain. The hourly operational data of the mesoscale model are obtained from the French meteorological center. The analysis is carried on yearly basis, as the ultimate objective is to calculate the AEP of the wind farm site. Then the hourly mesoscale data is classified using the *k*-means clustering method. The hourly mesoscale data are then grouped into a certain number of clusters, which is a representation of the annual wind distribution.

To impose the mesoscale data on the microscale domain boundaries, three methods are developed: Translation, Extrapolation and Cressman interpolation. All the methods are explained in the chapter 3. Cressman interpolation is then used for all CFD simulations for all the cluster centers. To incorporate the field measurement into CFD domain, data assimilation technique (nudging) is implemented into the CFD code. Simulations were carried out for the same cluster centers without and with nudging. Figure 2.11 shows the detailed flow chart of the methodology using assimilation, black color route shows the CFD

simulations using Cressman interpolation without assimilation and red color route shows the CFD simulations using Cressman interpolation with assimilation.

Firstly, implementation and validation of CFD simulations without assimilation and with assimilation are carried for several directions. Good field measurement data set is available for input data and validation for the nudged model. Cup anemometer data is chosen for assimilation at one of the mast location, as it is an industrial standard and widely used instrument in wind resource assessment. Additional measurements at this location are used for validation. The influence of the field measurement assimilation in CFD simulation is validated using other available masts.

The annual average wind speed is then calculated at mast locations for both CFD simulations without assimilation and CFD simulations with assimilation. The simulation results are compared with the field measurement annual average and with linear model - WAsP. Annual average wind speed map at 80m above the ground level is also created for the both CFD simulations without assimilation and CFD simulations with assimilation.

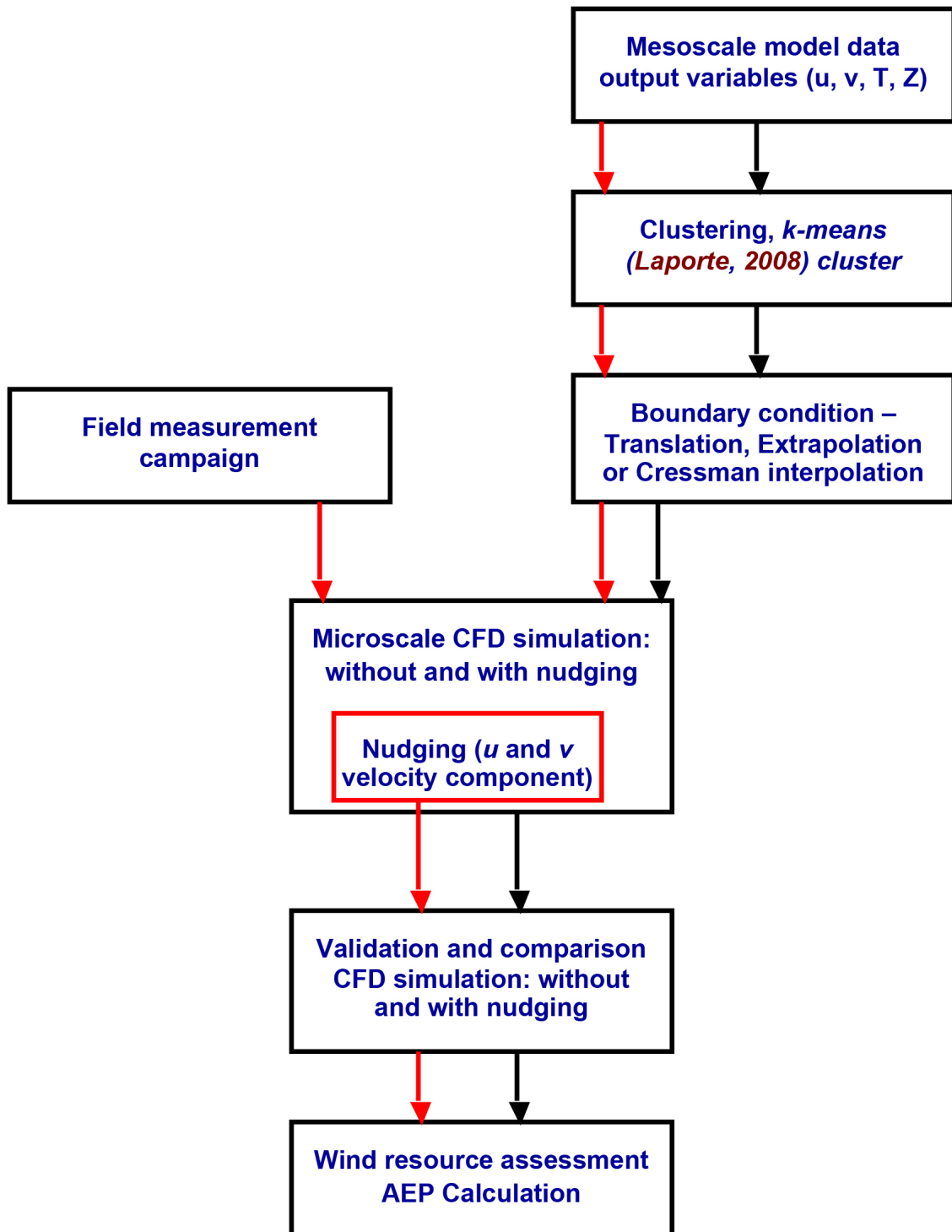


Figure 2.11: Methodology for calculating AEP without and with assimilation

### **3. Modeling procedure for coupling mesoscale and microscale models**

This chapter gives details of the necessary elements of coupled mesoscale and microscale modeling methodology for the wind resource assessment.

#### **3.1. Measurement Campaign**

This section gives the description of the site, land use, measurements equipment installed and meteorological conditions at the site.

##### **3.1.1. Site description**

The site selection was done in collaboration between EDF R&D and EDF-Energies Nouvelles (EDF-EN). The area of interest is located in southern France and for confidential reasons the exact location of the wind farm site cannot be mentioned. Figure 3.1 shows the elevation map of the complete site (40x40 km<sup>2</sup>), the inner domain of (20x20 km<sup>2</sup>) chosen for computation and mast locations. Three masts were installed at the site at M80, M and FP. The site is considered to be very complex with strong slopes, valleys and forest. Slopes are locally larger than 30° and more than 80% of the site is covered with forest inside the 20x20 km<sup>2</sup> domain. The trees are about 7-10 meters height around the measurement areas.

The average altitude of the site is 700 m. The site is located at the centre of the figure 3.1 with plain in southeast, valley on the Northwest and further to the Northwest a plateau at altitude of 1100 m. The digital elevation map and land use file have resolution of 25 m and 50 m respectively and were obtained from IGN (Institut Géographique National, France). Figure 3.2 shows the roughness index of the site.

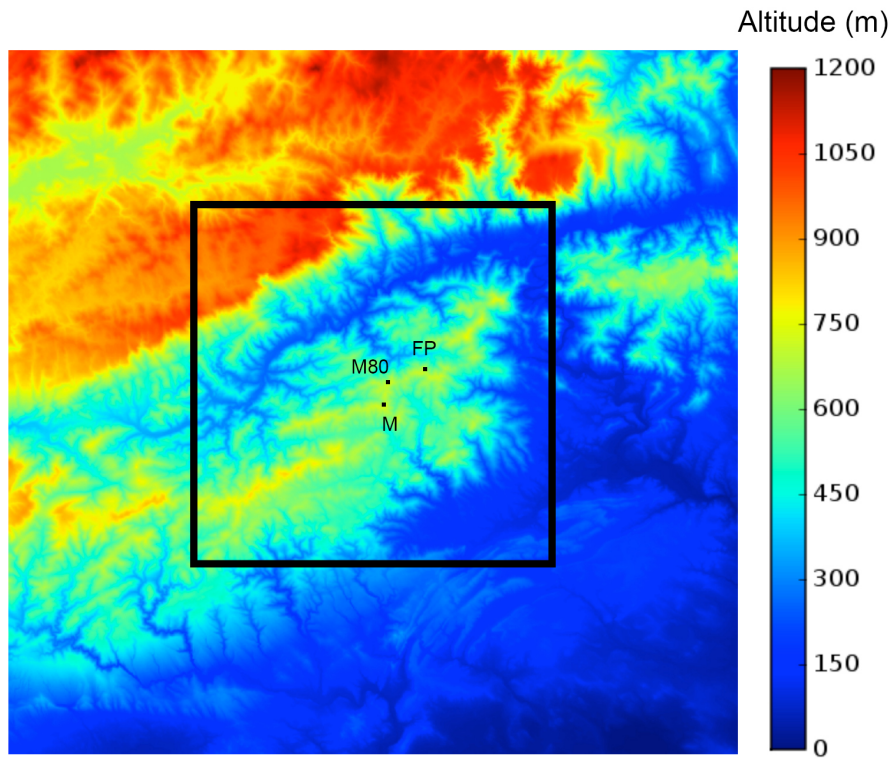


Figure 3.1: Digital elevation map (DEM) of the site along with the three mast locations.

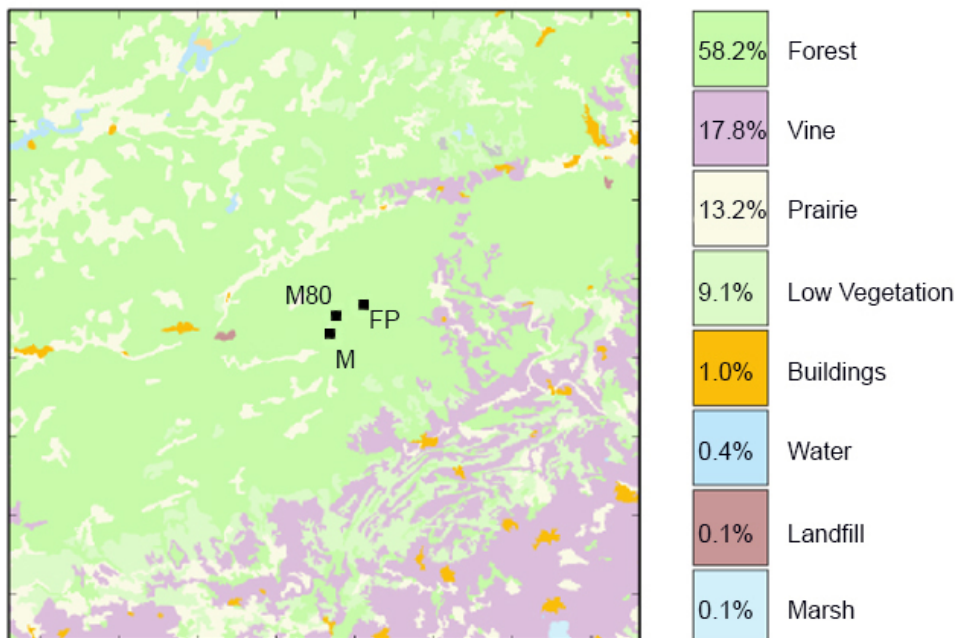


Figure 3.2: Roughness index of the site and locations of the three masts.

### 3.1.2. Measurement campaign

A one-year field measurement campaign was led by EDF R&D and EDF EN between June 2007 and June 2008 in order to provide input and validation data to this methodology. The measurement set-up included 2 sodars, two 50 m masts (M and FP) with cup anemometers and vanes, and an 80 m mast (M80) with cup and sonic anemometers, vanes, temperature and humidity sensors. A Remtech PA2 sodar was installed besides the 50 m M mast in order to provide the vertical profile of wind and turbulence between 100 m and 600 m.

Table 3.1: Description of instruments deployed at the site

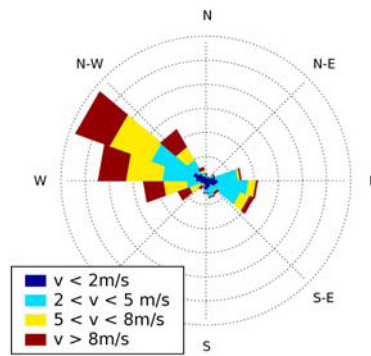
Location	Instruments	Height of measurements	Period of measurements
M	Cup anemometer	29, 39, 49, 49 m	From 2007 to 2008
	Vanes	29, 47 m	
	Sodar PA2 Remtech	100 to 600 m (every 50 m)	From 2 August 2007 to 7 July 2008
FP	Cup anemometer	30, 39, 49, 49 m	From 2007 to 2008
	Vanes	30, 47 m	
M80	Cup anemometer	40, 50, 65, 82 m	From 2007 to 2008
	Vanes	50, 75 m	
	Sonic Anemometer	10, 25, 45, 78 m	From 15 June 2007 to 7 July 2008
	Sodar SFAS Scientec	30 to 130 m (every 5 m)	From 12 October 2007 to 23 May 2008

A Scintec SFAS sodar, which provided the vertical profile of wind and turbulence between 30 m and 130 m, was located near the M80 mast. It had to deal with very difficult working condition (M80 mast and trees are located nearby), which explains the low vertical range and some doubtful

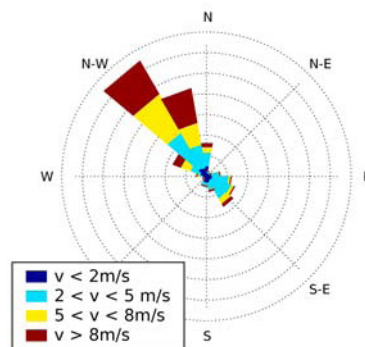
measurements. Four sonic anemometers installed on the M80 mast measured the three components of the wind with a sample rate of 10 Hz. Their mean values over 10 minutes, and standard deviation were calculated. Table 3.1 shows the list of the measurement locations, instrument device used, height of measurement and period of measurement. Access to electricity network was not possible in this area, so an autonomous device of power supply has been used which included 10 batteries, 10 solar cells and 4 small wind turbines.

### **3.1.3. Meteorological conditions**

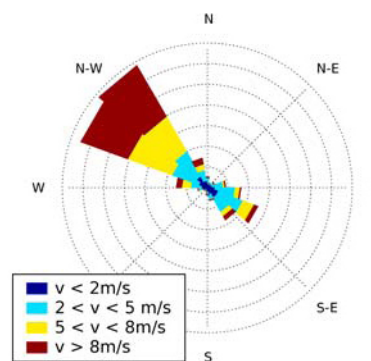
Figure 3.3 shows the wind rose and magnitude measured by the three meteorological masts M80 (80 m), M (50 m) and FP (50 m). The wind flow in the site is characterized by dominant northwesterly direction with higher wind speed and secondary southeast direction far less frequent with lower wind speed. The figure 3.3 also shows that the wind roses are not identical between the three masts. This could be due to the influence of the topography and complex flow phenomena over the site. Most of the available wind energy is contained by the northwesterly direction and slightly in southeasterly. The analysis of the sonic and sodar measurement data reveals that the SFAS sodar underestimated the wind speeds by about 12% in average when compared to the sonic anemometers which is partly due to the complex terrain. The ratio between sodar and sonic wind speed is highly dependent on the wind direction and is linked to the topography (Dupont et al., 2009).



a) M80



b) M



c) FP

Figure 3.3: Wind rose and magnitude from cup anemometer measurements at  
a) M80, b) M and c) FP

### 3.2. ALADIN - Mesoscale data extraction

The mesoscale model used for this methodology is ALADIN (Aire Limitée Adaptation dynamique Développement InterNational), which was developed and operated by several European and North African countries under the leadership

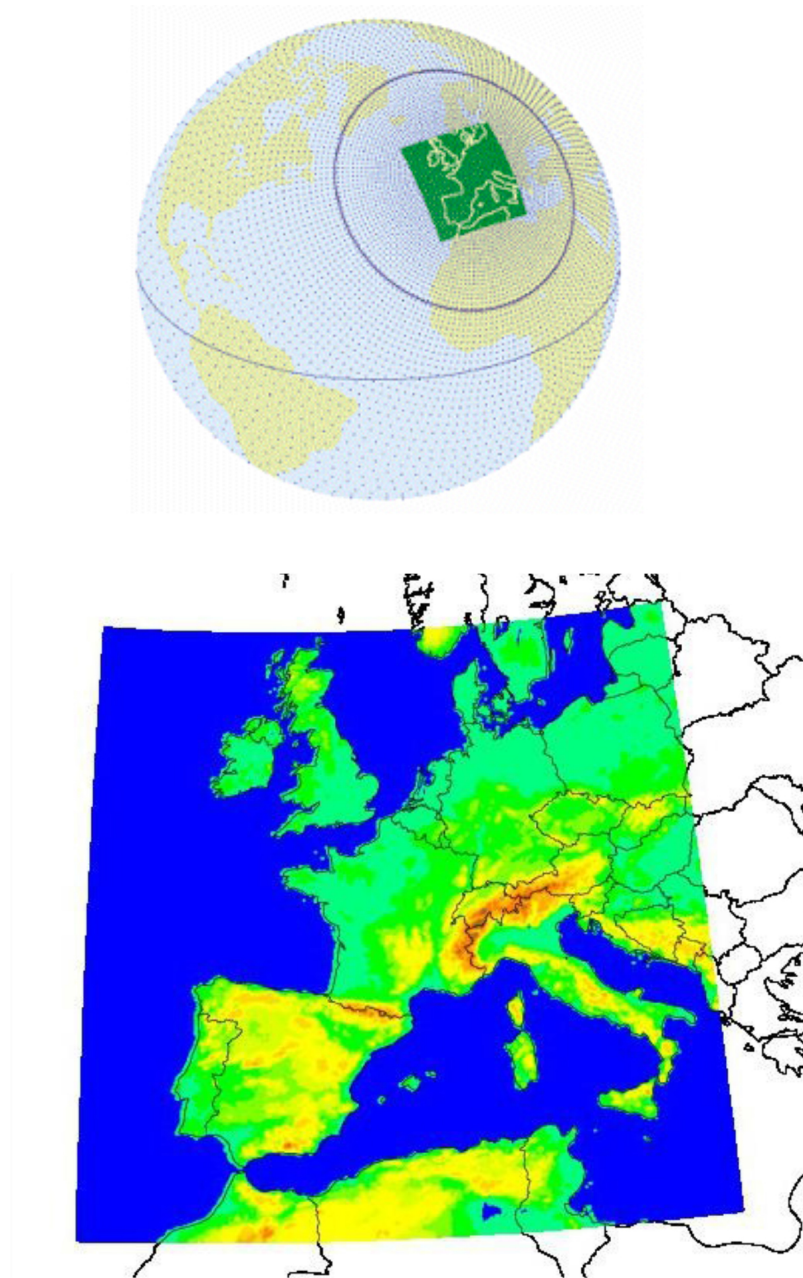


Figure 3.4: ARPEGE (top) and ALADIN (bottom) domain

of Météo-France. It maintains a NWP system for use on limited geographic areas, with small domains and high spatial resolution. The important meteorological events at fine scale (local winds, breezes, thunderstorms lines) are the main results of the dynamical adaptation to the characteristics of the earth's surface. It received boundary data from the ARPEGE, French global model.

During a forecast, ALADIN-France was coupled with ARPEGE every 3 hours. The center of the ALADIN domain was located at 46.47°N; 2.58°E. The horizontal resolution of ALADIN grid is approximately 9 km with 31 vertical levels. 4 runs were performed operationally each day at 00, 06, 12 and 18 UTC. Forecast terms were 54H for the 00 UTC forecast, 48H for 06 UTC, 42H for 12 UTC and 36H for 18 UTC. The assimilation scheme was 3D-Var with a 6-hour window. Coefficients for variation bias correction (applied to satellite observations) were computed by ARPEGE. In the present case, analyses are available at 0h and 12h and forecasts between 1h and 11h and between 13h and 23h with a one-hour step. A new forecast is produced every 12 hours, while the longest range of the forecast is 48 hours ([www.cnrm.meteo.fr/aladin/](http://www.cnrm.meteo.fr/aladin/)). Figure 3.4 shows the domain of ARPEGE global French model and ALADIN mesoscale model.

Météo-France provided the hourly wind speed and temperature profile for the year 2007, turbulent kinetic energy ( $k$ ) and dissipation ( $\varepsilon$ ) are deduced from the mesoscale profile using neutral similarity law for the surface layer (Stull, 1988) as follow:

$$k = \frac{u_*^2}{\sqrt{C_\mu}} \quad (3.1)$$

$$\varepsilon = \frac{u_*^3}{\kappa(z + z_0)} \quad (3.2)$$

$$U = \frac{u_*}{\kappa} \ln \left( \frac{z + z_0}{z_0} \right) \quad (3.3)$$

Where  $U$  is ALADIN velocity at 10 m,  $u_*$  is the frictional velocity,  $z_0$  is the roughness length,  $z$  is height above ground level, and  $\kappa$  is the Von Karman

constant ( $\kappa=0.4$ ). The operational ALADIN runs provide the initial and boundary condition for the CFD code *Code\_Saturne*. From March 27, 2012 ALADIN-France completed its last operational run (5860 days since its first pre-operational run; 5100 days since its first operational run), at Météo-France. However, the methodology developed in this framework can be applied with any mesoscale model.

### **3.3. Coupling mesoscale and microscale models**

At present, all the commercial wind resource assessment CFD packages use logarithmic profiles for different wind direction sectors and this leads to uncertainty in the annual energy prediction. However, using mesoscale data as inlet boundary condition has proven in many cases in the recent research to be a better approach for calculating AEP in wind farm. Mesoscale model data can be used either from the operational mesoscale model, which already exists from the weather forecasting, or specialized mesoscale model runs are carried out for wind energy application with finer resolution. These fine resolution runs are usually carried out for application research and are expensive and time consuming. For the presented methodology operational mesoscale model runs data are used. Figure 3.5 shows the location of the ALADIN mesoscale grid points and area of the computational domain (black box - 20X20 km<sup>2</sup>) with potential wind farm site located at the center.

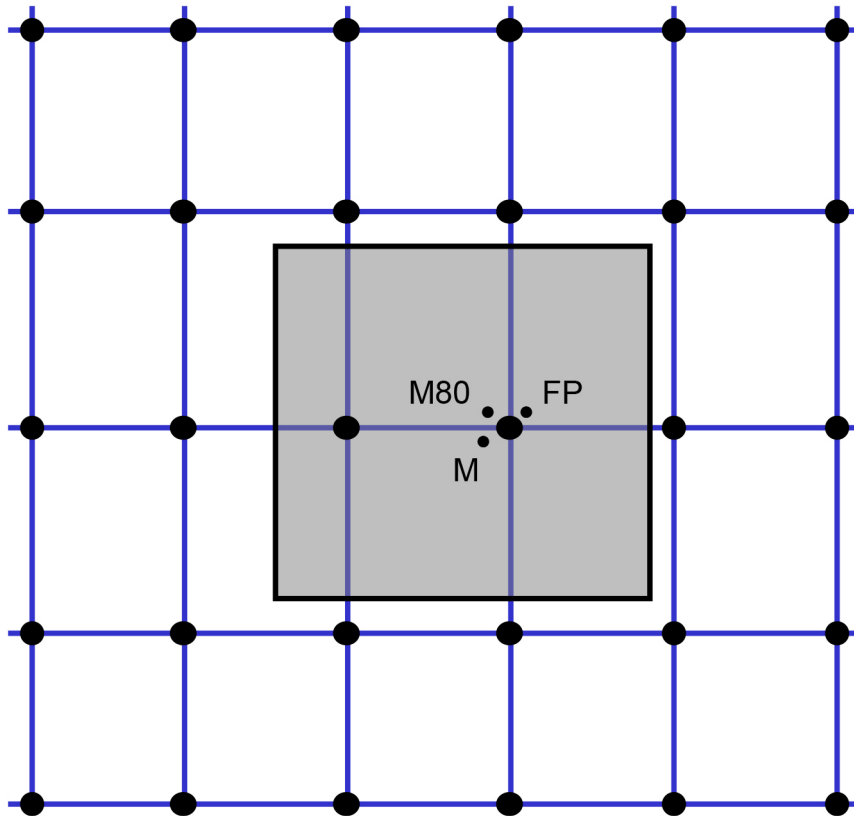


Figure 3.5: CFD simulation domain and surrounding operational ALADIN mesoscale grid points.

### 3.4. Clustering

Clustering is a process of grouping similar objects into groups (clusters). Clustering as a task is used in many fields, machine learning, pattern recognition, image analysis, bioinformatics and information retrieval (Jain, 1999). The purpose of clustering is to reduce the number of CFD simulations that have to be performed in order to insure long-term representativeness. Indeed, a first solution to insure this long-term representativeness would be to carry out a CFD simulation for each hour of the year, which would lead to a number of 8760 situations. Carrying out CFD simulation for 8760 situations would only be possible for a very small grid with too low resolution. Clustering method reduces dramatically the number of CFD simulation needed to reproduce 1 year of atmospheric flow over the site. An unsupervised clustering

method was selected, leading to real situations as representative clusters. This gives the possibility to compare the performance of the CFD simulation results with measurements for each individual selected situation (Laporte, 2008).

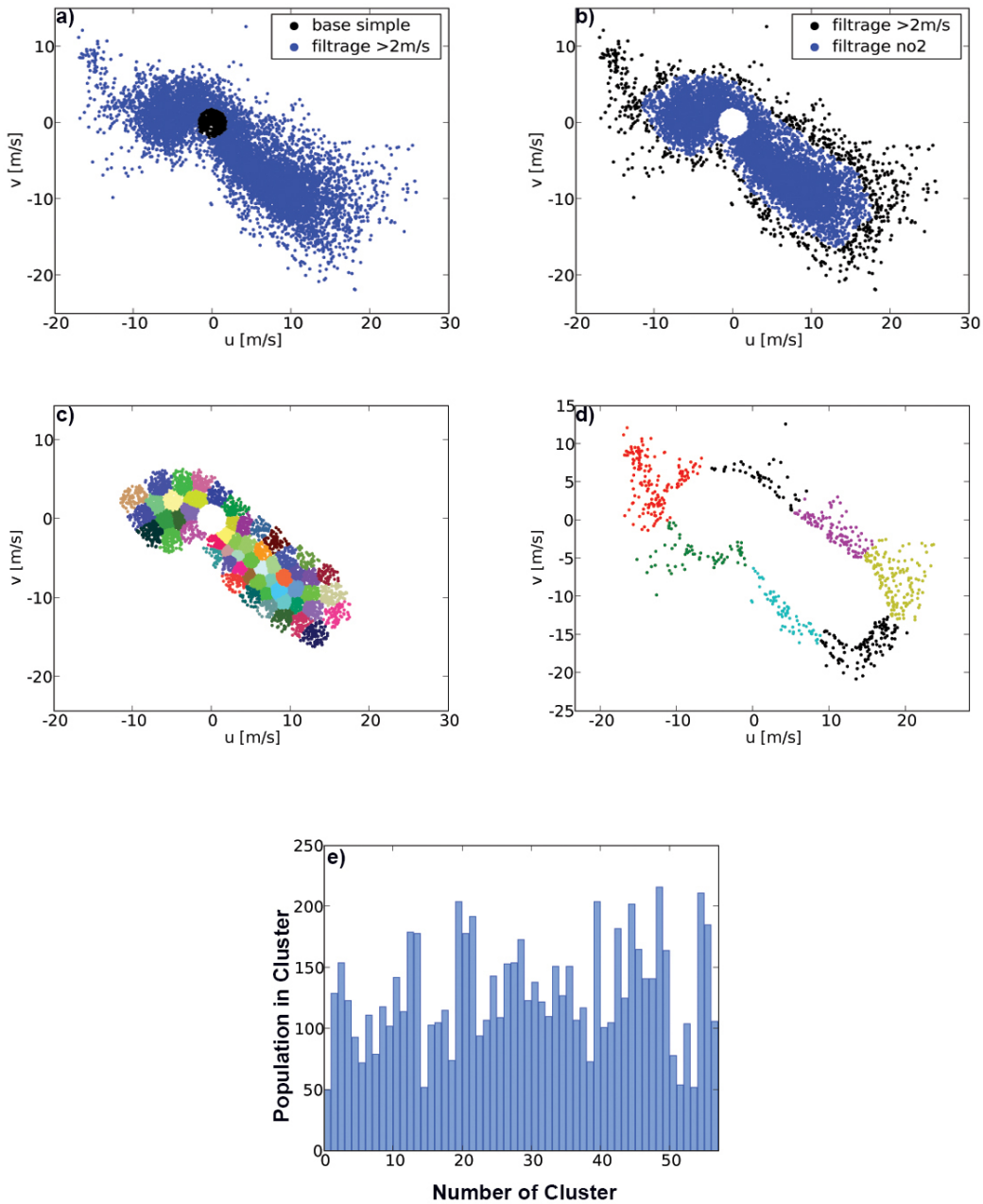


Figure 3.6(a-e): The k-means clustering process in the  $(u, v)$  wind speeds component plane, Source: Laporte (2008)

The clustering process carried out by Laporte, (2008) has been used with the new methodology of coupling mesoscale and microscale models. Some of the

important details of the clustering process of Laporte (2008) are discussed. The *k-mean* partition method was used; it's a popular algorithm, easy to implement and fast to compute. The horizontal components of the wind speed ( $u$ ,  $v$ ) provided by ALADIN at 100 m level (considering a particular vertical or an average over the 10 verticals close to the domain center) are used as variables to describe the meteorological situation. Situations with the wind speed lower than 2 m/s and greater than 25 m/s, corresponding to situations in which wind turbines do not produce electricity, are filtered before the clustering process. Euclidian distance in the ( $u$ ,  $v$ ) plane is used to measure the similarity of 2 situations.

Figure 3.6(a-e) shows the clustering process, how the raw filtered data (figure 3.6a) are grouped, situations with less dense group (outliers) are separated and clustered separately (figure 3.6d) as it can alter the quality of the clustering. Situations in the very dense group are then clustered (figure 3.6c). Figure 3.6e shows the population of each cluster. After the clustering process, 64 situations (57 main cluster and 7 outliers) corresponding to the 64 cluster centers were chosen for CFD simulation. Further information about this clustering process for wind resource assessment can be obtained in Laporte (2008, 2009).

### 3.5. Microscale CFD Model

The microscale CFD simulation requires three main elements: pre-processor, solver and post-processor. Pre-processor for wind resource assessment consists in defining the topography, computational domain, grid generation, land use cover and boundary condition. The accuracy of a CFD solution depends on the number of cells in the domain, so grid independence study was conducted to optimize the grid.

The solver used in most of the commercial CFD code and also in *Code\_Saturne* is finite volume method. It consists in: formal integration of the governing equation of fluid flow over all the control volumes of the domain, discretization

involving the substitution of finite-differences, finite-volumes-or finite-elements type approximation for the terms in the integrated equation representing flow processes (converts the integral equation into system of algebraic equation), solution of algebraic equation by an iterative method. The control volume integration expresses the conservation of relevant properties for each finite volume and this is one of the main advantages of the finite volume approach.

The CFD codes contain discretization techniques for advection, diffusion, source terms and rate of change with respect to time. The underlying physical phenomena are complex and non-linear so an iterative solution approach is required. The most popular solution procedures are the TDMA (Tridiagonal Matrix Algorithm) line-by-line solver of the algebraic equation and the SIMPLE algorithm to ensure correct pressure and velocity coupling.

In post-processor, data visualization of the CFD solution is carried out using domain geometry, grid display, line plots, 2D and 3D surface plots, vector plots, and particle tracking for analysis the CFD results. The section 3.5.3 explains the necessary elements of CFD modeling for wind resource assessment.

### **3.5.1. Topography and domain**

Topography is a very important part, on which the simulation domain is created and the size of the boundary layer is defined. A 40x40 km<sup>2</sup> Digital Elevation Map (DEM) is obtained from IGN, which contains the site to be analyzed. The DEM is cropped to 20x20 km<sup>2</sup> such that potential wind farm site is located at the center of the topography. The objective is to construct a computational domain with fine resolution (25 m) at the center, where the nudging model is applied and coarse grid (100 m) near the boundaries. The boundaries at the four lateral sides of the domain are gradually smoothed to ensure smooth inflow without overshooting of high velocities.

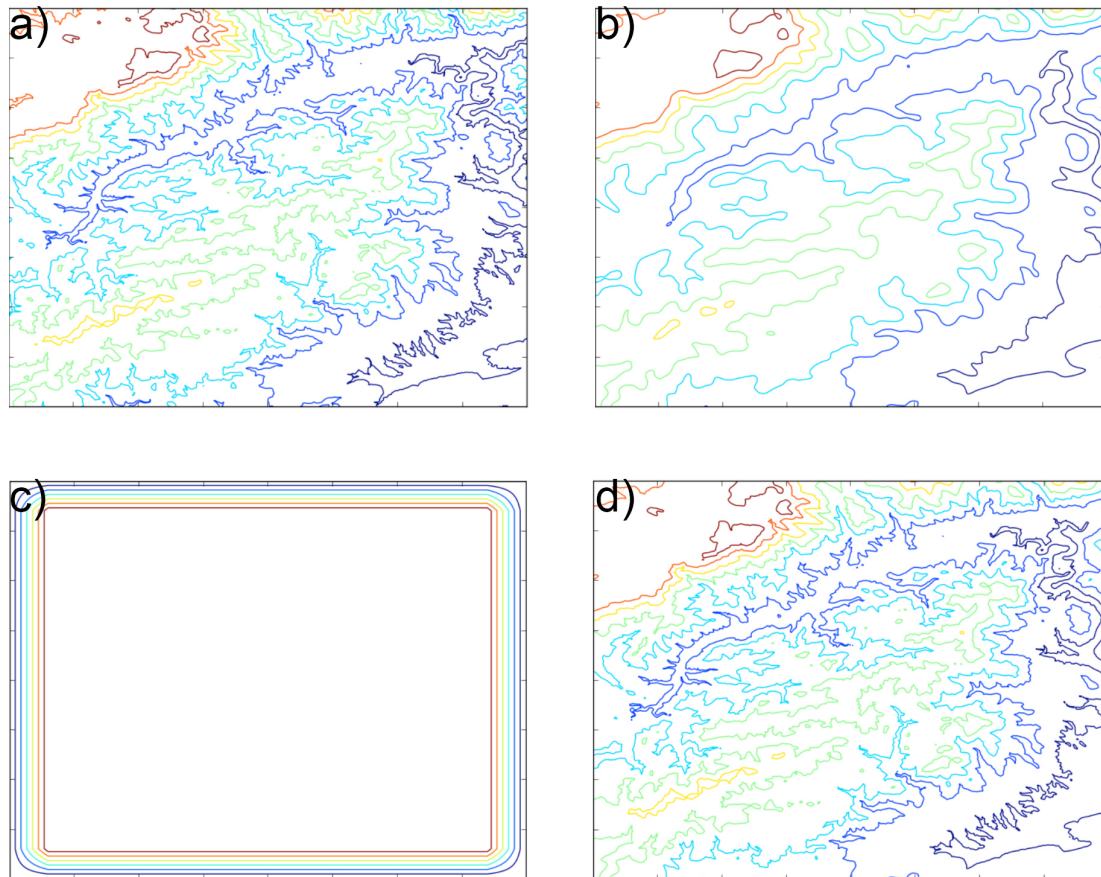


Figure 3.7: (a) Contour map of the DEM of topography with fine 25 m resolution, (b) Contour map of the DEM of topography with coarse 100 m resolution, (c) weight function applied for gradual change in topography resolution, (d) mixed topography with fine resolution at the center and coarse at the border.

Topography is built from the DEM with resolution of 25 m for the center part ( $17 \times 17 \text{ km}^2$ ) and gradually smoothed to 100 m towards the border (1.5 km) on the 4 sides. Figure 3.7.a shows the topography built using fine resolution DEM of 25 m, figure 3.7.b show the topography built using coarse resolution of 100 m, figure 3.7.c shows the weight function for the whole topography, where the boarder 1.5 km are gradually smoothed to the boundary. Figure 3.7.d shows the mixed topography of fine resolution at the center and coarse at the border. The sides are smoothed in order to avoid high velocity at the entrance of the domain caused by cell skewness. Figure 3.8 shows the final topography with smoothed

borders. Figure 3.9 shows the created computational domain with highest level at 6000 m, next step is grid generation.

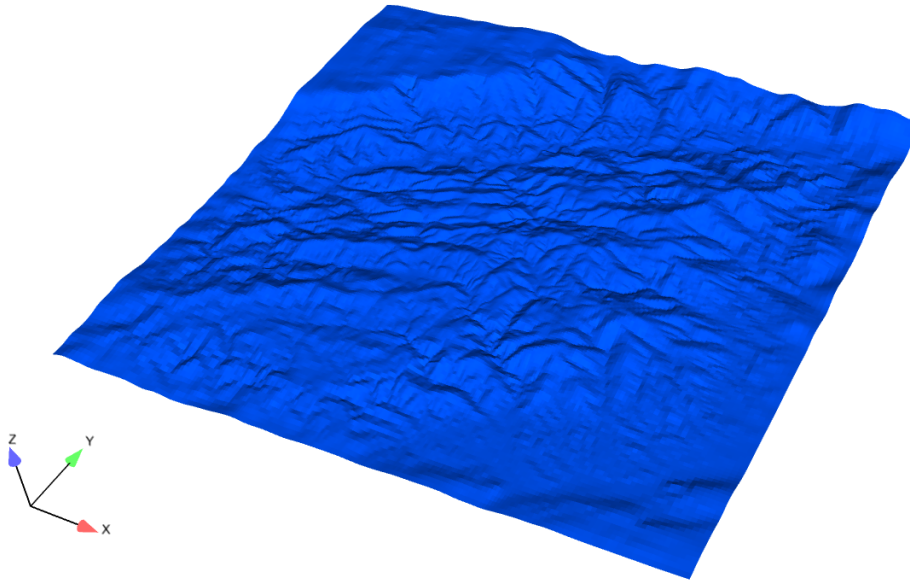


Figure 3.8: 3D view of the final topography of simulation domain.

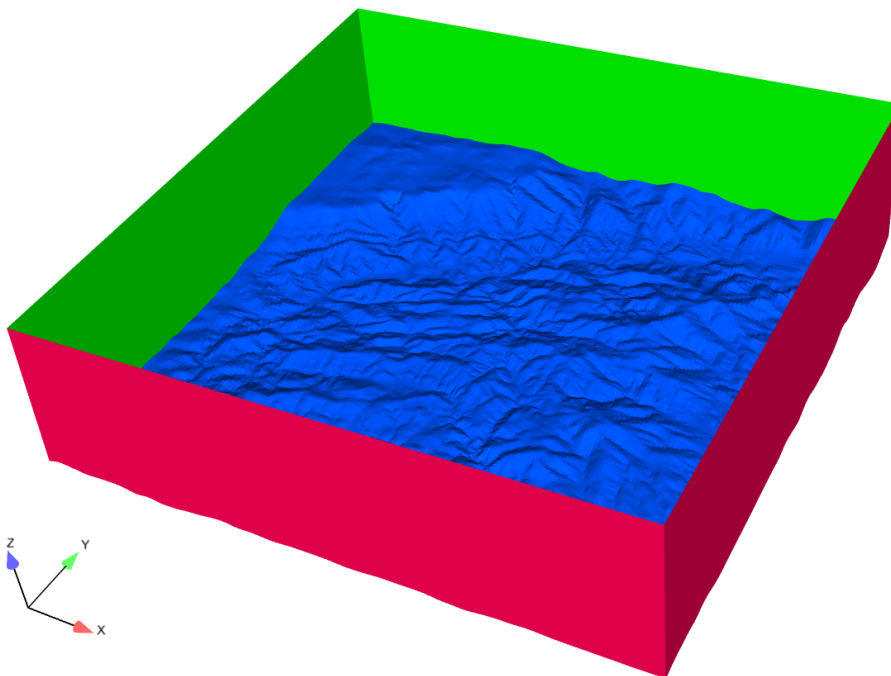


Figure 3.9: Computational domain

### 3.5.2. Mesh

The discretization of spatial domain is known as mesh or grid. Depending of the method used nodes are located at the center of the cells in the Finite Volume Method (FVM) or at the corner of the cells in the Finite Element Method (FEM). The quality of the mesh has direct influence on the quality of any CFD simulation results. Over 50% of the time spent in industry on a CFD project with complex geometry is devoted to the development of domain geometry and grid generation (Versteeg, 1995). When good quality mesh is used, the solver will be efficient and robust.

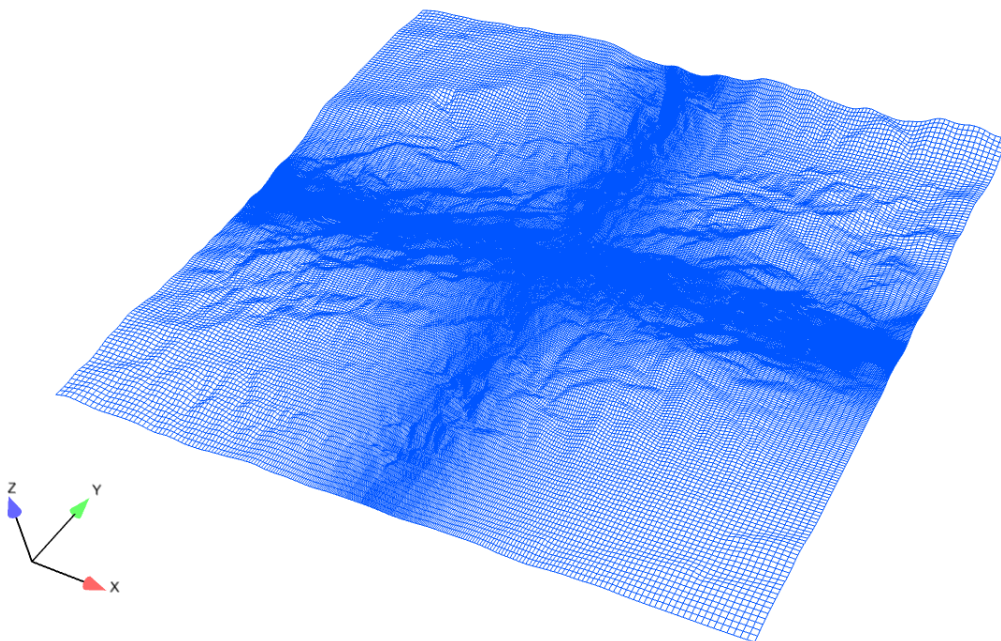


Figure 3.10: Surface mesh of the topography.

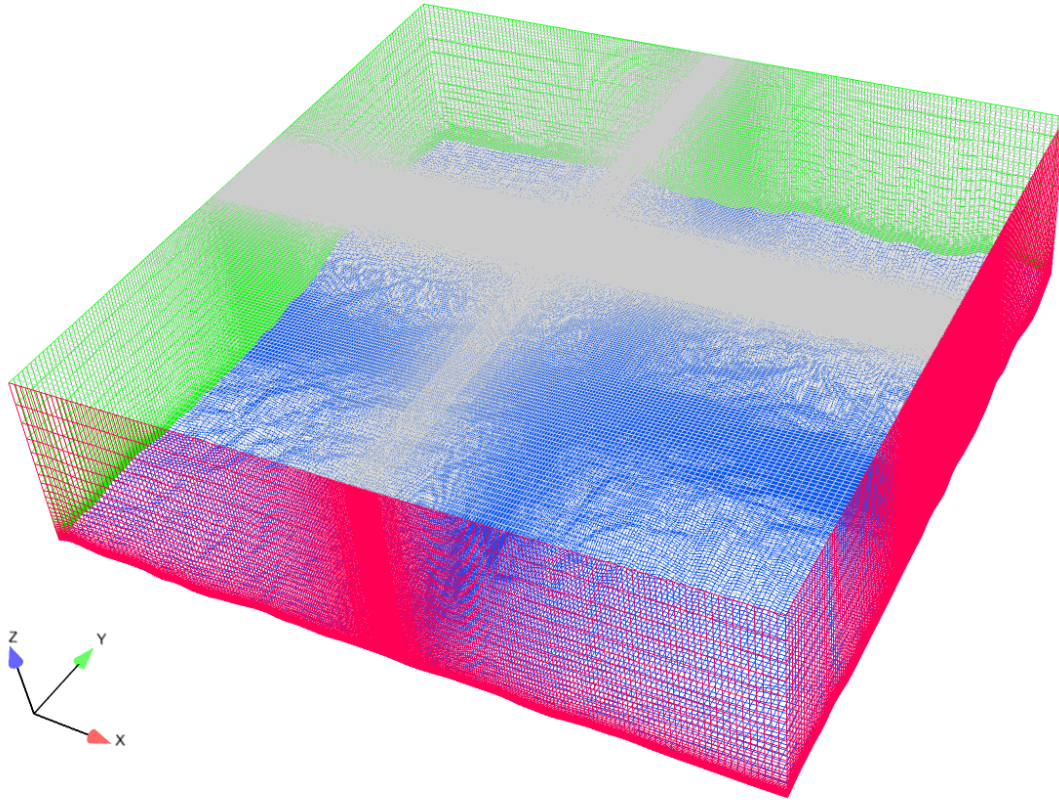


Figure 3.11: Surface grid of the computational domain.

Table 3.2: Grid specification for domain (20X20 Km<sup>2</sup>) used for the simulations

Grid	Z-resolution, m (in the first cell)	XY-resolution	Number of cells
Coarse	10	30 to 200 m	0.5 Million
Medium	5	20 to 150 m	1.2 Million
Fine	1.5	15 to 160 m	4.7 Million
Very fine	0.5	10 to 100 m	6.3 Million

Structured grid using hexahedral elements was created for the 20x20 km<sup>2</sup> topography with various grid resolutions in the X, Y and Z direction. Figure 3.10 shows the meshed topography. As the area of interest is located at the center of the domain, the cells are smaller at the center of the domain and larger at the boundaries. In the Z-direction, cells are smaller close to the topography in such

a way that the speed-up is captured correctly. The maximum cell skewness is 0.4 that is much less than allowable 0.8 for the hexahedral. Cells with highest aspect ratio were located at the top of the simulation domain. Figure 3.11 shows the surface grid of the complete computational domain. Table 3.2 shows the grids, *XY*-resolution and *Z*-resolution and number of cells. Grid independence was conducted with varying vertical resolution; results for different grids are discussed in the next chapter.

### 3.5.3. *Code\_Saturne* - Atmospheric Module

*Code\_Saturne* is an open source CFD software developed by Électricité de France. It is a general purpose CFD code, which handles complex geometry and physics (Archambeau et al., 2003). It solves the Navier-Stokes equations for 2D, 2D-axisymmetric and 3D flows, steady or unsteady, laminar or turbulent, incompressible or weakly dilatable, isothermal or not, with scalars transport if required. It is a finite-volume code, robust for application of several turbulence models from RANS to LES models. In addition, a number of specific physical models are also available as modules: gas, coal and heavy-fuel oil combustion, atmospheric flows, semi-transparent radiative transfer, particle-tracking with Lagrangian modeling, Joule effect, electric arcs, weakly compressible flows, rotor/stator interaction for hydraulic machines (<http://code-saturne.org/cms/>).

For RANS simulations in *Code\_Saturne*, the time scheme is an implicit first order Euler approach. A fractional step scheme is used to solve the mass and momentum equations. The first step (predictor step) provides predicted velocity components: they are determined sequentially and without coupling between each other (in the version 2.0 used for this work). The mass equation is taken into account during the second step (corrector step): a pressure Poisson equation is solved and the mass fluxes at the cell faces are updated. Furthermore, the equations for the turbulent variables (turbulent kinetic energy and dissipation or Reynolds stresses and dissipation) are solved, using also the

Euler approach. Next, the equations for the scalars are solved, also with the Euler approach.

#### **Atmospheric module:**

The atmospheric module of *Code\_Saturne* is developed by EDF R&D and CEREAs. The atmospheric module is based on the former code *Mercure\_Saturne* that was a peripheral version of *Code\_Saturne* adapted for multi-scales atmospheric airflow (either neutral or stratified) and pollutant dispersion studies. The atmospheric module takes into account the large-scale meteorological conditions and thermal stratification of the atmosphere. This module is used primarily for pollutant dispersion modeling, but other applications are currently developed like wind energy engineering and urban canopy modeling. Qu. (2011) investigated the energy exchange in an urban canopy flow using new atmospheric radiative and thermal schemes in *Code\_Saturne*. Recently, LES for atmospheric flow has been developed in *Code\_Saturne* and validated for the diurnal cycle of atmospheric boundary layer (Dallozzo, 2013).

Although RANS is less accurate in comparison with LES, RANS is the most commonly used CFD model for simulation involving turbulent flow in industrial and engineering application because it is computationally less expensive with fairly acceptable accuracy. The turbulence in the simulation domain is modeled by the standard  $k$ - $\epsilon$  turbulence closure as in the previous work concerning wind energy resource (Laporte, 2008). Here, the atmospheric stability is not taken into account in the simulations. The model can take into account the Coriolis force, but in the simulations carried out at local scale Coriolis force can be neglected.

#### **3.5.4. Turbulence model**

The equation of mass, momentum and energy conservation that are solved in atmospheric module of *Code\_Saturne* are:

$$\frac{\partial \rho \bar{u}_i}{\partial x_j} = 0 \quad (3.4)$$

$$\rho \left( \frac{\partial \bar{u}_i}{\partial t} + \bar{u}_j \frac{\partial \bar{u}_i}{\partial x_j} \right) = -\frac{\partial \bar{p}}{\partial x_i} + \frac{\partial}{\partial x_j} \left[ \mu \left( \frac{\partial \bar{u}_i}{\partial x_j} + \frac{\partial \bar{u}_j}{\partial x_i} \right) - \frac{2}{3} \mu \delta_{ij} \frac{\partial \bar{u}_k}{\partial x_k} \right] - \frac{\partial (\overline{\rho u'_i u'_j})}{\partial x_j} + (\rho - \rho_{ref}) g_i \quad (3.5)$$

$$\rho \left( \frac{\partial \bar{\theta}}{\partial t} + \bar{u}_j \frac{\partial \bar{\theta}}{\partial x_j} \right) = \frac{\partial}{\partial x_j} \left( \frac{\lambda}{C_p} \frac{\partial \bar{\theta}}{\partial x_j} \right) - \frac{\partial (\overline{\rho \theta' u'_j})}{\partial x_j} + S_{rad} \quad (3.6)$$

To close equation (3.4-3.6), the Reynolds stresses and the heat flux are expressed according to Boussinesq's turbulent diffusivity approximation:

$$\overline{u'_i u'_j} = \mu_t \left( \frac{\partial \bar{u}_i}{\partial x_j} + \frac{\partial \bar{u}_j}{\partial x_i} \right) - \frac{2}{3} \mu_t \delta_{ij} \frac{\partial \bar{u}_k}{\partial x_k} - \rho \frac{2}{3} \delta_{ij} k \quad (3.7)$$

$$-\overline{\rho \theta' u'_j} = \frac{\mu_t}{Pr_t} \left( \frac{\partial \bar{\theta}}{\partial x_j} \right) \quad (3.8)$$

where  $Pr_t$  the prandtl number.

In the  $k$ - $\epsilon$  model  $\mu_t$  is linked to the turbulent kinetic energy,  $k$  and the dissipation,  $\epsilon$  through:

$$\mu_t = C_\mu \rho \frac{\bar{K}^2}{\epsilon} \quad (3.9)$$

with  $C_\mu=0.09$  as in **Launder and Spalding (1974)**.

The transport equations for the turbulent kinetic energy and the dissipation are:

$$\rho \left( \frac{\partial \bar{K}}{\partial t} + \bar{u}_j \frac{\partial \bar{K}}{\partial x_j} \right) = \frac{\partial}{\partial x_j} \left[ \left( \mu + \frac{\mu_t}{\sigma_k} \right) \frac{\partial \bar{K}}{\partial x_j} \right] + \bar{P} + \bar{G} - \rho \varepsilon + S_k \quad (3.10)$$

$$\rho \left( \frac{\partial \varepsilon}{\partial t} + \bar{u}_j \frac{\partial \varepsilon}{\partial x_j} \right) = \frac{\partial}{\partial x_j} \left[ \left( \mu + \frac{\mu_t}{\sigma_k} \right) \frac{\partial \varepsilon}{\partial x_j} \right] + C_{\varepsilon 1} \frac{\varepsilon}{K} (\bar{P} + C_{\varepsilon 3} \bar{G}) - C_{\varepsilon 2} \rho \frac{\varepsilon^2}{K} + S_\varepsilon \quad (3.11)$$

$S_k$  and  $S_\varepsilon$  are source terms of the turbulent kinetic energy and dissipation respectively that can be used for example in drag porosity models.  $\bar{P}$  and  $\bar{G}$  are the production rate term of turbulent kinetic energy due to shear and production or destruction rate term of turbulent kinetic energy due to buoyancy respectively.

$$\bar{P} = -\overline{\rho u_j u_j} \frac{\partial \bar{u}_j}{\partial x_j} \quad (3.12)$$

$$\bar{G} = \frac{\mu_t}{Pr_t} \frac{1}{\theta} \frac{\partial \bar{\theta}}{\partial x_j} g_j \quad (3.13)$$

The parameters of the equations are:  $\sigma_k = 1$ ,  $\sigma_\varepsilon = 1.3$ ,  $C_{\varepsilon 1} = 1.44$ ,  $C_{\varepsilon 2} = 1.92$  and  $C_{\varepsilon 3} = 0$  for a stable stratified atmosphere and  $C_{\varepsilon 3} = 1$  for an unstable stratified atmosphere.

### 3.5.5. Coupling methods - Imposing mesoscale boundary condition on microscale CFD grid

As discussed earlier, the mesoscale model data are used as boundary condition for the microscale CFD model instead of logarithmic profile as in commercial microscale CFD modeling. Operational mesoscale data are obtained from Météo-France, with a horizontal grid resolution of almost 10 km and 31 vertical levels. The differences in horizontal grid ( $\Delta xy$ ) and vertical grid resolution ( $\Delta z$ ) between mesoscale grid ( $\Delta xy \approx$  a few km and  $\Delta z \approx$  some tens of meters) and

CFD grid ( $\Delta xy \approx$  some tens of m and  $\Delta z \approx$  some meters) are very large, whereas the topography variations are large at the border of the simulation domain. The reliefs seen by the mesoscale and microscale codes are different. In particular,

- When the relief altitude is smaller in the mesoscale grid than in microscale grid, higher velocities will be seen close to the ground in the microscale grid.
- When the relief altitude is higher in the mesoscale grid than in microscale grid, there are some unavailable values of the model variables.

Hence, imposing the inlet boundary condition on the CFD domain is a difficult task and different strategies need to be implemented. Different methods that were developed and used to impose mesoscale data on microscale grid are: translation, extrapolation and Cressman interpolation.

#### **3.5.5.1. Translation**

Translation method was developed and implemented in (Laporte, 2008). In this method, the mesoscale wind profiles are translated along the absolute coordinates of the microscale terrain. Therefore wind speed varies according to the height above ground level, which means that wind speed at a given height above the hill and valley have the same value (figure 3.12). This method is not reliable far from the ground in complex terrain. It also uses a single mesoscale profile to define the boundary condition on the entire inlet boundary, which is not a good boundary condition for complex terrain. Figure 3.12 shows the schematic diagram of translation method behavior on a complex terrain.

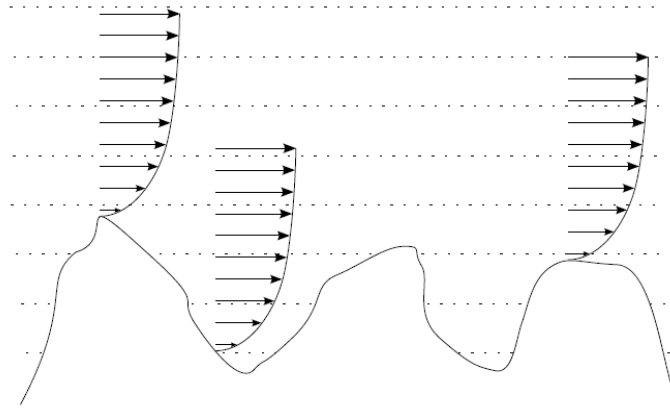


Figure 3.12: Translation coupling method on complex terrain.

### 3.5.5.2. Extrapolation

In extrapolation, the mesoscale wind profiles are extrapolated between the lowest level of the mesoscale profile and the absolute altitude of the local ground level in the microscale grid. Thus, above a certain level, the inlet wind speed obtained in extrapolation method is function of height above sea level. Extrapolation imposes low wind speeds in valley and at low altitude. Like translation, this method also uses a single mesoscale profile to define the boundary condition on the entire inlet boundary, which is not a good boundary condition for complex terrain. Figure 3.13 shows the schematic diagram of extrapolation method behavior on a complex terrain.

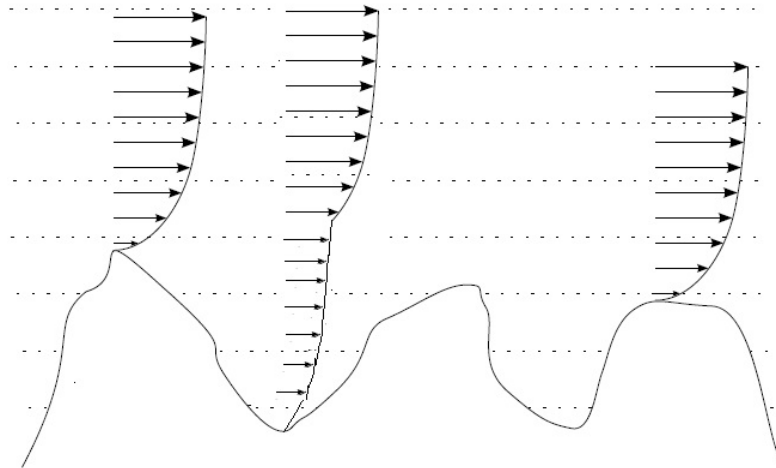


Figure 3.13: Extrapolation coupling method on complex terrain.

### 3.5.5.3. Cressman interpolation

**Cressman G.P. (1959)** introduced an interpolation method, which corrects the background grid point value by a linear combination of residuals between predicted and observed values. The residuals are weighted depending only on the distance between the grid point and observation. This method is widely used in NWP for weather forecasting (**Kalnay, 2008**). Using the Cressman interpolation, the wind speed on a boundary face of the microscale grid can also be calculated as a linear combination of the values provided by the nearby mesoscale data. This method is simple and very fast and results are more realistic.

Figure 3.14 shows schematic example of Cressman interpolation method. The grid point, P is located close to the observation points  $O_1$ ,  $O_2$  and  $O_3$ . The value of the grid point P is calculated using the defined radius of influence. The observations  $O_1$  and  $O_2$  influence the grid point P and  $O_3$  doesn't. Cressman interpolation takes into account multiple mesoscale grid points for calculating and imposing the inlet boundary condition on the microscale CFD grid and this

method is also used for field measurement data assimilation in to the CFD model. Cressman interpolation can be applied to all types of terrain.

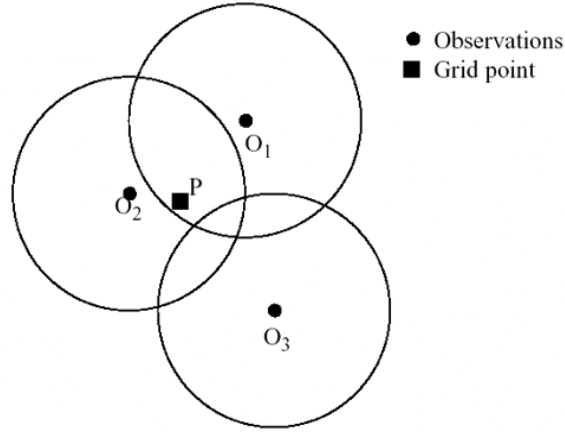


Figure 3.14: Cressman interpolation

These values are weighted depending only upon the distance between the CFD grid point and the mesoscale grid points. Thus, the inlet horizontal wind components are calculated as combinations of mesoscale data following:

$$V_{interpolate} = \frac{\sum_{i=1}^{n_{aladin}} V_i W_i}{\sum_{i=1}^{n_{aladin}} W_i} \quad (3.14)$$

$$W_i = \left\{ \begin{array}{ll} 0 & \text{if } \frac{r_i^2}{2} \geq 700 \\ e^{-\frac{r_i^2}{4}} & \text{else} \end{array} \right\} \quad (3.15)$$

$$r_i^2 = \left( \frac{x_{value} - x_i}{r_L} \right)^2 + \left( \frac{y_{value} - y_i}{r_L} \right)^2 + \left( \frac{z_{value} - z_i}{r_Z} \right)^2 \quad (3.16)$$

Where  $V_{interpolate}$  is the Cressman interpolated velocity component,  $n_{aladin}$  is the number of available ALADIN verticals,  $V_i$  is the ALADIN velocity component for

the vertical  $i$ , the weights  $W_i$  are functions of the distance between the CFD grid point where the wind speed is calculated (coordinates  $x_{value}$ ,  $y_{value}$ , and  $z_{value}$ ) and the nearby ALADIN grid points (coordinates  $x_i$ ,  $y_i$ , and  $z_i$ ). And  $r_i$  is the total radius of influence,  $r_L$  and  $r_Z$  are longitudinal and vertical radius of influence initialized at the beginning of the computation. The optimum radii are determined empirically. Thus, Cressman interpolation is able to calculate the mesoscale model variables on the microscale grid. Sensitivity analysis for the Cressman radius of influence is discussed in the next chapter, section 4.3.

### 3.5.6. Data assimilation – nudging

Data assimilation is a concept encompassing method for combining observations of variables into numerical models as used to predict weather. Data assimilation can proceed by analysis cycles, in each analysis cycle observations of the current state of a system are combined with the results from a NWP model to produce an analysis, which is considered as 'the best' estimate of the current state of the system. NWP is able to estimate the atmospheric evolution; given an estimate of the initial condition of the atmosphere, appropriate surface and lateral boundary conditions and proper physical model. Accuracy of the atmospheric evolution depends on the quality of the estimation of the initial condition. At present the operational NWP use data assimilation, which produces the initial conditions through a statistical combination of observations and short-range forecasts (Kalnay, 2007).

In NWP, there are 2 types of data assimilation: 3 Dimensional Data Assimilation (3DDA) and 4 Dimensional Data Assimilation (4DDA). In 3DDA only the observations available at the time of analysis are used and in 4DDA the assimilation is performed following a continuous process in time. Nudging is a 4DDA method. It is a Newtonian relaxation data assimilation technique used to incorporate the measurement data into the CFD simulations. It consists in adding to the prognostic equation of the wind components (or other variable of the model) a term that nudges the solution towards the observations (Kalnay,

2008 and Warner, 2011). This term has a negative sign that "keeps" the calculated state locally close to the observations. For example, a primitive equation model, the velocity equation is written as and similarly for all other equations.

$$\rho \left( \frac{\partial \bar{u}_i}{\partial t} + \bar{u}_j \frac{\partial \bar{u}_i}{\partial x_j} \right) = -\frac{\partial \bar{p}}{\partial x_i} + \frac{\partial}{\partial x_j} \left[ \mu \left( \frac{\partial \bar{u}_i}{\partial x_j} + \frac{\partial \bar{u}_j}{\partial x_i} \right) - \frac{2}{3} \mu \delta_{ij} \frac{\partial \bar{u}_k}{\partial x_k} \right] - \frac{\partial (\overline{\rho u'_i u'_j})}{\partial x_j} + (\rho - \rho_{ref}) g_i + \left( \frac{\overline{u_{obs}} - \overline{u_s}}{\tau_u} \right) * W(x, y, z, t) \quad (3.17)$$

Where  $\overline{u_{obs}}$ ,  $\overline{u_s}$ ,  $\tau_u$  and  $W(x, y, z, t)$  are observed velocity, simulated velocity in the previous time step, relaxation time scale or nudging coefficient and Cressman type spatial and temporal weighting function respectively. This type of modeling approach is not common in CFD simulation and *Code\_Saturne* is modified to incorporate this additional forcing term in the Navier-stokes equation.

The nudging coefficient  $\tau_u$  is chosen based on empirical consideration and may depend on the variables. It is carefully tuned to appropriate value like in the data assimilation application in NWP (Stauffer et al., 1993). Then Cressman type volumetric interpolation is used in the horizontal and vertical direction in order to calculate the observed values on the surrounding grid points. Sensitivity analysis was carried out to determine the volume of the assimilation zone, where the observations are interpolated. Horizontal radius of influence ( $r_L$ ) and vertical radius of influence ( $r_Z$ ) determine the volume of the assimilation zone.

The drop-off function used for Cressman spreading function is similar to the one used in (Haupt, 2011). A radial drop-off rate of  $e^{-r/2}$  is used for  $W(x, y, z, t)$ , where  $r_i$  is the radial distance from observation point. A study was conducted to

see the influence of  $r_L$  and  $r_z$  (longitudinal and vertical radius of influence) on  $W(x, y, z, t)$ . This type of function is used in NWP and it doesn't vary in time since time integration is very small in CFD simulation. Here, the value of  $r_L$  and  $r_z$  is set in such way that  $W(x, y, z, t)$  includes the other observational mast locations into the assimilation zone.

## 4. Results: Sensitivity and parameteric analysis

### 4.1. Case description

The case chosen for the initial analysis is typical of the most dominant wind direction (Northwesterly) and is on 07<sup>th</sup> December 2007 and the time for the CFD simulation is 16:00 UTC. The surface wind speed and temperature are 6 m/s and 10 °C respectively at 100 m. The wind direction along the height is not uniform and varies between NWW and NW sector. Figure 4.1 depicts the 10 ALADIN wind profiles decomposed into  $u$  and  $v$  components located in and around the simulation domain (see figure 3.5). Grid independence, sensitivity analysis of radius of influence in Cressman interpolation, analysis of different coupling methods and data assimilation sensitivity analysis are carried out with this case. On-site field measurements at M80 (cup anemometer, sonic anemometer and sodar), M (cup anemometer and sodar) and FP (cup anemometer) are available for assimilation and validation.

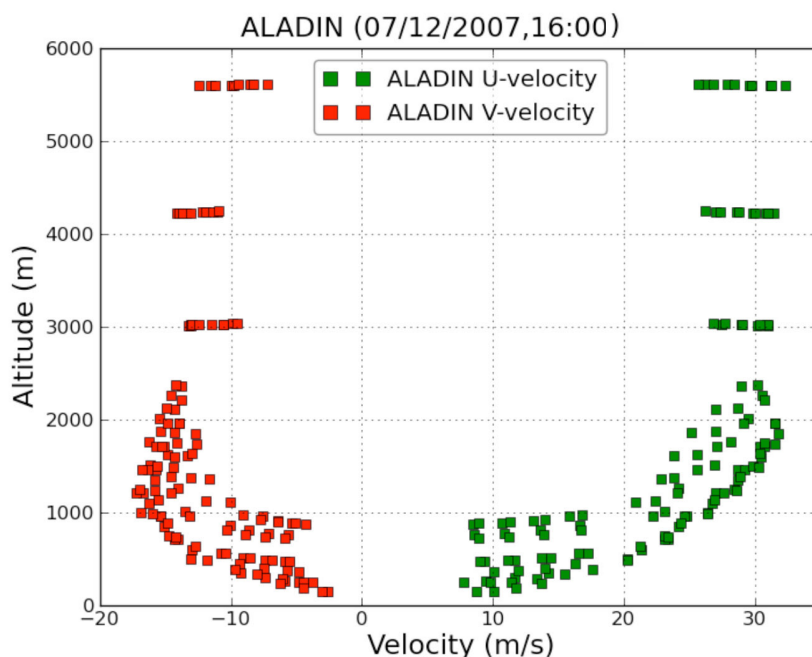


Figure 4.1: ALADIN inlet wind profiles decomposed into  $u$  and  $v$  components.

## 4.2. Grid Independence

Grid independence studies in CFD are conducted to make sure that the results obtained are due to the boundary conditions and physics used, not to the mesh resolution. Hence if the results do not change with the mesh density, then the grid independence is achieved. But the main issue is that this varies from case to case, depending on the physics involved and flow structures. Not checking is a common cause of erroneous results in CFD.

Grid independence study is conducted for a simulation domain whose dimensions are 20x20 km<sup>2</sup> horizontally and 5.7 km vertically. Table 3.2 gives details of the different grid vertical, horizontal resolutions and number of hexahedral cells. A total of 4 grids were constructed with different horizontal and vertical resolutions. The coarse, medium, fine and very fine grids have a first cell height of 10 m, 5 m, 1.5 m and 0.5 m respectively and contain 0.5, 1.2, 2 and 4.7 million hexahedral elements respectively. The horizontal grid resolution varies from 10 m at the center of the domain to 100 m at the domain boundaries in the fine grid, and from 30 m to 200 m in the coarse grid.

The simulations are carried out with same set-up for the 4 different grids such as, standard  $k$ - $\epsilon$  turbulence model, boundary condition – most dominant wind direction (Northwesterly), without data assimilation and stability effects. After the convergence is achieved, the results show considerable differences in prediction between the 4 grids.

To show the influence of the grid resolution on the flow field, velocity cross-sections along the X-axis are created for each grid. This cross-section is located exactly at the center of the computational domain where the mesh is very dense. Figure 4.2a and 4.2b show the wake formation behind the hill for coarse and very fine grid respectively. Wake is noticeable at this location for all 4 grids but with varying resolution and size. Wake behind the hill causes reverse flow,

which can be seen clearly in the fine grid (figure 4.2b). The coarse grid is unable to predict any such reverse flow in this region. It is to be noted that this wake sits directly in front of the M80 mast and hence it is necessary to capture properly the wind flow field in this region. The coarse and medium grids are clearly unable to predict the wake characteristics. Fine and very fine grids with adequate grid resolution are able to capture wake characteristics and its influence on surroundings.

Figure 4.3a, 4.3b and 4.3c compare the computed velocity magnitude profile for 3-mast location at M80, M and FP for four grids. The M80 and FP masts were located on the top of steep slopes and wind speed-up is expected at this location. Figure 4.3a and 4.3c show that coarse and medium grids are unable to capture the wind speed-up at both M80 and FP location. While fine and very fine grid, predicted better the velocity magnitude profile which indicate convergence. This indicates that fine and very fine grid resolution have predicted very similar flow fields. The M mast is located south of M80 mast on the top of the ridge running from north to south. Figure 4.3b show that the computed velocity profiles for all grids converge for M mast.

Overall, the grid independence study shows that coarse and medium grids over predict the velocity close to the ground and thus are unable to predict correctly the wind speed-up induced by the topography on the hills. Grids with vertical resolution below 2 m near the ground are able to predict the wind flow fields and speed-up better at the mast location M80 and FP. The difference in predicted velocity between fine and very fine grid is negligible. Hence, fine grid spacing is adequate to predict the wind accurately and saves additional computational time in comparison with very fine grid.

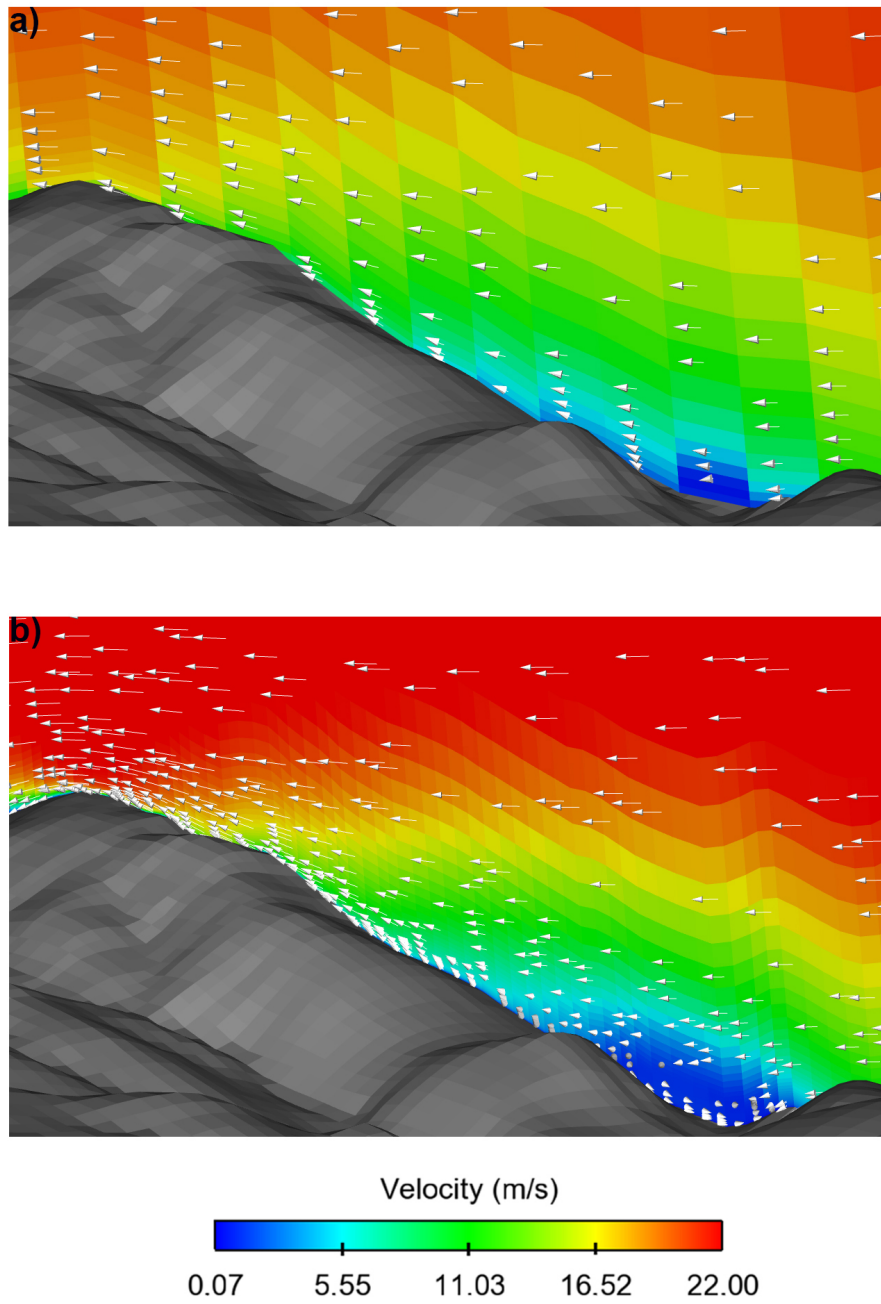


Figure 4.2: Wake formation behind the hill for (a) coarse grid (b) fine grid

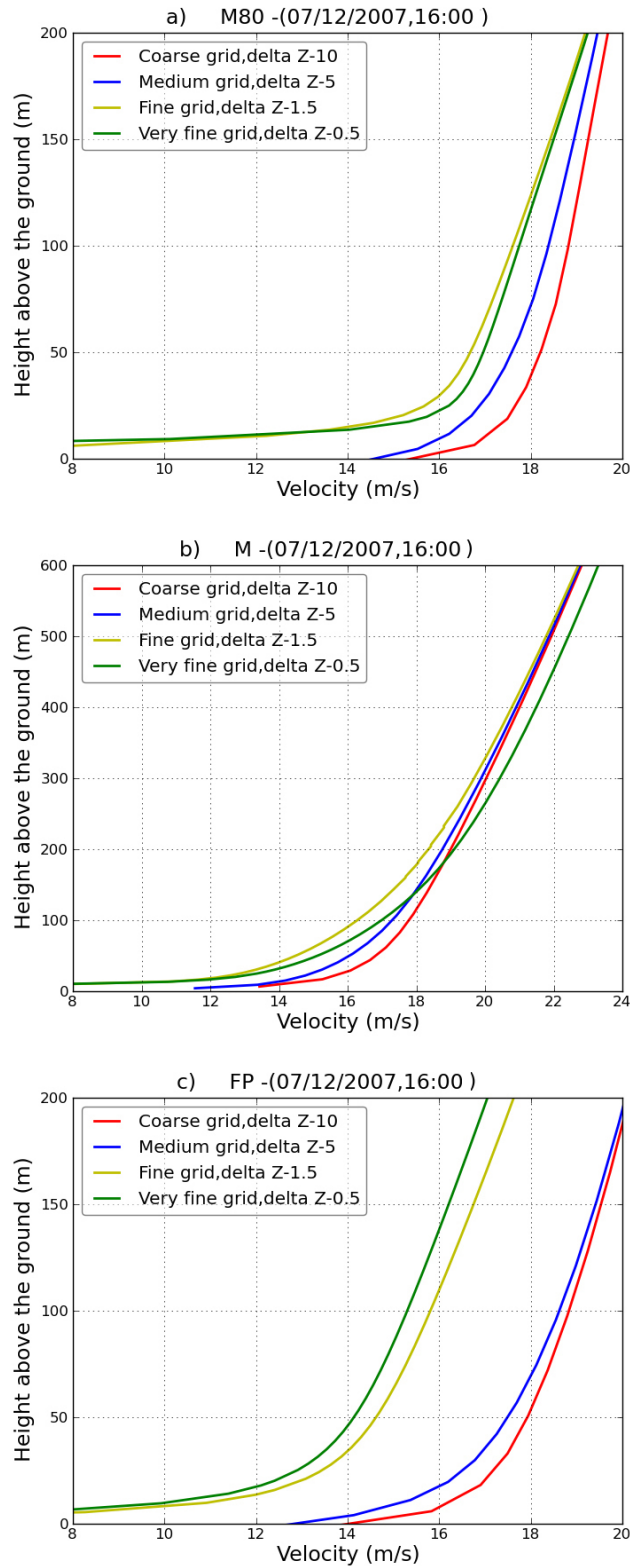


Figure 4.3: Grid independence: comparison of velocity profile of different CFD grids (Coarse, Medium, Fine, Very fine) prediction at location a) M80, b) M and c) FP masts.

### 4.3. Cressman Sensitivity - Radius of influence

As discussed earlier, to impose the mesoscale wind profile on microscale CFD grid 3 methods were developed: translation, extrapolation and Cressman interpolation. Translation and extrapolation can only use a single ALADIN grid profile to impose the inlet boundary condition for all inlet boundary faces. The ALADIN grid profile can be chosen from either the upstream or middle of the computational domain depending on the prevailing wind direction. The drawback of translation and extrapolation method is the difference in the relative altitude of the chosen ALADIN grid profile and the inlet boundary face altitude that varies locally.

Cressman interpolation is used in data assimilation and also to impose the inlet boundary condition. It uses multiple ALADIN grid profiles to calculate the inlet boundary faces values. The radius of influence in Cressman interpolation determines the amount of weight of each ALADIN grid points on the CFD grid point. Longitudinal radius of influence ( $r_L$ ) and vertical radius of influence ( $r_z$ ) contributes to total radius of influence. These two parameters determine the radius of influence of each ALADIN grid point on the inlet boundary face. Sensitivity analysis is carried out to determine the optimum values of longitudinal and vertical radius of influence.

Sensitivity analysis was carried out with values of 2000, 4250, 8500 and 10500 m for the longitudinal radius and 100, 200 and 500 m for the vertical radius. Figure 4.4(a-e) show all the ALADIN grid points  $u$  velocity component (green square),  $v$  velocity component (red square) and Cressman interpolated  $u$  velocity component and  $v$  velocity component (black) for all CFD inlet boundary faces using longitudinal radius of influence of 2000, 4250, 8500 and 10500 m and vertical radius of influence of 100 m and 200 m.

Longitudinal radius of influence ( $r_L$ ) of 2000 and 4250 m with vertical radius of influence ( $r_z$ ) of 100 m showed large scattered region of Cressman interpolated  $u$  and  $v$  velocity component (Figure 4.4a and 4.4b). This radius of influence gives maximum weight to the ALADIN grid point close to the considered inlet face of the CFD domain. For longitudinal radius ( $r_L$ ) of 8500 m, the scattered region of Cressman interpolated velocity is smaller compared to 2000 and 4250 m (Figure 4.4c). The west face of the computational domain is located in between two columns of ALADIN grid points and Cressman interpolation with  $r_L$  of 8500 m gives equal weight to both columns of the ALADIN grid points.

Longitudinal radius ( $r_L$ ) of 10500 m and beyond 10500 m shows no difference in the imposed inlet velocity at the boundaries. The radius is high enough; all the ALADIN grid points are used with varying weights. Figure 4.4d shows that the scatter of Cressman interpolated  $u$  and  $v$  velocity components is smaller than with longitudinal radius of 2000, 4250 and 8500 m.

The main objective of the CFD simulations is to compare CFD results with field measurements close to the ground. ALADIN profiles from the ground to 1000 m have 8 grid points at levels 10, 20, 50, 100, 250, 500, 750, 1000 m. Choosing very small vertical radius of influence will affect the top layer of the interpolated inlet boundary and large radius will affect the bottom layer. Vertical radius ( $r_z$ ) of 200 m (figure 4.4e) and beyond 200 m impose higher velocities as it mixes lower altitude velocities (close to the ground) and higher altitude velocities. The results are satisfactory for the vertical radius of influence of 100 m. Longitudinal radius ( $r_L$ ) of 8500 m and vertical radius ( $r_z$ ) of 100 m are chosen for further simulations. Cressman sensitivity tests have to be conducted for every site in case the domain and mesoscale grid are changed.

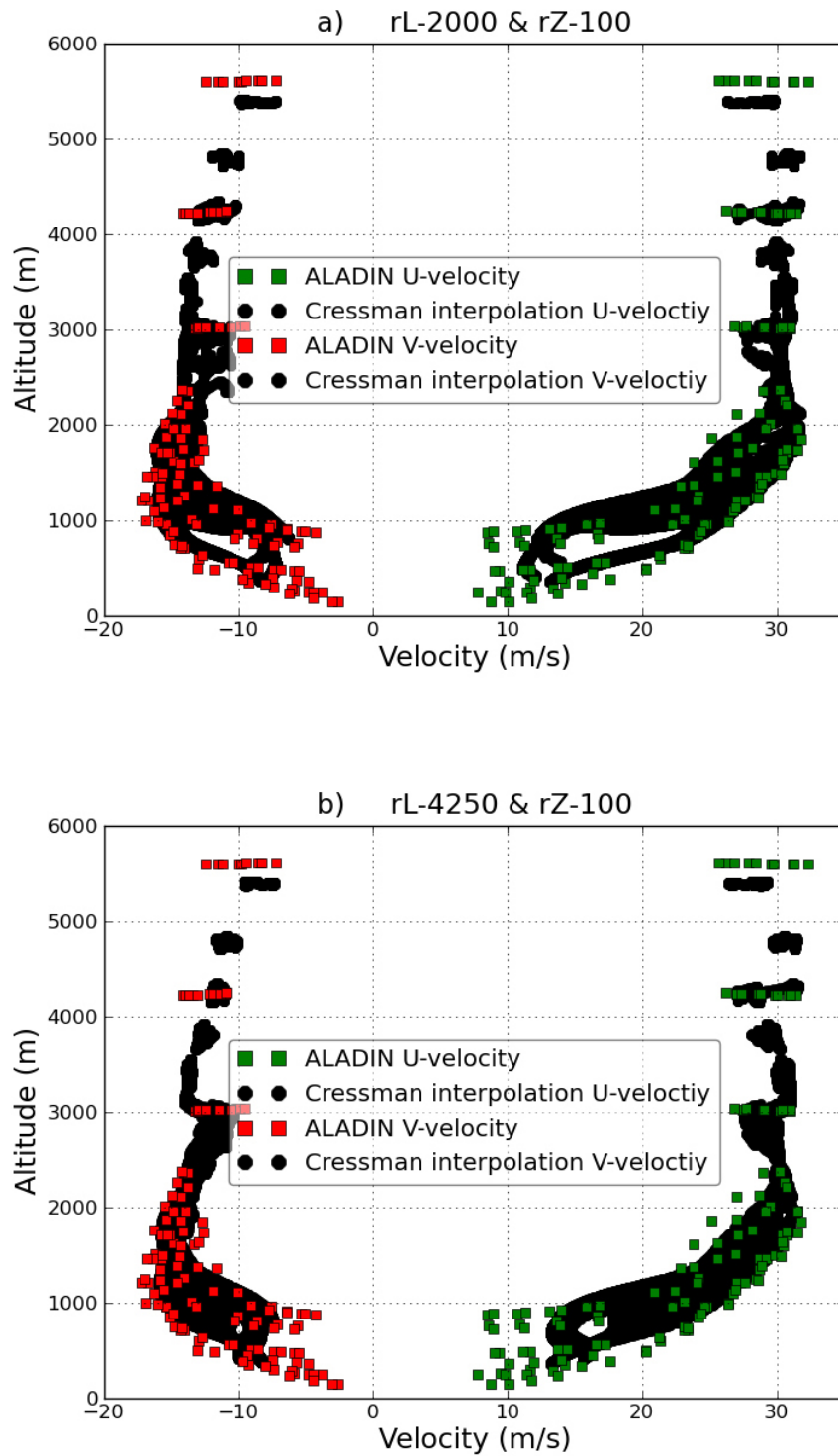


Figure 4.4: Imposed inflow along the north and west boundary using Cressman interpolation for a)  $r_L=2000$  m and  $r_Z=100$  m b)  $r_L=4250$  m and  $r_Z=100$  m.

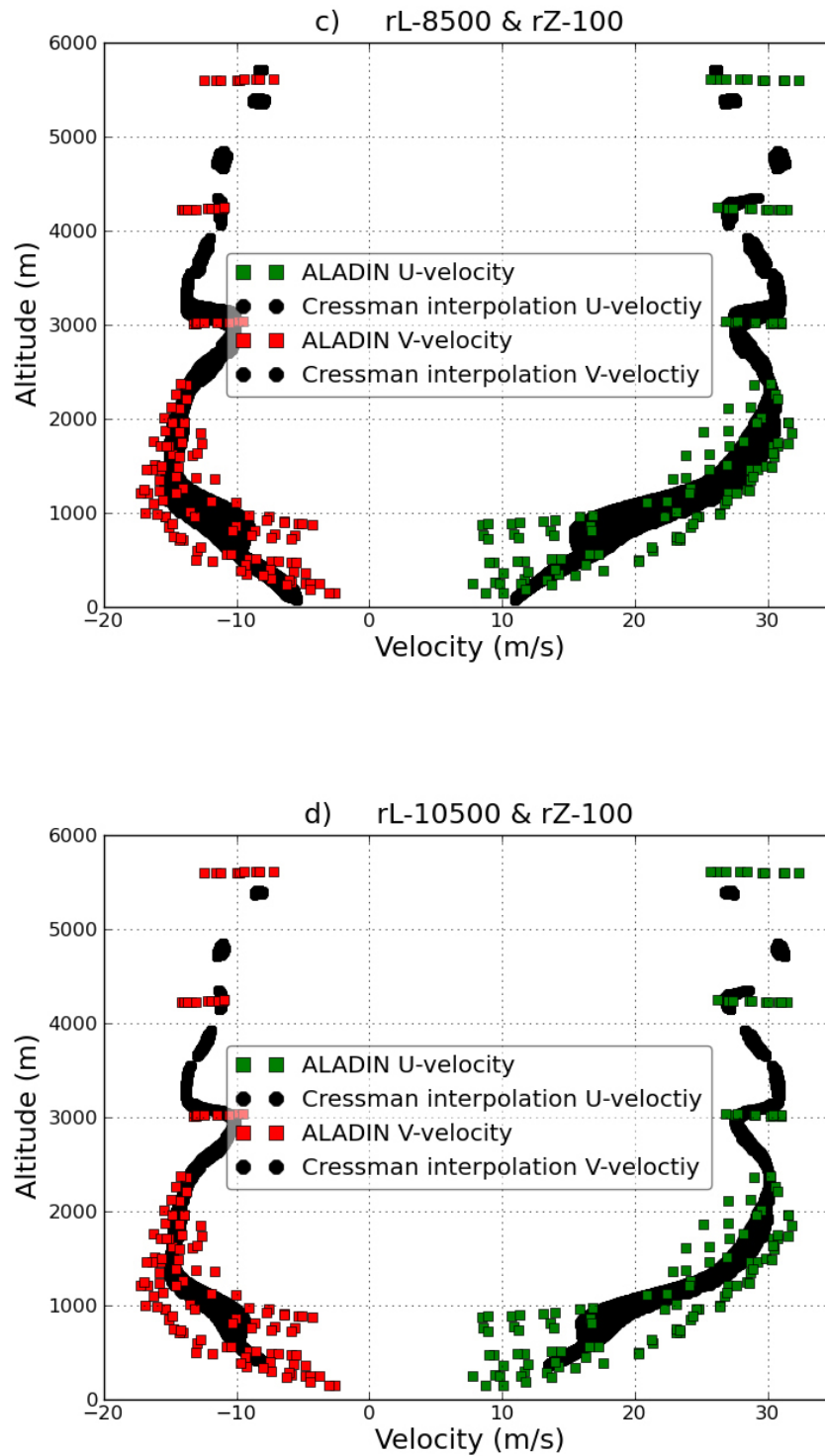


Figure 4.4: Imposed inflow along the north and west boundary using Cressman interpolation for c)  $r_L=8500$  m and  $r_Z=100$  m d)  $r_L=10500$  m and  $r_Z=100$  m.

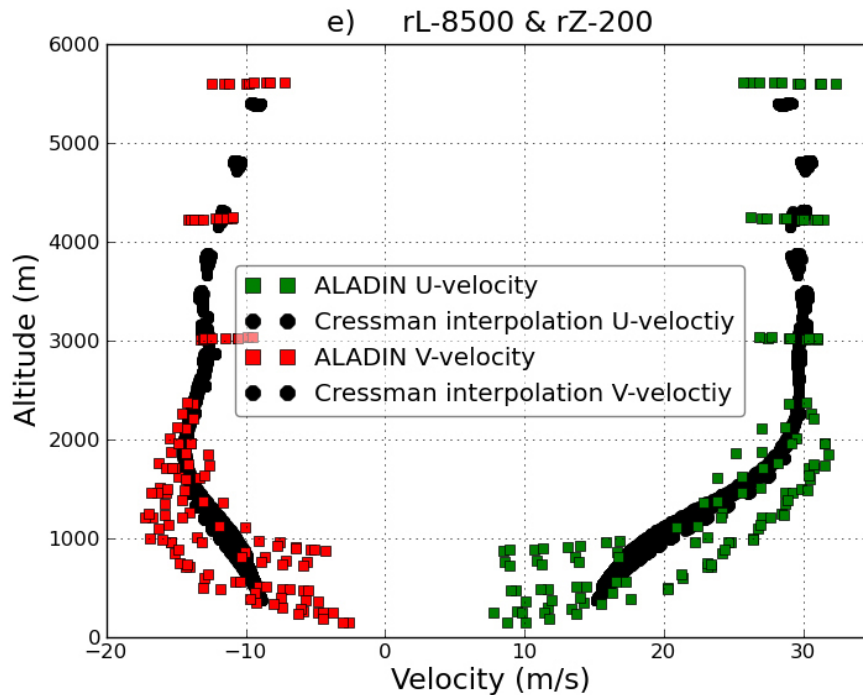


Figure 4.4: Imposed inflow along the north and west boundary using Cressman interpolation for e)  $r_L=8500$  m and  $r_Z=200$  m

#### 4.4. Coupling method - Translation, Extrapolation, Cressman interpolation

Simulations are carried out to see the influence of coupling methods (Translation, Extrapolation and Cressman interpolation) at measurement mast locations. Fine grid is used for all the simulation, Cressman interpolation uses longitudinal radius of influence ( $r_L$ ) of 8500 m and vertical radius of influence ( $r_Z$ ) of 100 m and translation and extrapolation coupling method use the ALADIN grid profile closest to the measurement masts.

North and west are inlet boundary faces and south and east are outflow boundary faces. Figure 4.5a, 4.5b and 4.5c show the cross-section of the imposed velocity magnitude at the north face using translation, extrapolation and Cressman interpolation respectively. In translation method, (figure 4.5a) the imposed wind speed varies uniformly along the height above the ground for the

entire north face. It is also noticed that higher altitude and lower altitude have wind speed magnitude of same order. While using extrapolation (figure 4.5b) low wind speed is observed at low altitude and high velocity at high altitude. Figure 4.5c shows the computed velocity magnitude of Cressman interpolation.

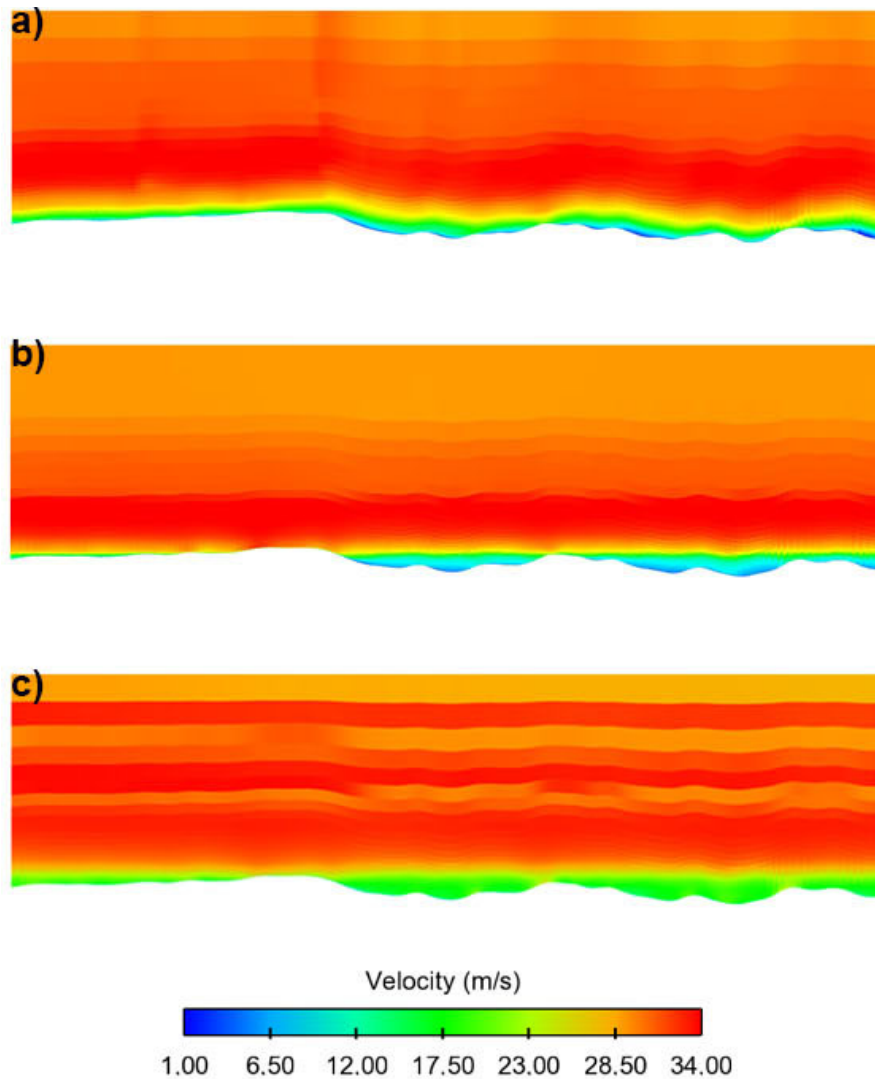


Figure 4.5: Imposed mean velocity cross-section at North boundary using a) translation b) extrapolation and c) Cressman interpolation method.

Figure 4.6a, 4.6b and 4.6c show the comparison between the onsite field measurements and *Code\_Saturne* prediction using translation, extrapolation and Cressman interpolation at M80, M and FP locations respectively. At M80

location, three consecutive 10 minutes average velocity of cup and sonic anemometer measurement and three consecutive 20 minutes average velocity of short-range sodar measurements are plotted. At M mast location, three consecutive 10 minutes average velocity of cup anemometer and three consecutive 20 minutes average velocity of long-range sodar measurements are plotted. At FP mast, three consecutive 10 minutes average velocity of cup anemometer are plotted. It is to be noted that the hourly ALADIN wind profiles are imposed at the inlet and the computed *Code\_Saturne* results are compared with 10 and 20 minutes field measurement average.

At M80 mast location, the three consecutive 10 minutes average of cup and sonic anemometer are in good agreement with each other. The sodar measured reduced average velocity in comparison to the cup and sonic anemometer and shows mixed wind profile along the 100 m height. CFD prediction using *Code\_Saturne* showed that Cressman interpolation and extrapolation coupling methods clearly better predict the mean wind speed, compared to translation coupling method. All the three coupling methods are able to capture the shape of wind speed-up. At M mast location, the wind speed is over-predicted by *Code\_Saturne* compared to both cup anemometer and sodar measurements for all three coupling methods. At FP location, the three consecutive 10 minutes averages of cup anemometer show large variation. The CFD models cannot reproduce this variability, as the results of the simulation correspond to a stationary state for the given boundary condition.

The results of CFD simulations using translation, extrapolation and Cressman interpolation (as inlet boundary) were compared and they show Cressman interpolation performed better compared to translation and extrapolation. Translation and extrapolation use a single mesoscale profile as inlet boundary and results vary depending on the chosen mesoscale grid point. Overall, using Cressman interpolation method to compute the inflow at lateral boundary seems to be a better option to take into account both the horizontal gradients in the mesoscale field and the influence of topography.

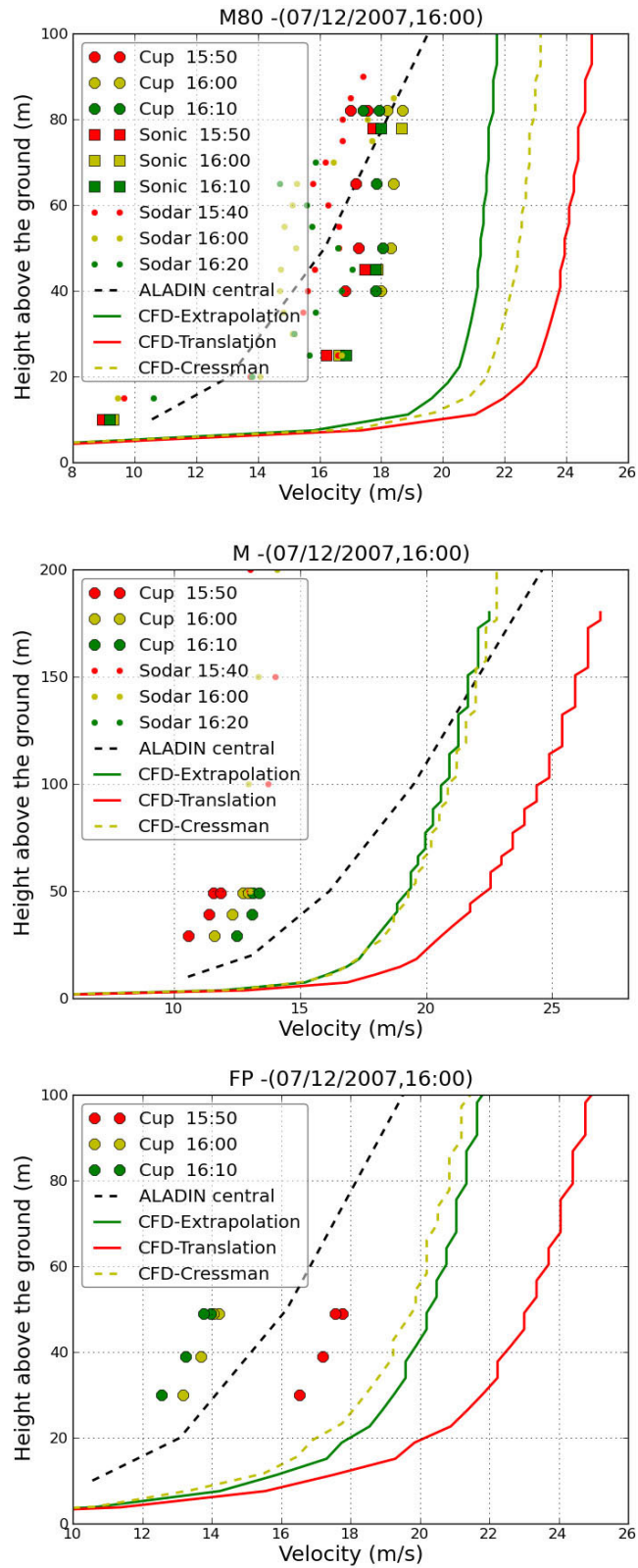


Figure 4.6: Comparison of velocity profiles at 3-mast location M80, M and FP using different coupling methods.

#### 4.5. Data assimilation at M80 mast location

Nudging, the data assimilation technique described in the previous chapter is implemented into *Code\_Saturne*. The preliminary analysis of implementation and testing of assimilation procedure is carried out for the same case that occurred on 07<sup>th</sup> December 2007 at 16:00 UTC. Cressman interpolation is used for imposing the inlet boundary condition for CFD simulation with data assimilation. Three masts (M80, M and FP) with very good data sets are available for data assimilation procedure. The idea is to assimilate one of the mast and use the other two masts are used for validation purpose. The location of M80 mast in between M and FP masts is an ideal choice for field measurement assimilation. The M80 mast location has three measurement data sets (cup and sonic anemometer and sodar) and hence cross validation between the assimilated data and rest of data is possible at this location. For the initial analysis the sonic anemometer measurements are assimilated into the CFD simulation.

The observed velocities  $\bar{u}_{obs}$ , in Eq. (3.17) have to be interpolated in the vicinity of M80 mast location. The volumetric Cressman interpolation is used to interpolate  $u$  and  $v$  components of the observed velocity. Sensitivity analysis is carried out to determine the longitudinal radius of influence ( $r_L$ ) and vertical radius of influence ( $r_Z$ ) of the volumetric Cressman interpolation. Sonic anemometer measurements are available at 10, 25, 45 and 78 m heights. The volumetric Cressman interpolation is carried out with longitudinal radius ( $r_L$ ) of 400, 600 and 800 m and vertical radius ( $r_Z$ ) of 100, 150 and 200 m. Figure 4.7a, 4.7b and 4.7c show the isosurface of the interpolated observed velocity inside the simulation domain and vertical cross-section of interpolated  $u$  and  $v$  observed velocity component using  $r_L$  of 600 m and  $r_Z$  of 150 m. The larger the value of radius of influence ( $r_L$  and  $r_Z$ ), the larger the volume of Cressman interpolation. Figure 4.8a and 4.8b show the 4 levels of sonic anemometer measurement data along with the vertical profiles of interpolated  $u$  and  $v$  velocity components at M80 location respectively.

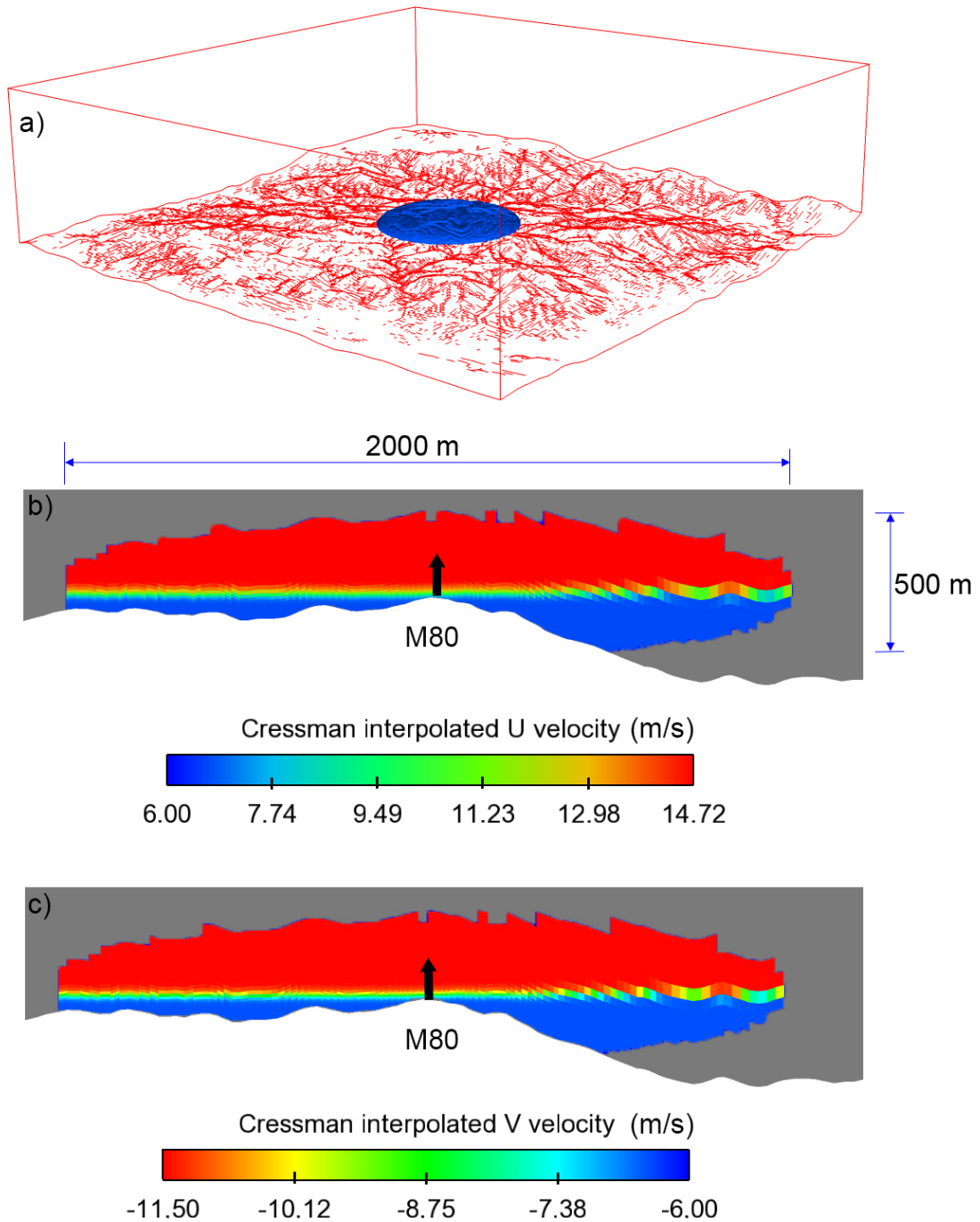


Figure 4.7: Volumetric Cressman interpolation at mast M80 location: a) Isosurface of the Cressman interpolated velocity, b) Cross-section of observed volumetric Cressman interpolated  $u$  velocity and c) Cross-section of observed volumetric Cressman interpolated  $v$  velocity.

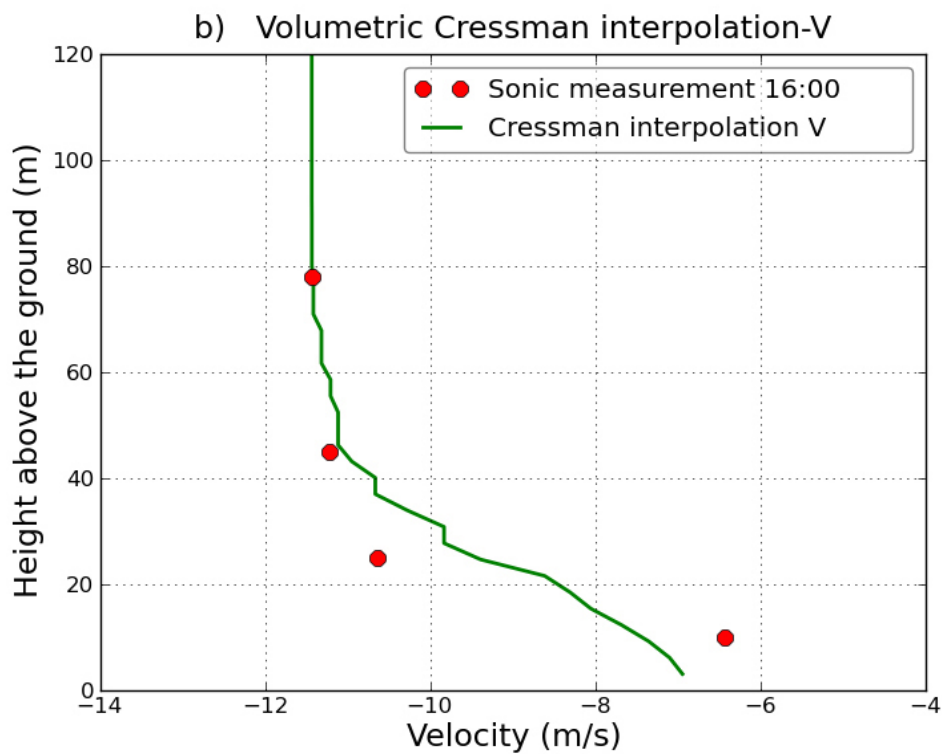
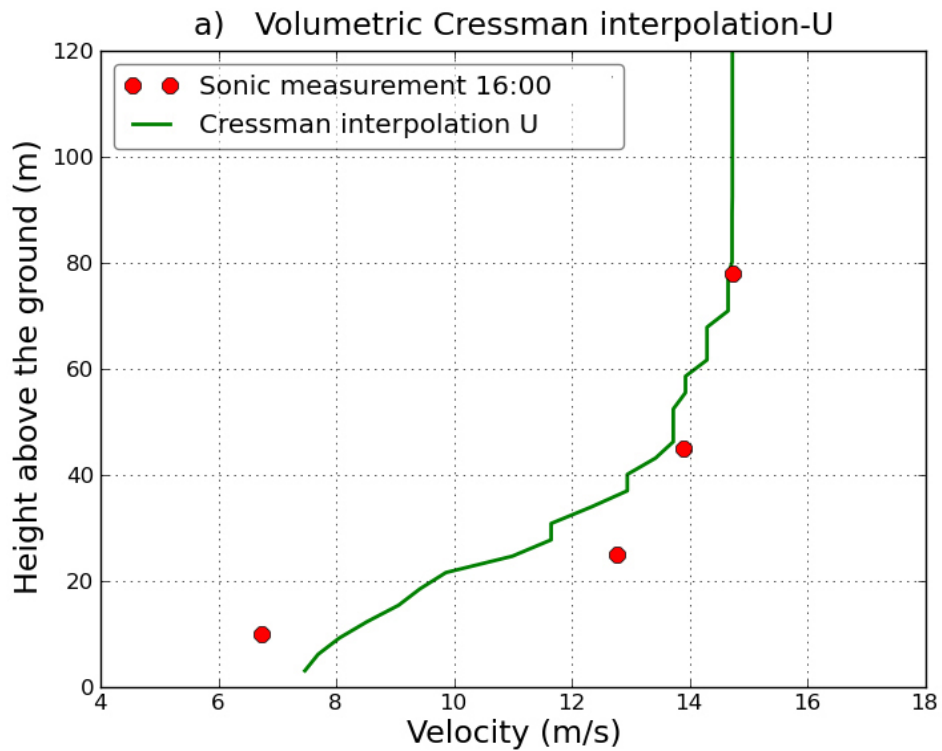


Figure 4.8: Volumetric Cressman interpolation at M80 mast location using sonic anemometer measurement: a)  $u$  velocity component and b)  $v$  velocity component.

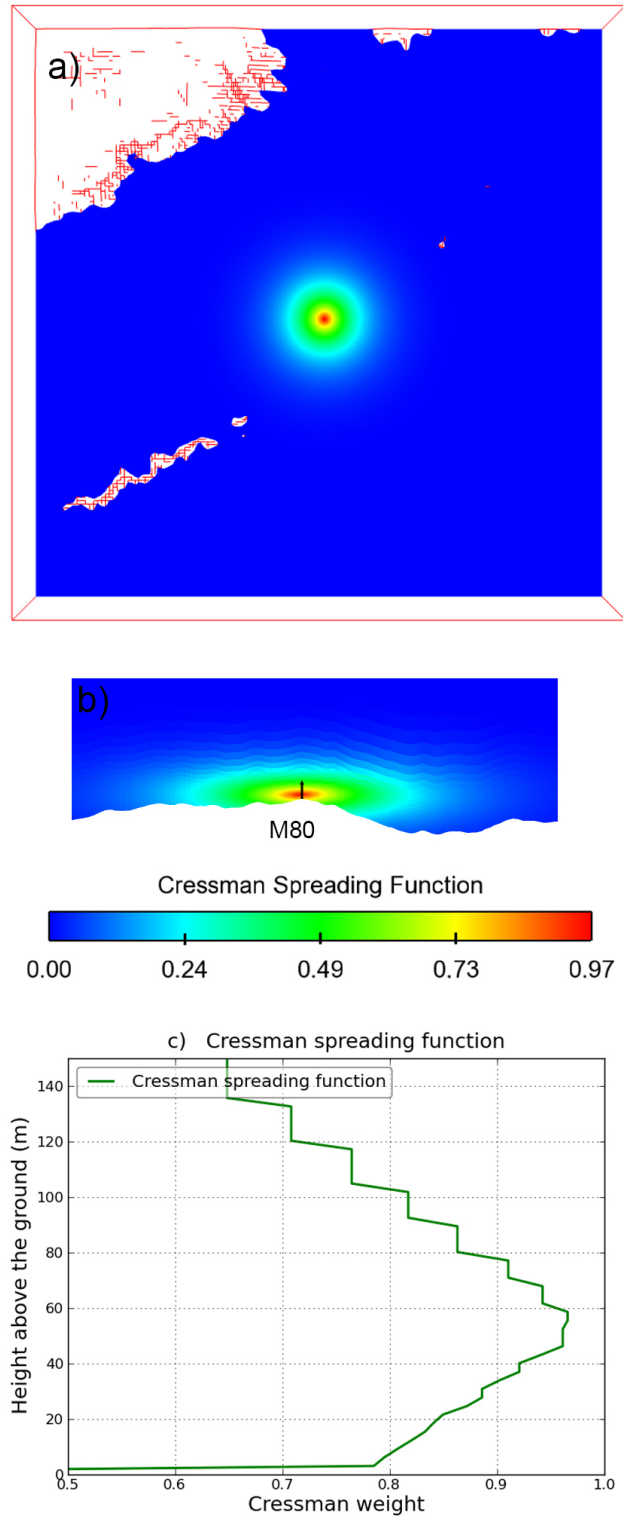


Figure 4.9: Cressman spreading weighting function imposed at mast M80 location: a) Cross-section at  $Z=770$  m, b) Cross-section at  $X= 643697$  m M80 location and c) Vertical profile of Cressman weight function at M80 mast location.

Next, the Cressman spreading function,  $W(x, y, z, t)$  from Eq. (3.17) is computed. Figure 4.9a and 4.9b shows the horizontal and vertical cross-section of the Cressman spreading function applied at the M80 mast location respectively. The Cressman spreading function is imposed at 50 m above ground, which corresponds to the centre of the vertical range covered by sonic measurements. Figure 4.9c shows the plot of Cressman spreading function at M80 location. The value of the Cressman spreading function,  $W(x, y, z, t) = 1$  at 50 m above ground and it drops exponentially outwards to  $W(x, y, z, t) = 0$ . The purpose is to nudge M80 sonic anemometer and monitor the influence of nudging at the M and FP mast location. The radius of influence of volumetric Cressman interpolation and Cressman spreading function are chosen in such way that both masts (M and FP) are inside the assimilation zone. To quantify the value of  $\tau_u$ , sensitivity study was conducted with following values: 35, 50, 65 and 100 s for sonic measurement assimilation.

Figure 4.10 (a-c) and 4.11 (a-c) illustrates the influence of assimilation on the  $u$  and  $v$  velocity components. The figures (a-c) represent CFD simulation without assimilation, CFD simulation with assimilation and difference between CFD simulation without and with assimilation respectively. The horizontal cross-section plane is located at altitude of 770 m, where  $W(x, y, z, t) = 1$ . The CFD simulation with assimilation (figure 4.10b and 4.11b) has adjusted the flow in both  $u$  and  $v$  in comparison with CFD simulation without assimilation (figure 4.10a and 4.11a). Difference between CFD simulation without and with assimilation (figure 4.10c and 4.11c) shows clearly weakening of both  $u$  and  $v$  velocity components. Inside the assimilation zone, strengthening of  $v$  velocity components is also noticed. It is evident that the nudging has modified the wind flow field upstream and downstream of the assimilation location.

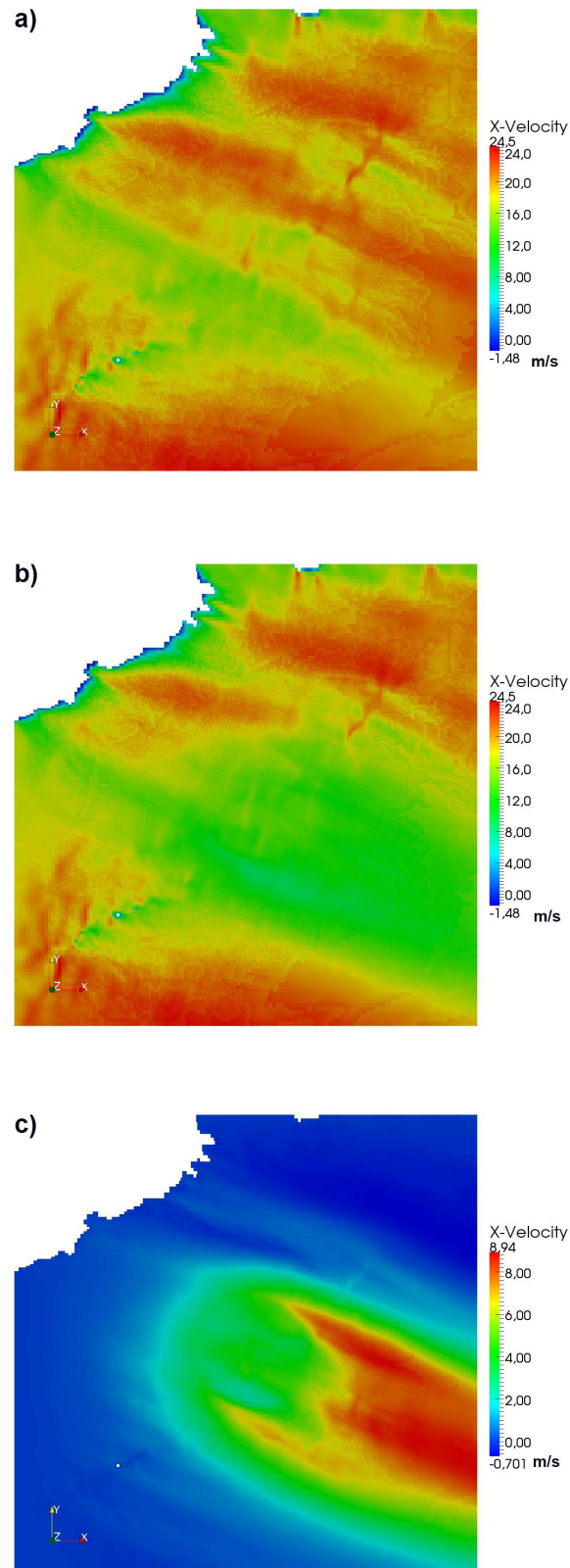


Figure 4.10: Velocity  $u$  component cross-section at 770 m altitude for a) CFD simulation without assimilation b) CFD simulation with assimilation c) difference between the CFD simulation without and with assimilation.

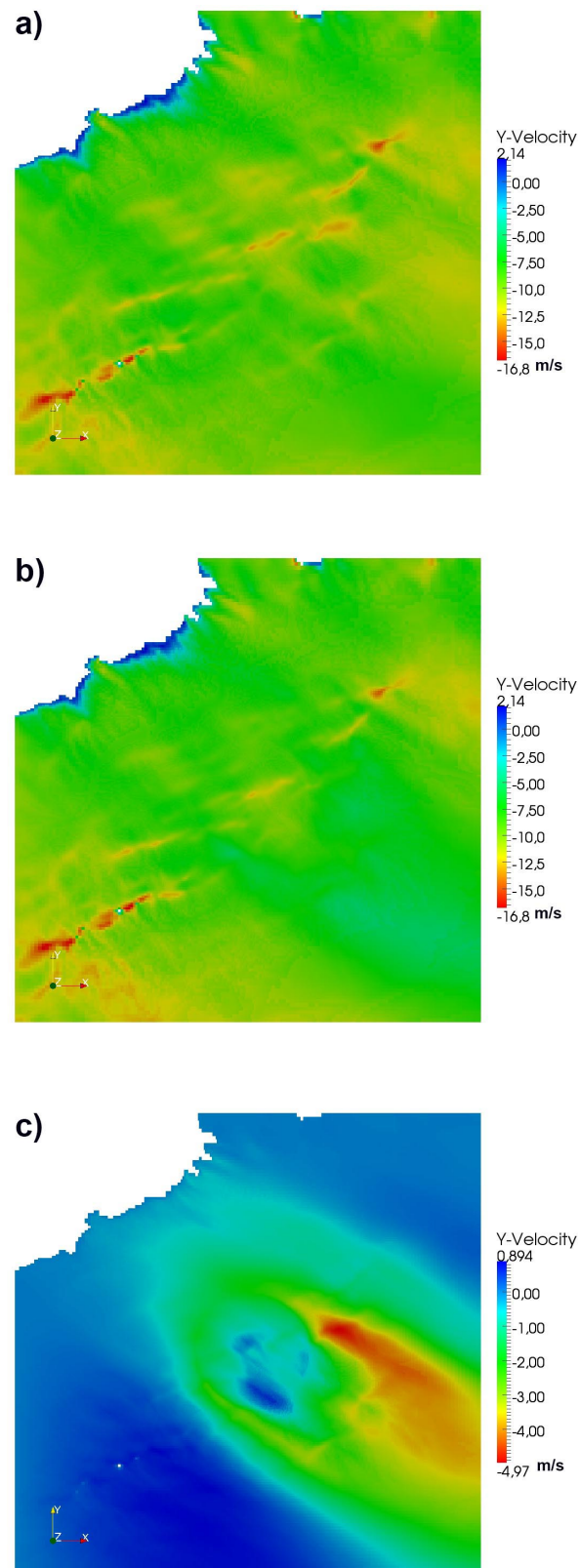


Figure 4.11: Velocity  $v$  component cross-section at 770 m altitude for a) CFD simulation without assimilation b) CFD simulation with assimilation c) difference between the CFD simulation without and with assimilation.

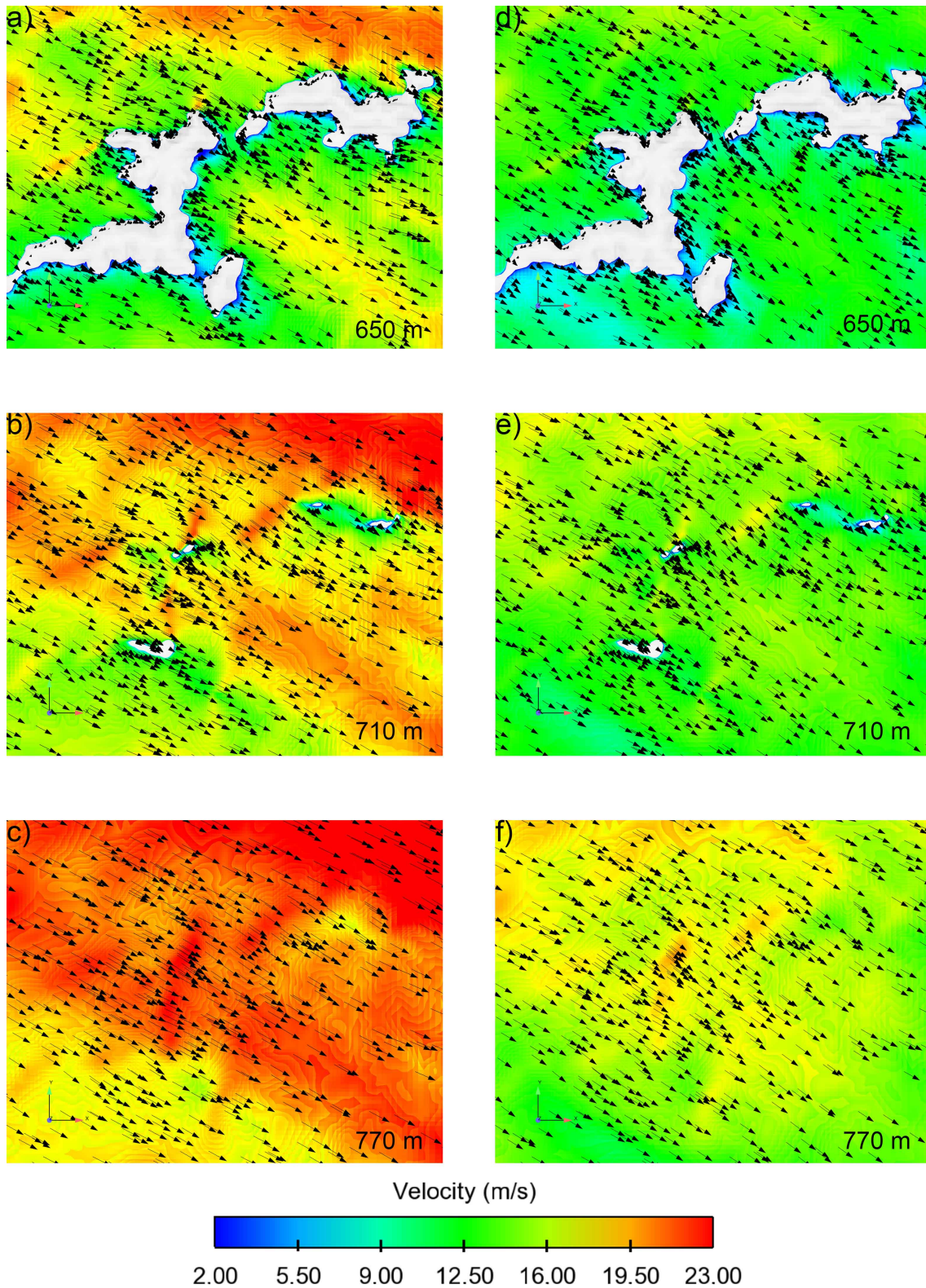


Figure 4.12: Zoom of velocity magnitude and vector cross-section for (a-c) CFD simulation without assimilation and (d-f) CFD simulation with assimilation.

Figure 4.12(a-c) and 4.12(d-f) shows the zoom of velocity magnitude and vector cross-section for CFD simulation without and with assimilation respectively. Figures 4.12a and 4.12d are located at an altitude of 650 m (60 m below the M80 ground level). Figure 4.12b and 4.12e are located at an altitude of 710 m (ground level of M80). Figure 4.12c and 4.12f are located at an altitude of 770 m (60 m above M80 ground level), where  $W(x, y, z, t) = 1$  (nudging is in maximum strength). The figure 4.12(a-f) shows the impact of assimilation on the mean wind speed in the assimilation zone. The over-prediction of mean wind speed at the mast location in the CFD simulation without assimilation was suppressed by nudging the sonic field measurements. Comparison of figures 4.12c and 4.12f shows a difference of 4 m/s in wind speed between CFD simulation without and with assimilation, this is a considerable influence of the nudging procedure.

Figures 4.13 (a-f) illustrate the results of field measurement assimilation at M80 mast location. Field measurement assimilation in CFD is carried out for  $u$  and  $v$  velocity component. In the figures, CFD represents the simulation with Cressman interpolation at inlet faces and without assimilation, and CFD+nudging represents the simulation with Cressman interpolation with field measurement assimilation. Cup, sonic anemometer and sodar for three consecutive averages are also plotted.

Figures 4.13(a-c) represent the  $u$  velocity component profiles,  $v$  velocity component profiles and mean velocity profile at M80 location respectively. CFD profile (green) without assimilation over predicted compared to all the measurements. Nudging the sonic anemometer measurement at 16:00 UTC (yellow square) improved the prediction of CFD+nudging (red). Velocity  $u$  component at M80 location of cup and sonic measurements and CFD+nudging are in very good agreement. In figure 4.13b, the  $v$  velocity component CFD+nudging (red) showed a small improvement compared with CFD (green) without assimilation. From the mean velocity profiles (figure 4.13c) at M80

location, CFD+nudging showed good improvement in predicting wind speed using nudging and the influence on the neighbouring M and FP masts is now detailed.

Figure 4.13d and 4.13e show the *Code\_Saturne* predictions and field measurement data at M and FP masts respectively. At M mast location, CFD+nudging improved the prediction compared to the CFD but still shows an overestimation compared to cup anemometer and long-range sodar measurements. At FP mast location CFD+nudging improved the prediction compared to CFD, but also as mentioned in the previous section a large variability in 10 minutes cup anemometer is seen. CFD simulation with assimilation predictions is in good agreement at M80 and FP mast, at M location the results over predict the wind speed by 11% when compared with cup anemometer and by 30% when compared to sodar at 200 m.

Figure 4.13f shows the turbulent kinetic energy (TKE) measured by sonic anemometers and predicted for CFD simulation without assimilation (green) and CFD simulation with assimilation (red) at M80 location. The 5 consecutive TKE 10 minutes measurements show very large variation. Assimilation of velocity components into the assimilation zone has modified TKE field and predictions of both CFD simulations with and without assimilation are within the range of the measured TKE.

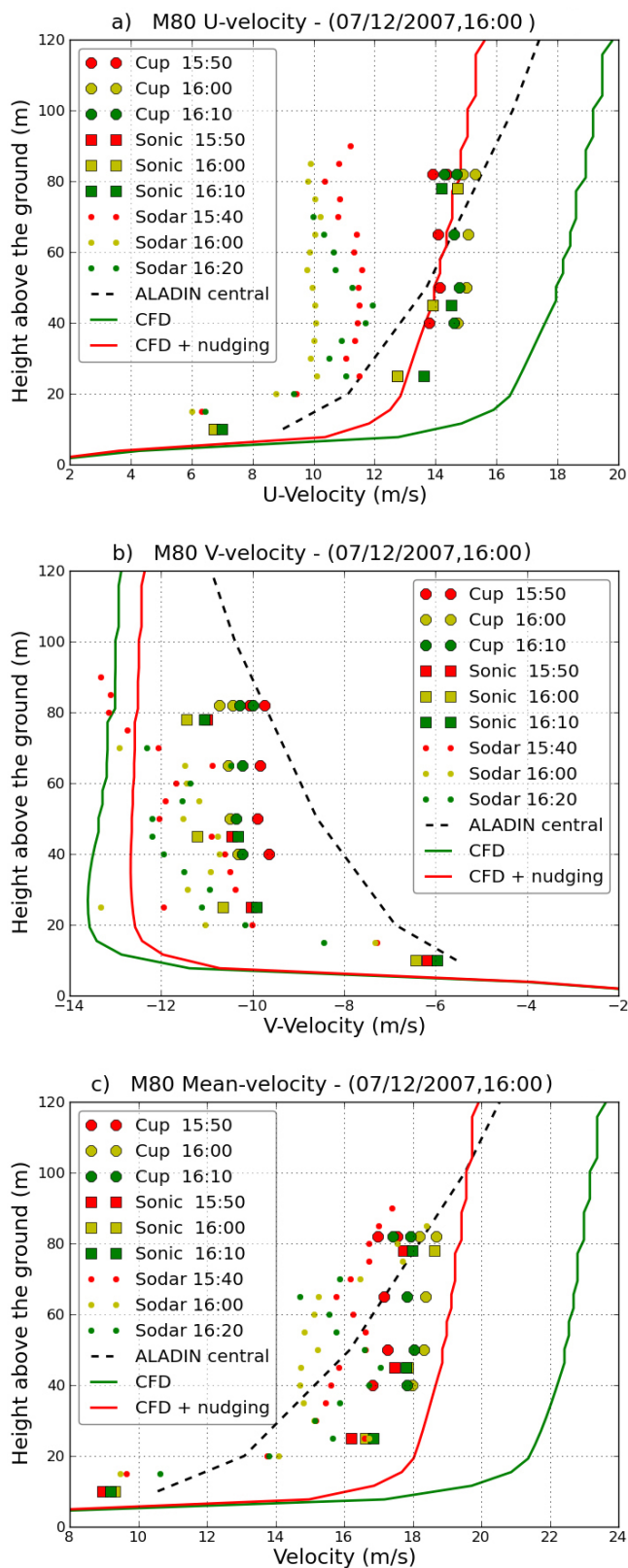


Figure 4.13(a-c): Comparison of field measurements, CFD simulation without and CFD simulation with assimilation at M80.

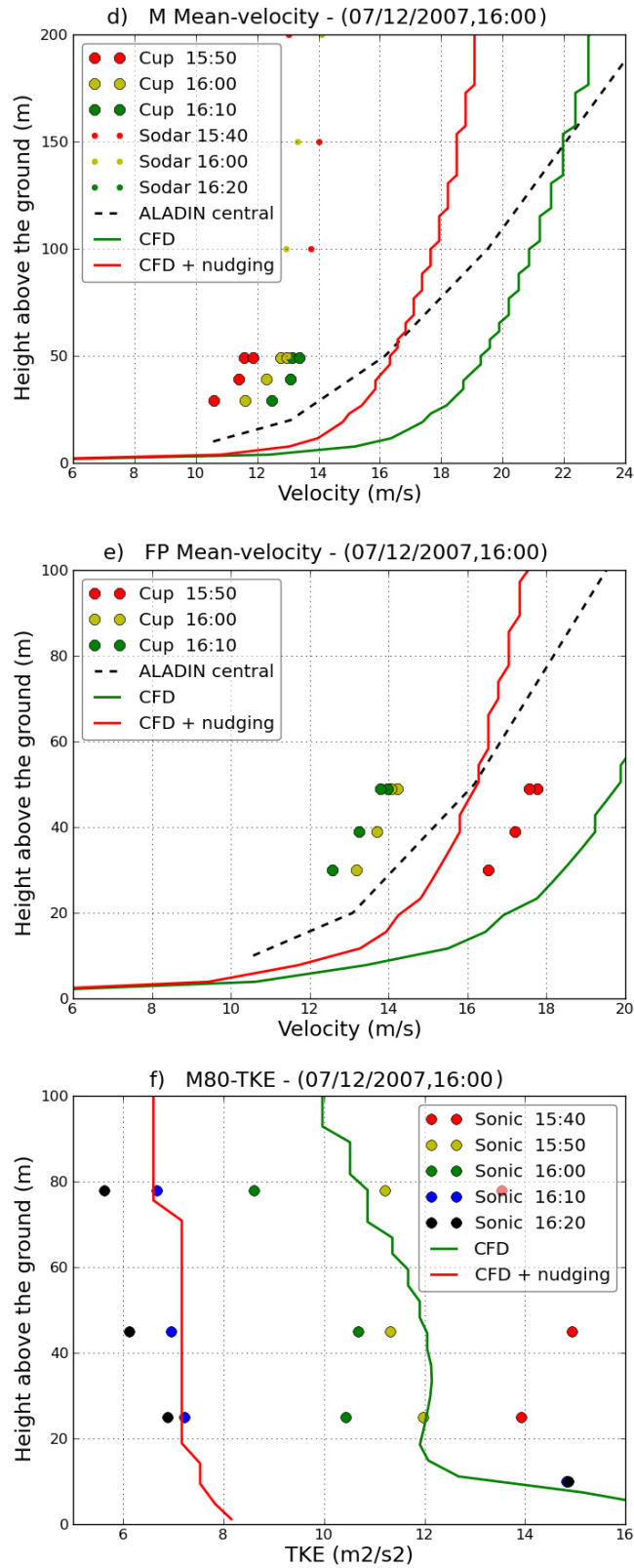


Figure 4.13(d-f): Comparison of field measurements, CFD simulation without and CFD simulation with assimilation at M, FP and M80.

## 4.6. Analysis of two situations

CFD simulations for two main wind directions (Northwesterly and Southeasterly) using Cressman interpolation without assimilation and Cressman interpolation with assimilation are demonstrated. Sonic anemometer measurements are nudged at M80 mast location for both cases. *Code\_Saturne* predicted results are then compared with the field measurements at M and FP mast locations.

### 4.6.1. Northwesterly direction

The Northwesterly case corresponds to the situation on 17<sup>th</sup> November 2007 and the specific time for the CFD simulation is 20:00 UTC. The surface wind speed and temperature are 3.5 m/s and 10 °C respectively. Results are discussed for CFD simulation without field measurement assimilation and CFD simulation with field measurement assimilation. Simulation uses Cressman interpolation of ALADIN wind profiles for imposing inlet boundary condition. Figure 4.14 shows all ALADIN  $u$  and  $v$  velocity components (green and red color) on 17<sup>th</sup> November 2007 at 20:00 UTC and Cressman interpolated  $u$  and  $v$  velocity component (black color) for all inlet boundary faces. ALADIN wind profiles show very large spatial gradients in  $u$  and  $v$  velocity components. The Cressman interpolation ( $r_L$  of 8500 m and  $r_z$  of 100 m) leads to a significant decrease of the gradients on the inlet boundary faces. Sonic anemometer (M80) measurements at 20:00 UTC are nudged into the simulation domain at M80 location.

Figures 4.15(a-c) and 4.15(d-f) present the zoom of the velocity vector and magnitude cross-section at altitude (650, 710 and 770m) close to the mast locations for CFD simulation without assimilation and CFD simulation with assimilation respectively. Figures 4.15(a-c) show that the wind direction in the CFD simulation without assimilation almost comes from the north direction. But the field measurement shows the wind direction is from northwest sector.

Assimilation of sonic field measurement at M80 (figure 4.15(d-f)) shows that wind direction in the assimilation zone has changed to northwesterly. Also the over prediction in the wind speed is also suppressed. They show the significant effect of data assimilation on the wind speed within the zone of interest and also an important effect on the direction, because of the separated assimilation of  $u$  and  $v$  components. Thus data assimilation may allow correcting at least partly some errors in wind speed and direction calculated by the mesoscale and CFD models.

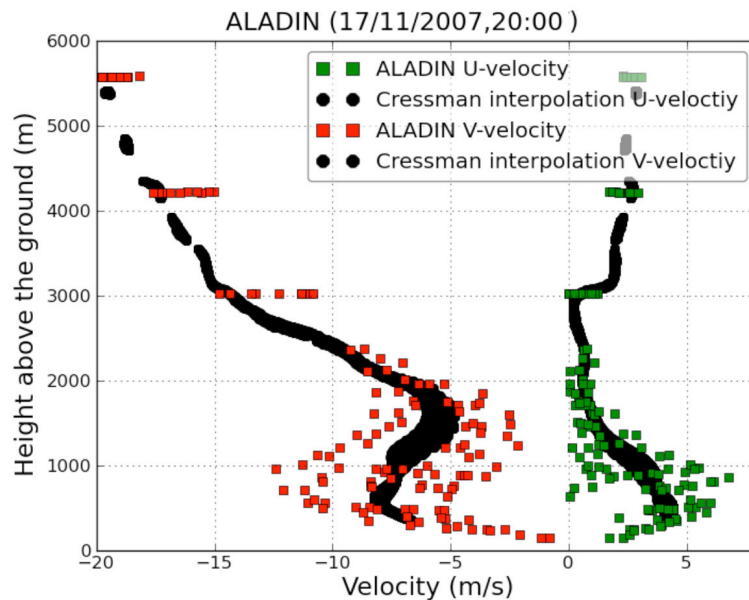


Figure 4.14: Imposed inflow along the north and west boundary using Cressman interpolation for  $r_L=8500$  m and  $r_Z=100$  m.

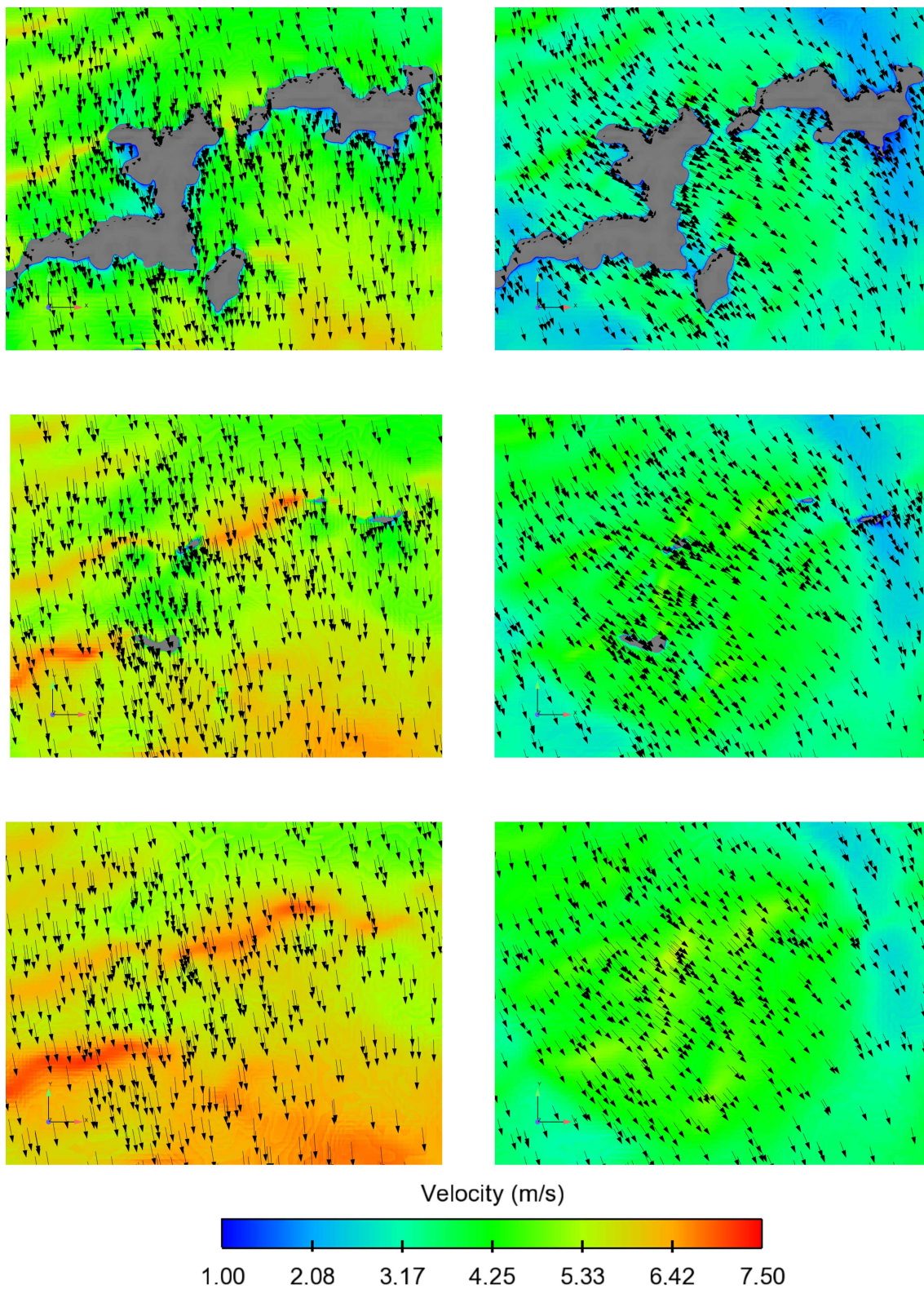


Figure 4.15: Zoom of velocity magnitude and vector cross-section for (a-c) CFD simulation without assimilation and (d-f) CFD simulation with assimilation.

Figures 4.16(a-c) show the comparison of field measurements, CFD simulations without assimilation (CFD) and CFD simulation with assimilation (CFD+nudging) at mast locations. It is to be noted that ALADIN (grid point closest to the masts location) largely over predicts velocity compared to the measurement from three masts. The CFD simulation without assimilation partially corrects this overestimation. The field measurement assimilation allows providing an additional improvement, especially at FP mast, where the CFD simulation with assimilation is in very good agreement with the cup anemometer although there was not any FP measurement assimilation. At M80, the CFD with assimilation is also in very good agreement with the measurements at 80 m, but slightly over predicting the wind speed at lower levels. The CFD profiles are much more mixed on the vertical than ALADIN profiles in which the vertical gradients are largely overestimated. However, the measurements show the maximum speed-up at about 50 m at M80, which is not reproduced in CFD. This could be due to the thermal stratification which is not included in the simulations. Thermal stratification is assessed below using bulk Richardson number,  $R_i$ . The Richardson number is calculated for vertical level between 10m and 80m.

$$R_i = \frac{|g|(\Delta\theta_v)\Delta z}{\theta_v(\Delta U^2 + \Delta V^2)} \quad (4.1)$$

The bulk Richardson number (shown in equation 4.1) for this situation is 0.79, which is higher than the critical Richardson number of 0.25. Therefore the atmosphere is under dynamically stable conditions. The current simulations assume the atmosphere to be in neutral conditions. At M location, variability in the three consecutive 10 minutes average is noticed, and CFD+nudging better compares to measurements at 20:00 than CFD simulation without nudging. Long-range sodar measurements at M location are not available for this situation.

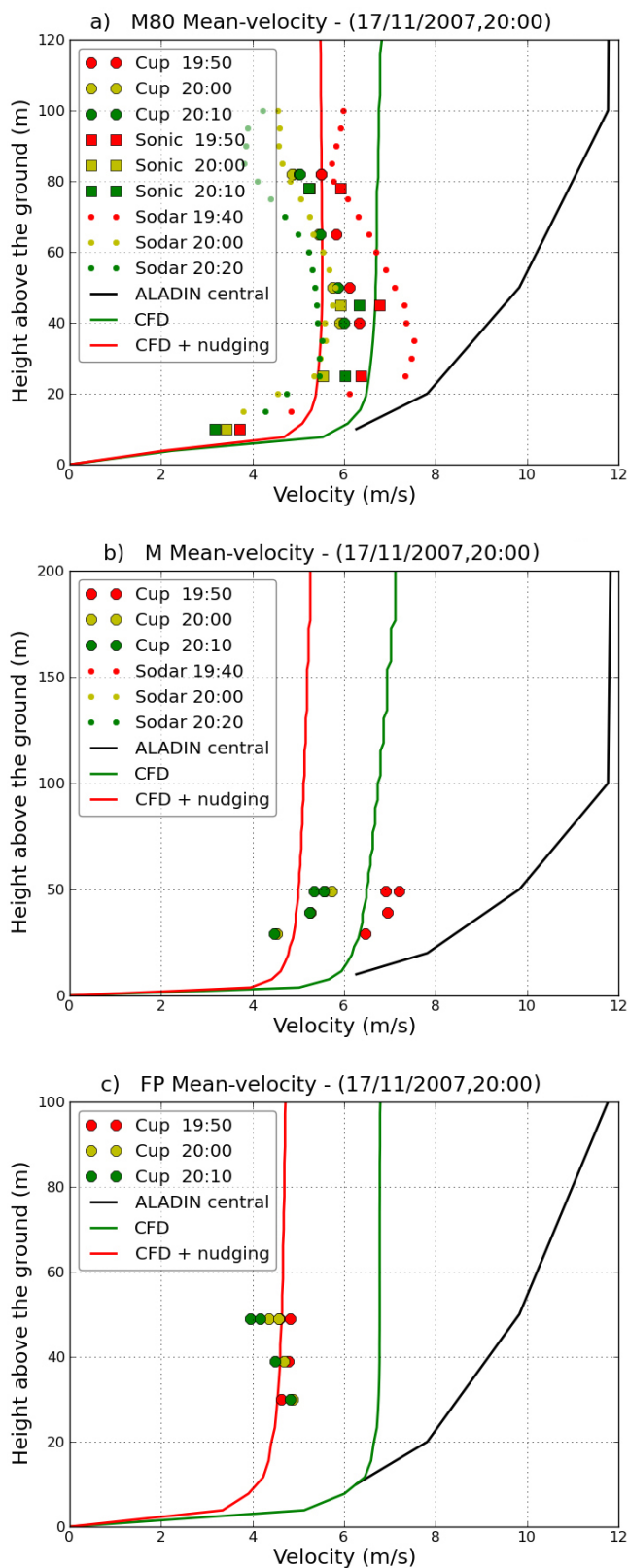


Figure 4.16: Comparison of velocity profiles between measurement, CFD simulation with and without assimilation at M80, M and FP mast location.

#### 4.6.2. Southeasterly direction

Southeasterly case corresponds to the situation 03<sup>rd</sup> October 2007 at 18:00 UTC. The wind flows from the plains into the hills (area of interest), wind direction is exactly opposite of the Northwesterly dominant wind direction. The surface wind speed and direction are 4 m/s and 160° respectively and surface temperature of 15 °C. Results are discussed for CFD simulation without field measurement assimilation and CFD simulation with field measurement assimilation. Figure 4.17 shows all ALADIN  $u$  and  $v$  velocity components (green and red respectively) along with the Cressman interpolated velocity components for south and east boundary. Cressman interpolation uses ALADIN wind profiles closest to the South and East of the simulation domain. The use of Cressman interpolations for inlet boundary condition have significantly reduced the gradients in the  $u$  velocity component, while the ALADIN  $v$  velocity component shows no such large gradients. Sonic anemometer measurement at 18:00 UTC is nudged to the simulation domain at M80 location.

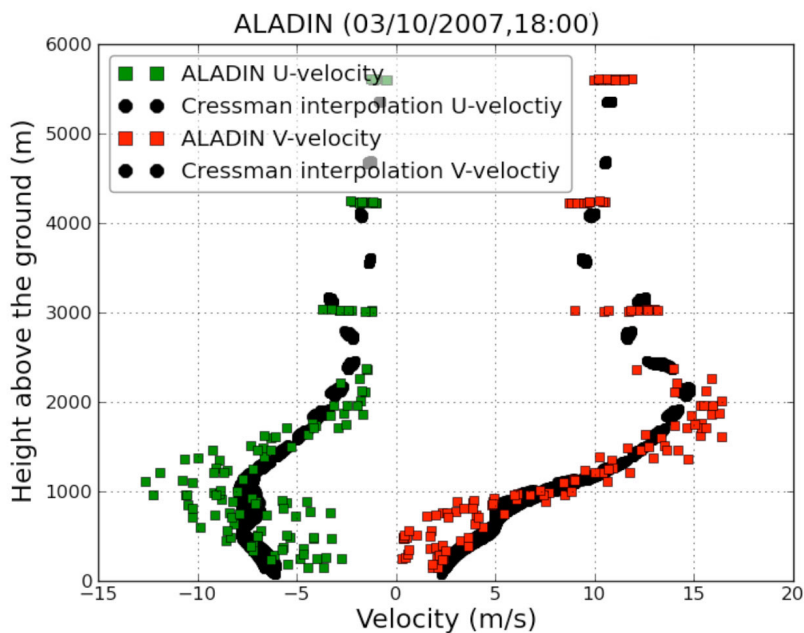


Figure 4.17: Imposed inflow along the north and west boundary using Cressman interpolation for  $r_L=8500$  m and  $r_Z=100$  m.

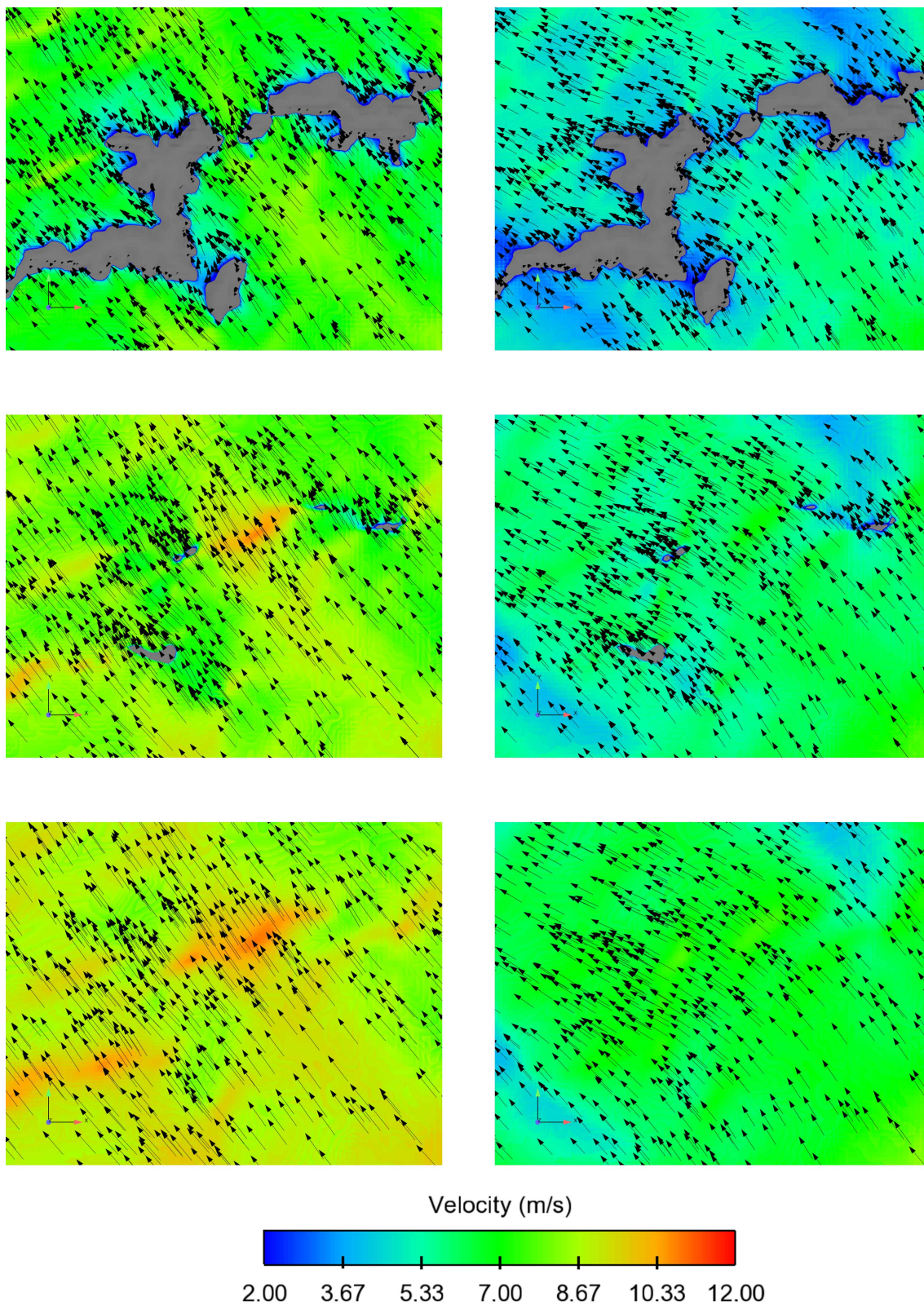


Figure 4.18: Zoom of velocity magnitude and vector cross-section for (a-c) CFD simulation without assimilation and (d-f) CFD simulation with assimilation.

Figure 4.18(a-c) and (d-f) present the zoom-up of the velocity vector and magnitude cross-section at altitude (650, 710 and 770 m) close to the mast locations for CFD simulation without assimilation and CFD simulation with assimilation respectively. Figure 4.18(a-c) shows the wind flow from southeasterly direction throughout the entire domain, while figure 4.18(d-f) shows the influence of assimilating sonic measurement and change in direction slightly westward in the assimilation zone and downstream. Also considerable reduction in velocity magnitude is noticed in the figure 4.18(d-f).

Figures 4.19(a-c) show the comparison of field measurements, CFD simulations without assimilation (CFD) and CFD simulation with assimilation (CFD+nudging) at M80, M and FP mast locations. At M80 location, cup and sonic measurements are in good agreement while the sodar measurements were widely spread and they are not reliable at M80. In this situation, ALADIN largely under predicted wind speed compared to the measurements of the three masts. On the contrary, the CFD simulation without assimilation leads to an overestimation, which is well corrected in the CFD simulation with assimilation of the M80 sonic anemometer measurements. At M location, long-range sodar measurements are consistent. Cup and sodar measurements give the complete wind profile until 200 m. The results of CFD simulation with assimilation are in very good agreement with measurements especially at M80 and FP.

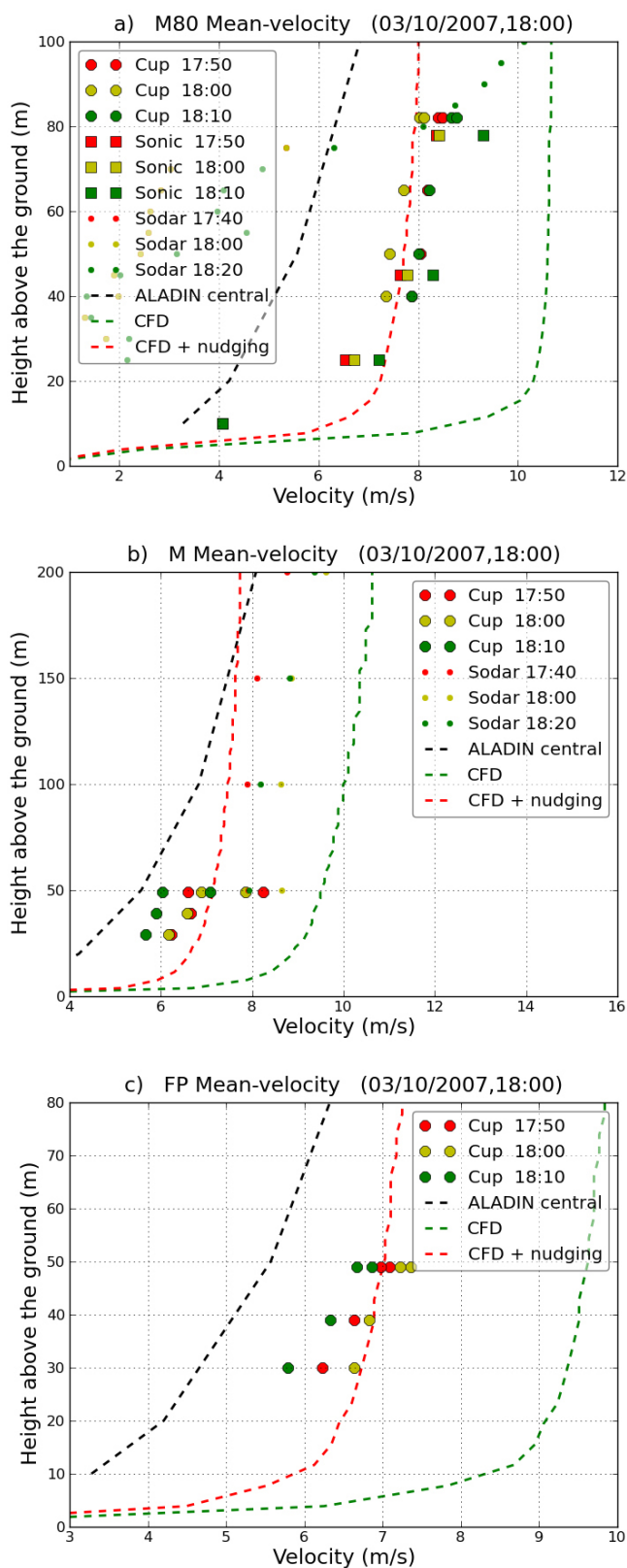


Figure 4.19: Comparison of velocity profiles between measurement, CFD simulation with and without assimilation at M80, M and FP mast location.

## 5. Computation of the annual average wind speed

The methodology shown in figure 2.11 is used to calculate the annual average wind speed at the 3 masts locations and compare with the field measurements and WAsP results. Annual wind speeds are calculated using the methodology without and with assimilation. The clustering process of the yearly mesoscale data for the site reduces the number of situations necessary to simulate for 1 year. In this analysis, the same clustering method used by Laporte (2008) is implemented to compare the previous results with the current methodology. In Laporte (2008), the number of situations is reduced to 64 cluster centers. The CFD simulations are carried out for those 64 cluster centers. CFD simulations without assimilation use only Cressman interpolation of mesoscale data (ALADIN) for inlet boundary, while CFD simulation with assimilation uses Cressman interpolation for inlet boundary and assimilation of cup anemometer measurements inside the CFD domain for yearly analysis. Hourly mesoscale data and hourly averaged cup anemometer measurements at M80 are used for the current methodology.

Hourly averaged wind speed and direction of the cup anemometer measurements at M80, M and FP mast location are compared with CFD simulations without and with assimilation. Finally, annual average wind speed is computed for CFD simulation without and with assimilation and compared with measurements, WAsP results at M80, M and FP mast locations. Comparisons are performed for hourly average at the mast locations between the cup anemometer measurement and CFD simulation results without and with assimilation.

### Preliminary comparisons

Coupling mesoscale and microscale models is a better modeling approach than mesoscale model alone as discussed in chapter 2 and it has proven to be successful in capturing detailed flow dynamics. It is important to note, that CFD simulation results are dependent on the accuracy of the inlet mesoscale model

data. Therefore, ALADIN mesoscale data used in this study was first compared to M80 mast measurements at 50m. Figure 5.1a and 5.1b, shows the difference between mesoscale data and M80 mast at 50 m. The mesoscale data over predicts wind speed compared to M80 mast measurements. ALADIN predictions are mostly higher with the largest difference of  $\approx 8$  m/s. Concerning the wind direction, 14 cases correspond to a difference larger than  $30^\circ$ , which may lead to inaccuracy in CFD modeling. It provides further evidence to the fact, that mesoscale model results alone should not be used for accurate wind resource assessment in complex terrain and that there is a need to downscale mesoscale data in order to take into account the topography at high resolution and to include local data with data assimilation.

In this methodology, M80 cup anemometer measurements are assimilated for all the 64 clusters. This should correct the CFD predictions at M80 and is expected to improve the CFD predictions at M and FP mast locations. Therefore, it is important to analyze the differences in flow field between each of these mast locations. Figure 5.2a and 5.2b shows the difference of wind speed and direction between the M80 (50m) and M (50m) cup anemometer measurements, respectively. Most of the clusters show less wind speed difference with a maximum difference of  $\approx 4$  m/s. The mean absolute error of wind speed, for the entire 64 clusters, is  $\approx 1.5$  m/s. Large differences in direction are observed between M80 and M in certain clusters. The difference in direction could be due to complex topography, direction of incoming wind speed and local thermal effects.

Figure 5.3a and 5.3b shows the difference between the M80 (50m) and FP (50m) cup anemometer measurements of wind speed and direction. Both M80 and FP masts are located on the top of the hill with similar conditions. FP cup measurements for the first 14 clusters are unavailable. The differences are in the same order of magnitude as between M80 and M. The largest difference is  $\approx 4.5$  m/s and the mean absolute error is  $\approx 1.5$  m/s. From the figure 5.3a and 5.3b it is noticed that the difference (M80-FP) in wind speed is mainly positive

and difference in direction is negative. Assimilating M80 cup measurements into the CFD model, should influence the CFD model results at M and FP mast locations. Hence, M and FP are located within the assimilation zone.

Three sets of data are available for nudging – cup, sonic anemometer and sodar at M80. Sodars at M80 and M and sonic anemometers data are only available for the second half of the year 2007; hence we choose to assimilate M80 cup anemometer measurement data for the 64 cluster centers for annual average calculation. The hourly cup anemometer measurements at M and FP are used for validation and verification of the assimilation procedure and don't enter the assimilation model. However, before the results over the whole year 2007, a comparison between the results with sonic data assimilation and cup anemometers data assimilation is presented over the second half of the year.

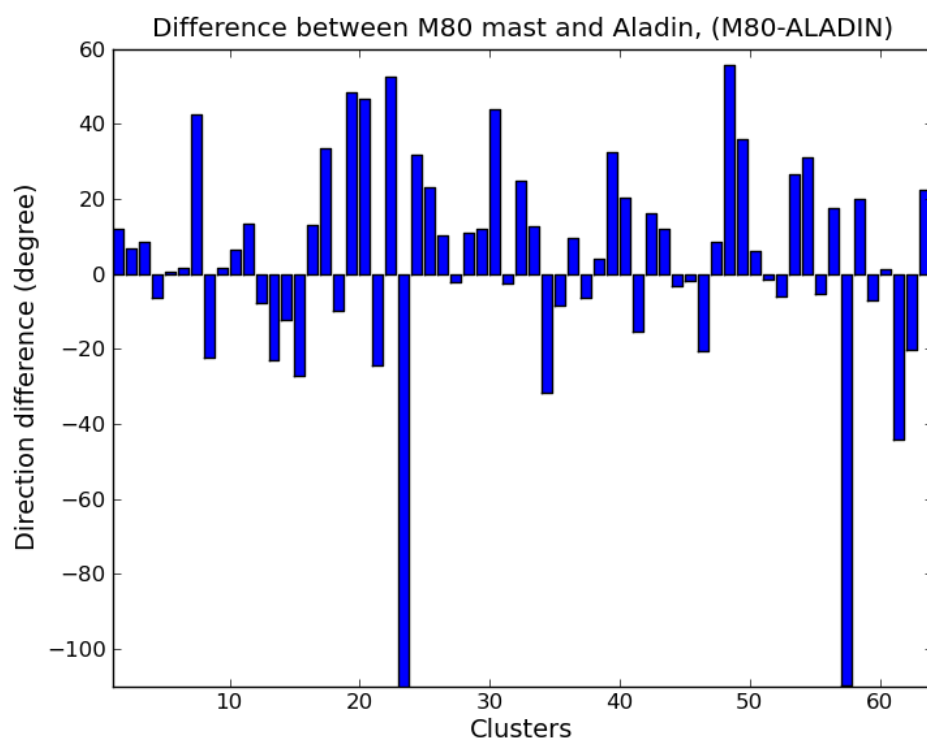
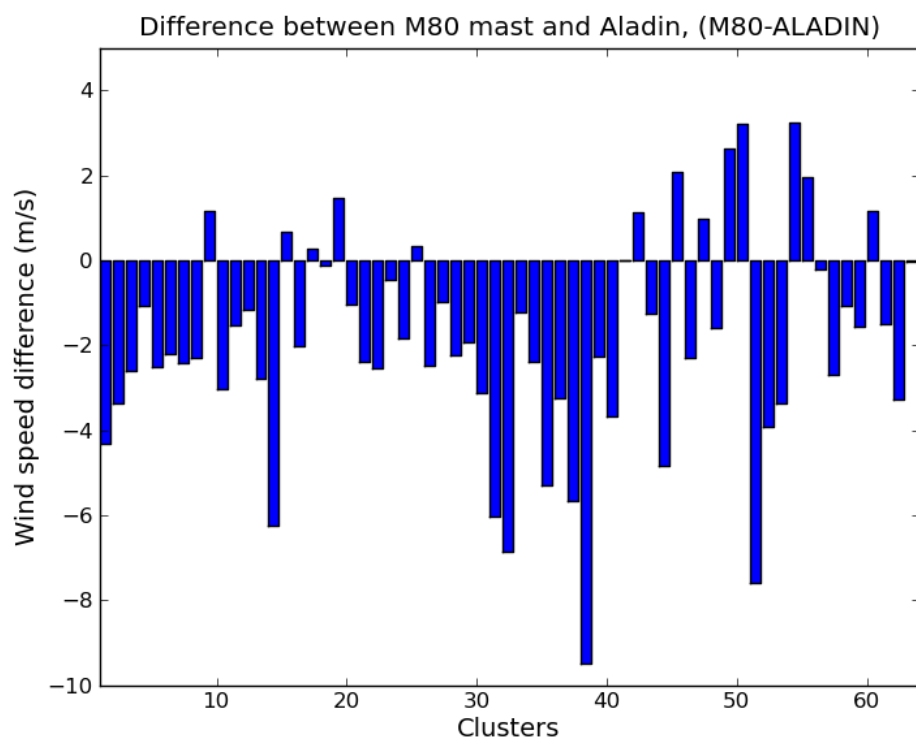


Figure 5.1: Difference between M80 and ALADIN a) wind speed b) wind direction

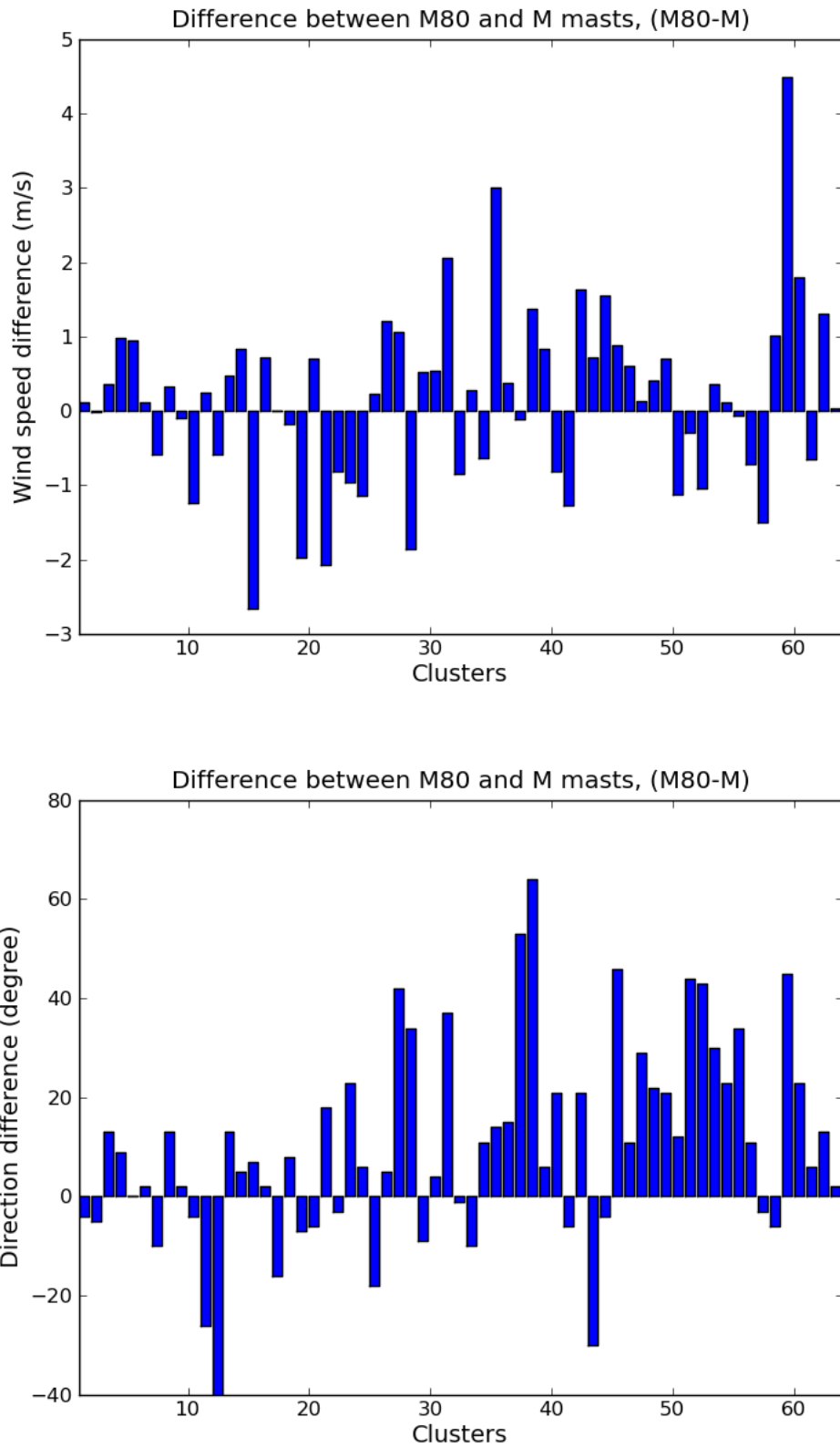


Figure 5.2: Difference between M80 and M mast at 50m a) wind speed b) direction

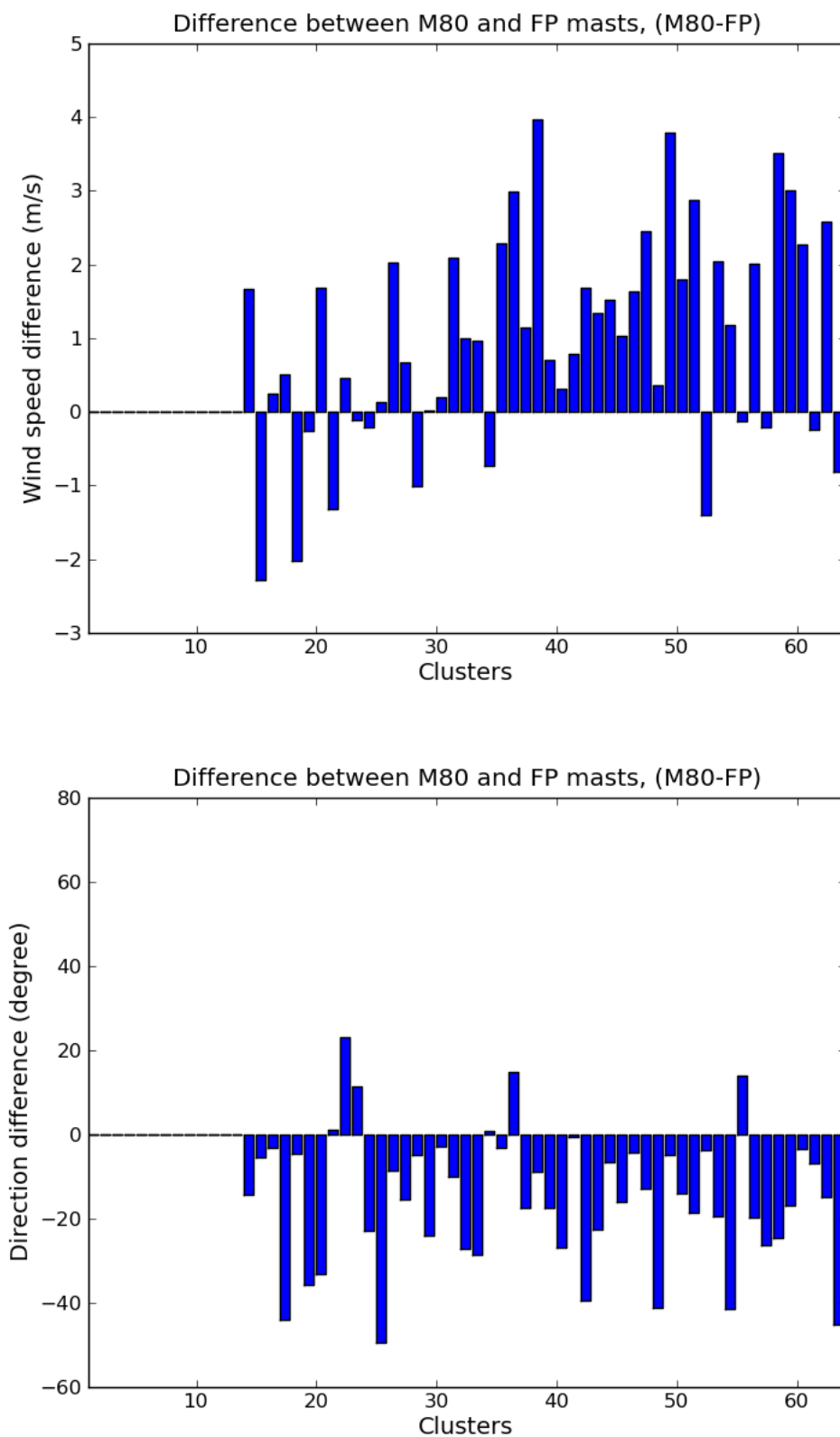


Figure 5.3: Difference between M80 and FP mast at 50m a) wind speed b) direction

### 5.1. CFD simulations with sonic and cup anemometer assimilation

In this section, a sensitivity analysis for assimilating sonic and cup anemometer for two northwesterly cases are analyzed. The M80 mast location is chosen as common location for both sonic and cup anemometer nudging. At M80 location, sonic anemometer measurements are located at 10, 25, 45 and 78 m and cup anemometer measurements are located at 40, 50, 65 and 82 m. Sensitivity analysis for sonic anemometer assimilation was explained in chapter 4. Both cup and sonic anemometer measurements are nudged at 50 m above the M80 mast location, which result in  $W(x, y, z, t) = 1$ . At first, the volumetric Cressman interpolation parameters (longitudinal and vertical radius of influence) have to be determined for cup anemometer assimilation. The longitudinal radius of influence of sonic anemometer assimilation of 600 m is chosen for cup assimilation in order to have same horizontal extent of assimilating zone. In sonic assimilation, 10m height measurements are available and vertical radius of influence of 150m results in  $W(x, y, z, t) = 0.8$  close to the ground. In cup assimilation, vertical radius of influence of 10 m is used in order to drop the  $W(x, y, z, t)$  to 0 close to the ground. This will nudge the cup measurements only close to the heights where the measurements are available.

The relaxation timescale,  $\tau_u$  value is chosen to modify the CFD solutions towards the measurements. Higher  $\tau_u$  values results in less forcing and gives priority to the CFD solution and vice-versa. To quantify the value of  $\tau_u$  for cup nudging, sensitivity analysis was conducted with following values: 50, 25, 15, 5, 2 and 1 s. From the figure 5.3 lower  $\tau_u$  values results in increased wind speed close to the ground and higher  $\tau_u$  values has weak nudging. Table 5.1 provides the nudging parameters for sonic and cup assimilation. In sonic and cup nudging,  $\tau_u$  value of 50 and 5 s, respectively, were used for all the simulations.

The large difference between two different values of  $\tau_u$  is that sonic and cup nudging uses different radius of influence for  $r_L$  and  $r_z$  and hence requires different forcing (nudging coefficient) for correcting the CFD solution towards the measurements.

Table 5.1 Nudging parameters for sonic and cup assimilation

Parameters	Sonic assimilation	Cup assimilation
Longitudinal radius of influence, ( $r_L$ ) m	600	600
Vertical radius of influence, ( $r_z$ ) m	150	10
Nudging coefficient, ( $\tau_u$ ) s	50	5

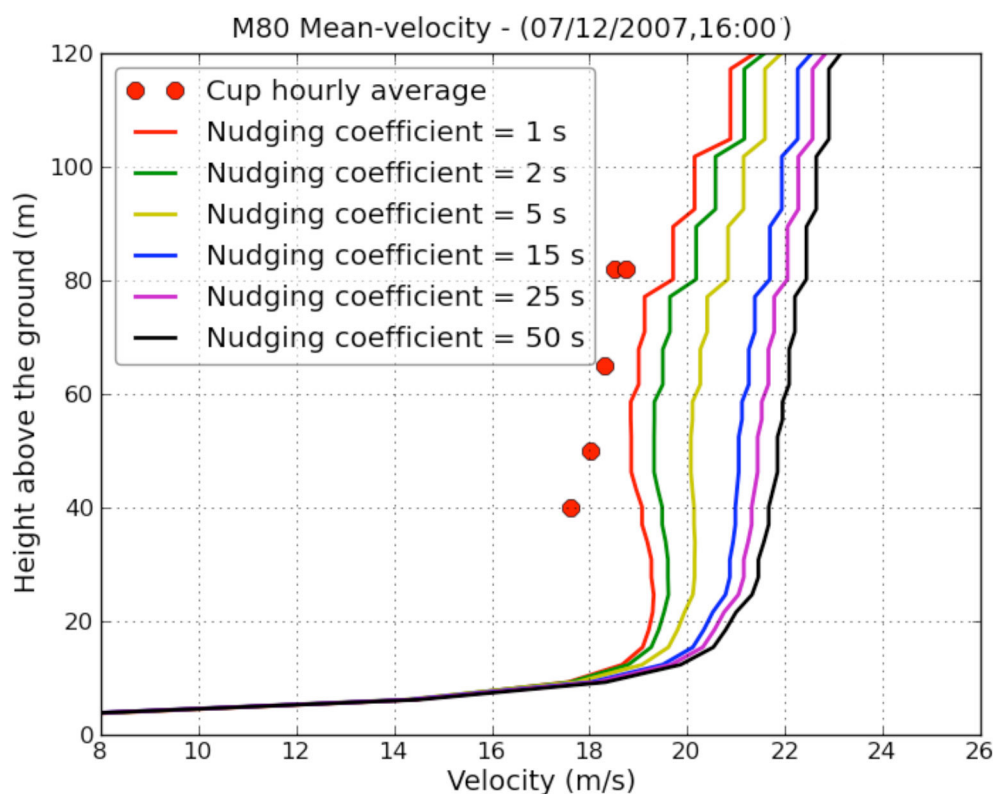


Figure 5.4: Sensitivity analysis of nudging coefficient for CFD simulation with cup assimilation.

The first northwesterly case corresponds to the simulation on 07<sup>th</sup> November 2007 and the specific time for the CFD simulation is 04:00 UTC. Hourly

averaged cup and sonic anemometer measurements are used for assimilation. Figure 5.5 (a-c) shows the comparison of velocity profile between hourly averaged measurements, CFD simulation with sonic and cup assimilation at M80, M and FP. Hourly averaged cup and sonic anemometer data are in good agreement with each other at M80 mast location. CFD simulation predictions of both sonic and cup anemometer assimilation are also in good agreement with each other and with the measurements (as shown in figure 5.5a). At M and FP only hourly averaged cup anemometer measurements are available which are compared to CFD predictions. At M location, both CFD simulation with sonic and cup assimilation predicts reasonably well, while CFD simulation with cup assimilation predicted slightly higher wind speed close to the ground compared to the measurements. At FP location both CFD simulations with sonic and cup assimilation over predict the measurement by  $\approx 2\text{m/s}$ .

The second northwesterly case corresponds to the simulation on 17th November 2007 and the specific time of the simulation is 20:00 UTC. Figure 5.6 (a-c) show the comparison of velocity profile between hourly averaged measurements, CFD simulation with sonic assimilation and CFD simulation with cup assimilation at M80, M and FP. The hourly average of cup and sonic anemometer are in good agreement from 40m to 80m, while a significant reduction in wind speed is observed below 40m in sonic measurements. In figure 5.6a, CFD simulation with sonic assimilation predicts better compared to cup assimilation. Cup assimilation over predicts the wind speed close to the ground at M80 and this could lead to positive bias in annual mean wind speed. At M location, CFD simulation with cup assimilation is in good agreement with the measurements and CFD simulation with sonic assimilation under predicts compared to measurements. At FP location CFD simulation with sonic assimilation predicts well compared to CFD simulation with cup assimilation.

In the first case CFD simulations with cup and sonic assimilation perform equally well, while in the second case CFD simulation with sonic assimilation performed better than cup assimilation at M80 nudging location.

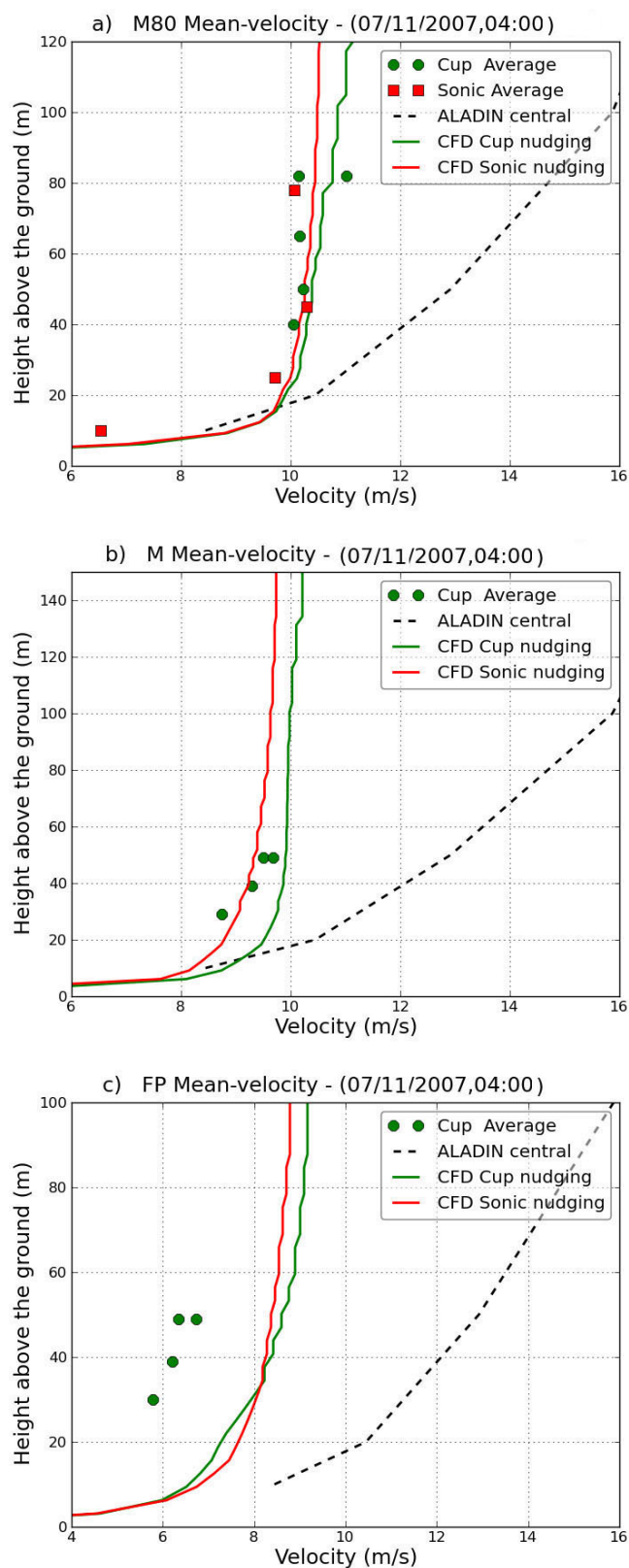


Figure 5.5: Comparison of velocity profile between hourly averaged measurements, CFD simulations with cup and sonic assimilation at M80, M and FP location.

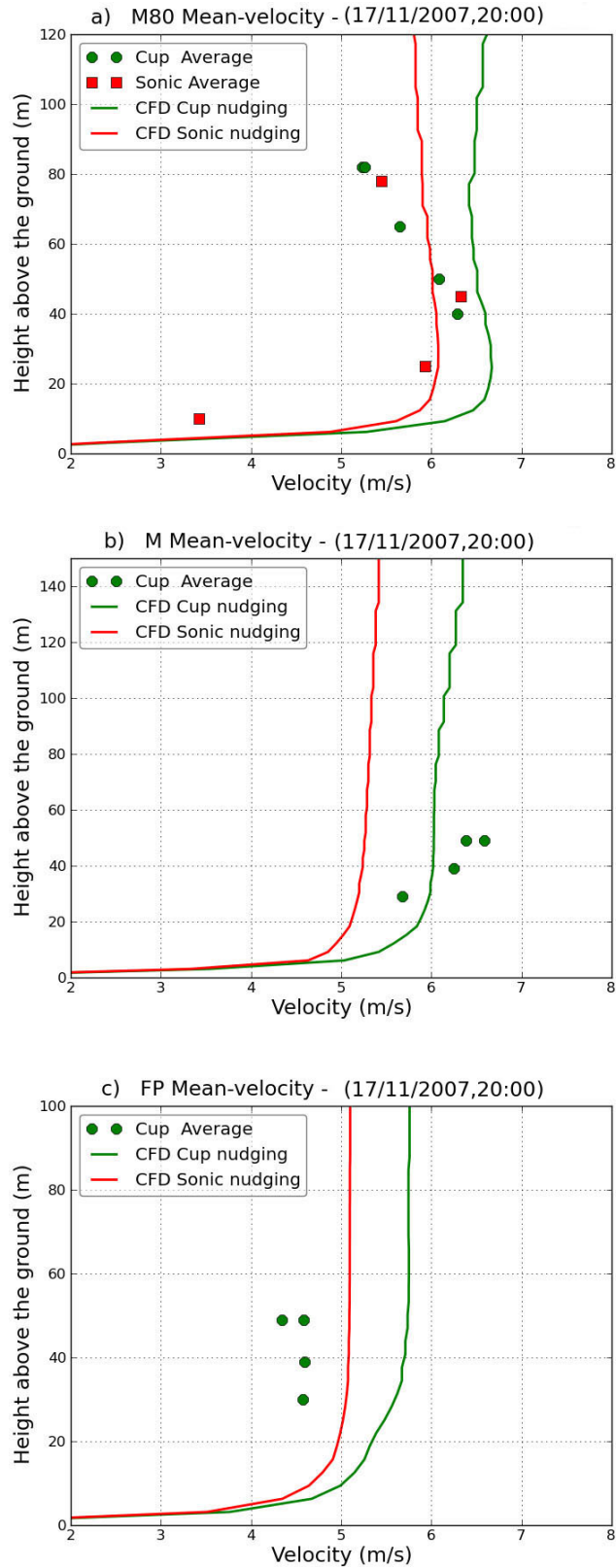


Figure 5.6: Comparison of velocity profile between hourly averaged measurements, CFD simulations with cup and sonic assimilation at M80, M and FP location.

Sonic anemometer measurements are available from 23th June 2007 to 31<sup>st</sup> December 2007. Comparison between CFD simulations carried out without assimilation, with cup and sonic assimilation for 15 clusters (36<sup>th</sup> to 50<sup>th</sup> cluster) is discussed below. Figure 5.7-5.9 represents the difference between the hourly averaged cup anemometer measurements and simulated wind speed and wind direction at M80 (80m), M (50m) and FP (50m) mast locations respectively. At M80 location, CFD simulations with cup assimilation have predicted better wind speeds compared to CFD simulation with sonic assimilation for these 15 clusters, while the direction (figure 5.7a&b) is predicted better in both CFD simulations with cup and sonic assimilation.

At M location, CFD simulations without assimilation show large difference in wind speeds in a few clusters (in figure 5.8a), while CFD simulations with cup and sonic assimilation have reduced the difference compared to measurements. CFD simulations without assimilation lead to a mean absolute error of  $\approx 2.9$  m/s at M80 location for the 15 clusters centers. While CFD simulations with cup assimilation and CFD simulations with sonic assimilation show good reduction in mean absolute error (MAE $\approx 0.5$  m/s and  $\approx 0.85$  m/s respectively). Also at M mast location, CFD simulations with cup assimilation have predicted wind speed better compared to CFD simulations with sonic assimilation. Reasonable improvements in wind direction are observed with both cup and sonic assimilation compared to traditional CFD simulations (figure 5.8b). At FP location, similar trends as in M mast location are observed (as shown in figure 5.9a and 5.9b). CFD simulations with cup assimilation (at M mast, MAE  $\approx 0.78$  m/s and at FP mast, MAE  $\approx 1.04$  m/s) and CFD simulations with sonic assimilation (at M mast, MAE  $\approx 1.24$  m/s and at FP mast, MAE  $\approx 1.32$  m/s) have also shown good reduction in mean absolute error compared with CFD simulations without assimilation (at M mast, MAE  $\approx 2.73$  m/s and at FP mast, MAE  $\approx 2.8$  m/s) at M and FP mast location.

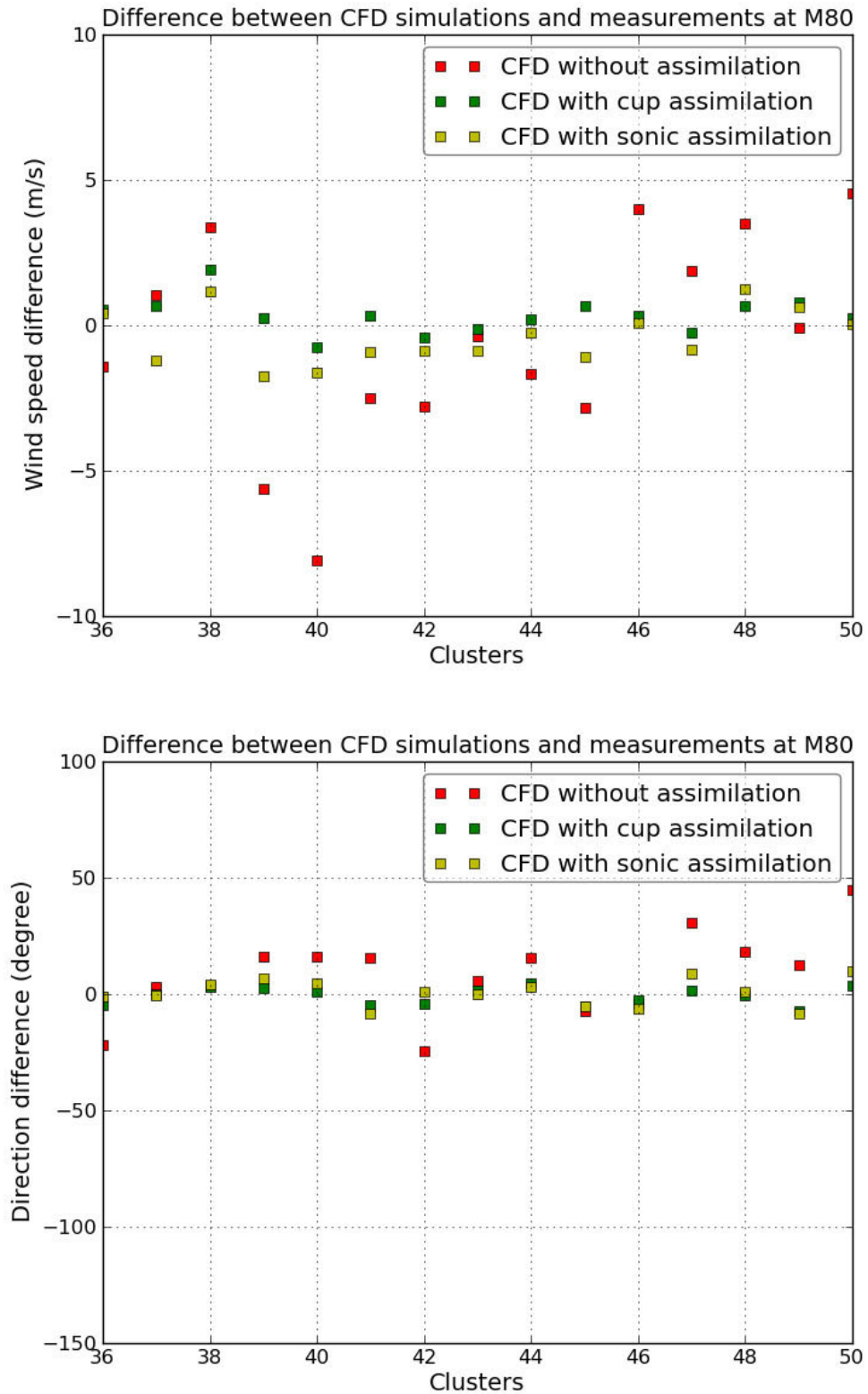


Figure 5.7: Difference between CFD simulations without assimilation and measurements, CFD simulations with cup assimilation and measurement and CFD simulations with sonic assimilation and measurement at M80 (80m) a) wind speed b) direction.

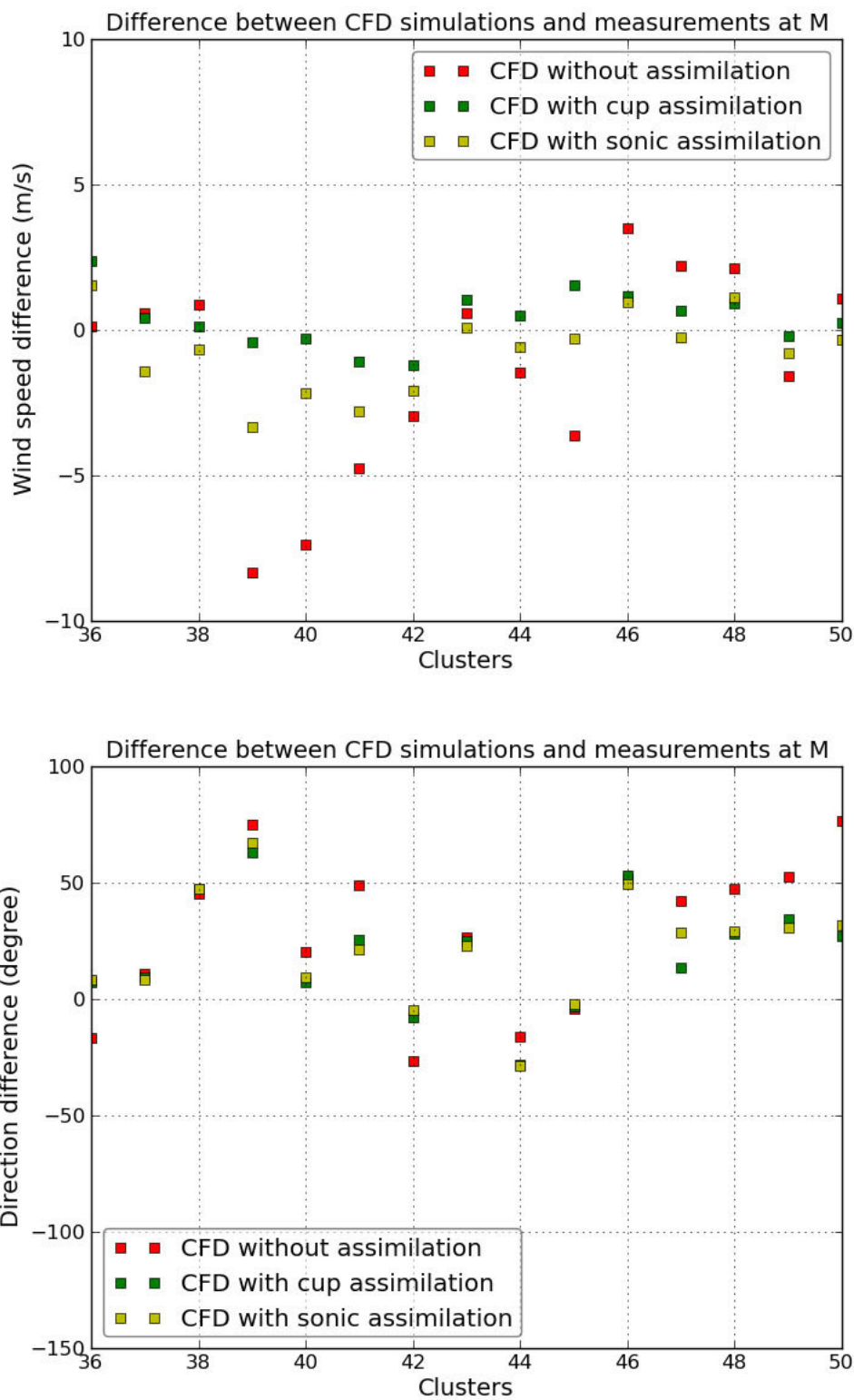


Figure 5.8: Same as figure 5.7 but for M(50m)

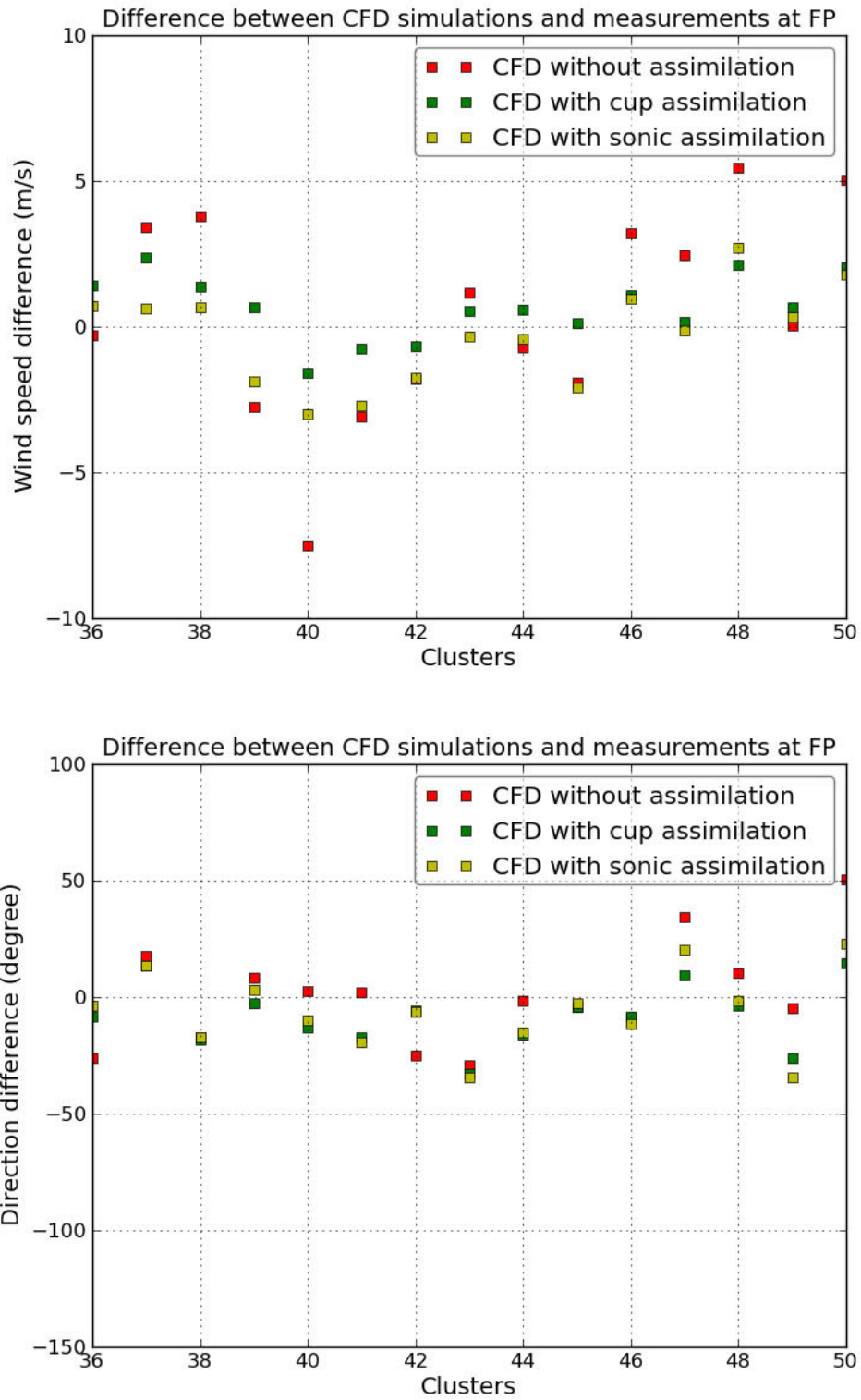


Figure 5.9: Same as figure 5.7 but for FP(50m)

## 5.2. Comparisons of CFD simulation without and with assimilation on the yearly average

In view of an annual energy production computation, the yearly averaged wind speed at the 3 mast locations using cup anemometer measurements are compared to CFD results. This provides an insight on how CFD without and with assimilation have performed over the entire set of clusters. Figure 5.10-5.12(a-b) represents the difference between the hourly averaged cup anemometer measurements and simulations for wind speed and wind direction at M80 (80m), M (50m) and FP (50m) mast location.

CFD simulations without assimilation (red square), in figure 5.10a, have a maximum difference of  $\approx 9$  m/s for a few clusters and with mean absolute error of  $\approx 2.72$  m/s observed at M80 location for all the 64 clusters. While nudging cup anemometer measurements at M80, CFD simulations with assimilation (green square) show good reduction in mean absolute error, which is  $\approx 0.65$  m/s. Figure 5.10b shows the direction difference (in degrees) between the measurement and CFD simulation without and with assimilation. An overall reduction in direction difference is observed, while performing CFD simulations with assimilation. This reduction of error is expected at M80 as the assimilation is performed with data provided by this mast. Below, the influence of the assimilation at M80 over the neighboring 2 masts (M and FP) will be analyzed.

Figure 5.11 and 5.12 shows the difference between measurements and CFD simulation without and with assimilation for the entire 64 clusters at M and FP. Figure 5.11a and 5.12a shows the difference between wind speeds and figure 5.11b and 5.12b shows the difference in directions. CFD simulations with assimilation have shown good reduction in wind speed mean absolute error ( $\approx 0.97$  m/s at M and  $\approx 1.13$  m/s at FP) compared with CFD simulations without assimilation ( $\approx 2.8$  m/s at M and  $\approx 2.38$  m/s at FP). As seen at M80, CFD simulations without assimilation have higher difference in wind speed and direction at both M & FP. From figure 5.11b we notice good improvement in

direction in the first half of the 64 clusters with CFD simulation with assimilation and in the second half of 64 clusters higher difference with measurements are noticed. This can be explained by figure 5.2b, which shows higher difference in direction between M80 and M, consequently assimilating M80 measurements is less efficient in correcting model errors in direction at M location. At FP location, CFD simulations with assimilation also showed reduced difference in wind speeds and directions compared to CFD simulation without assimilation (in figure 5.12a and 5.12b). Hence assimilation with cup measurements at a location improves the prediction of the variability at other mast locations compared with CFD simulation without assimilation. This can be expected from a data assimilation procedure which introduces local information (M80).

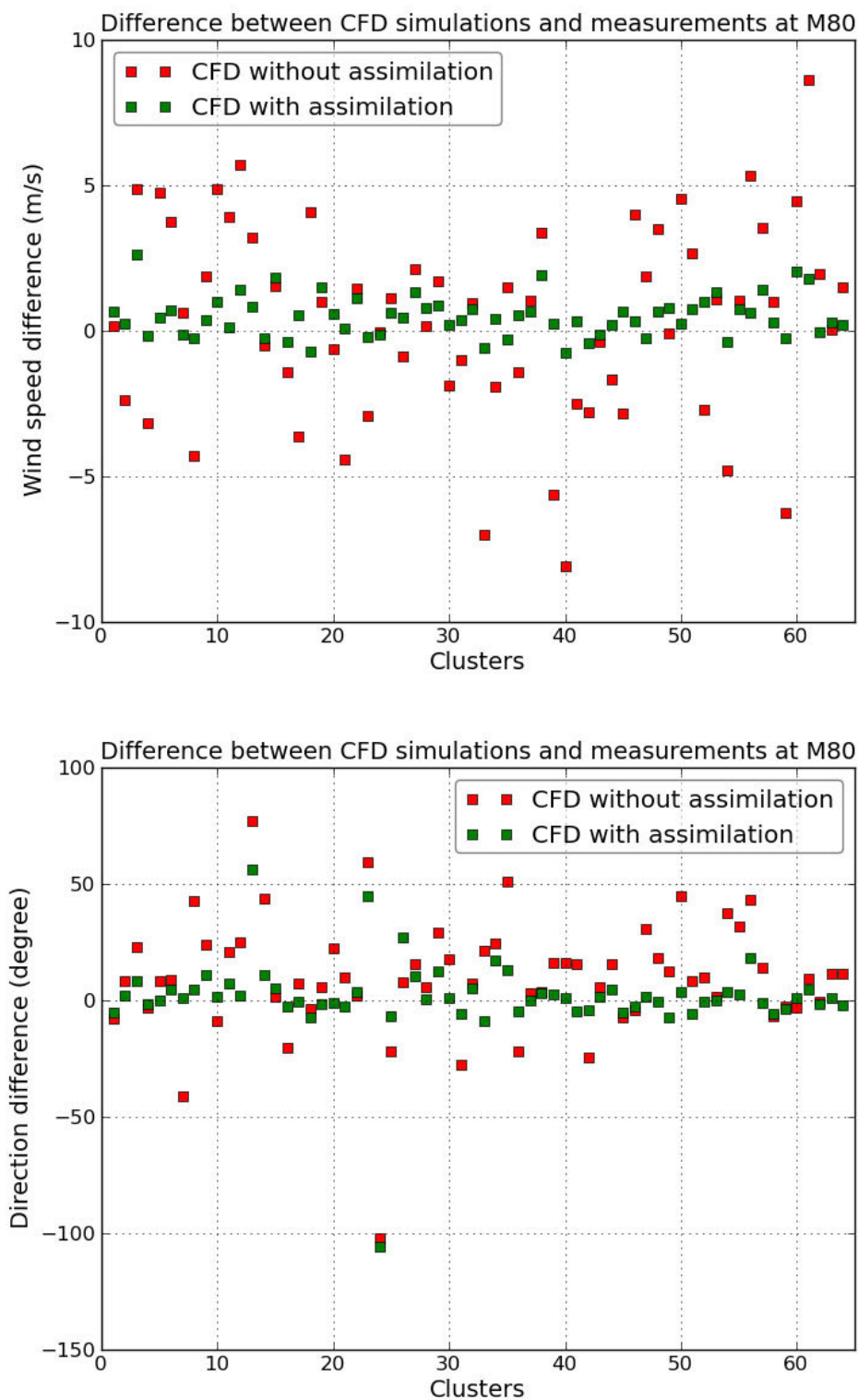


Figure 5.10: Difference between CFD simulations without assimilation and measurements, CFD simulations with cup assimilation and measurement and CFD simulations with sonic assimilation and measurement at M80 (80m) a) wind speed b) direction.

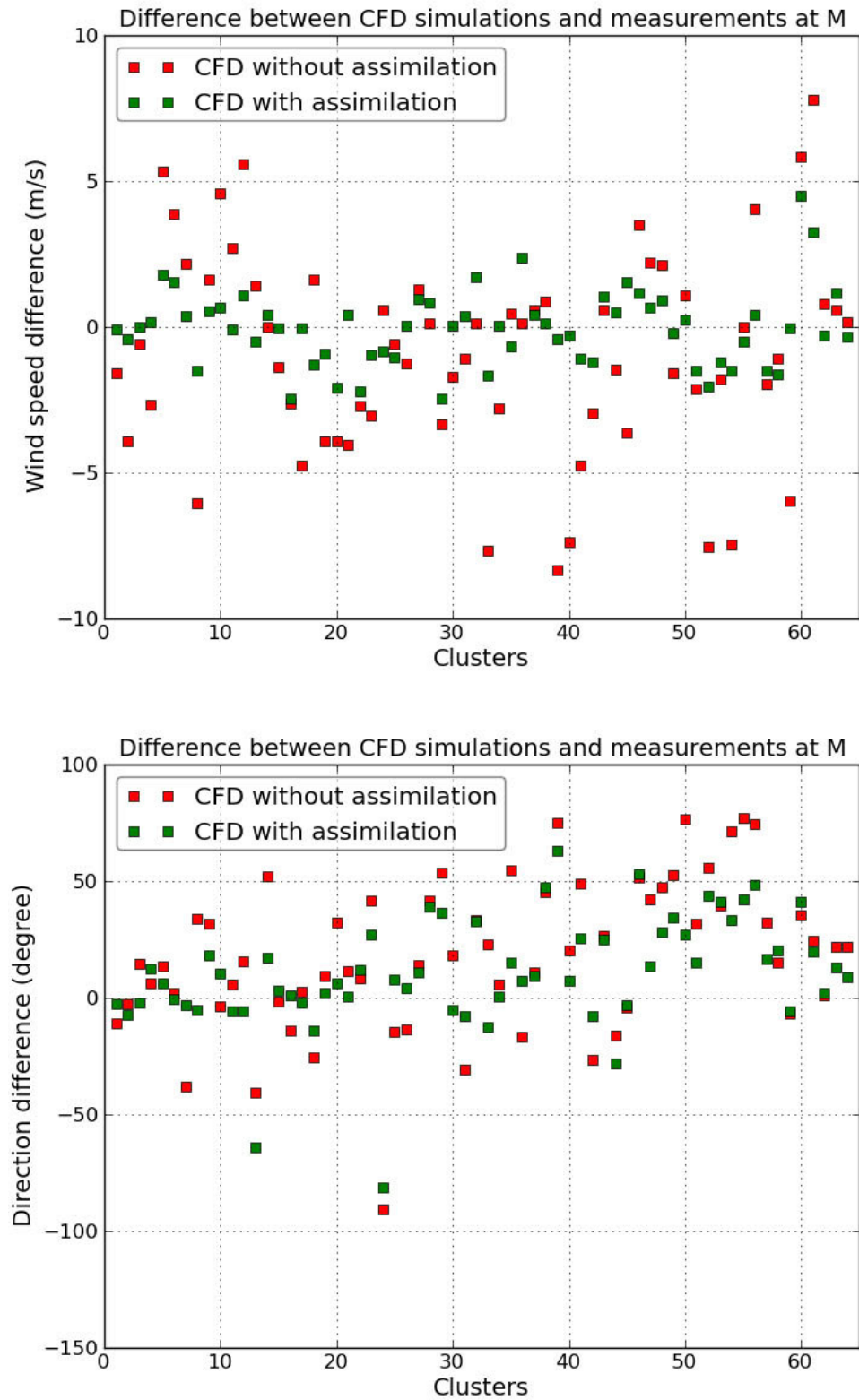


Figure 5.11: Same as figure 5.10 but for M(50m).

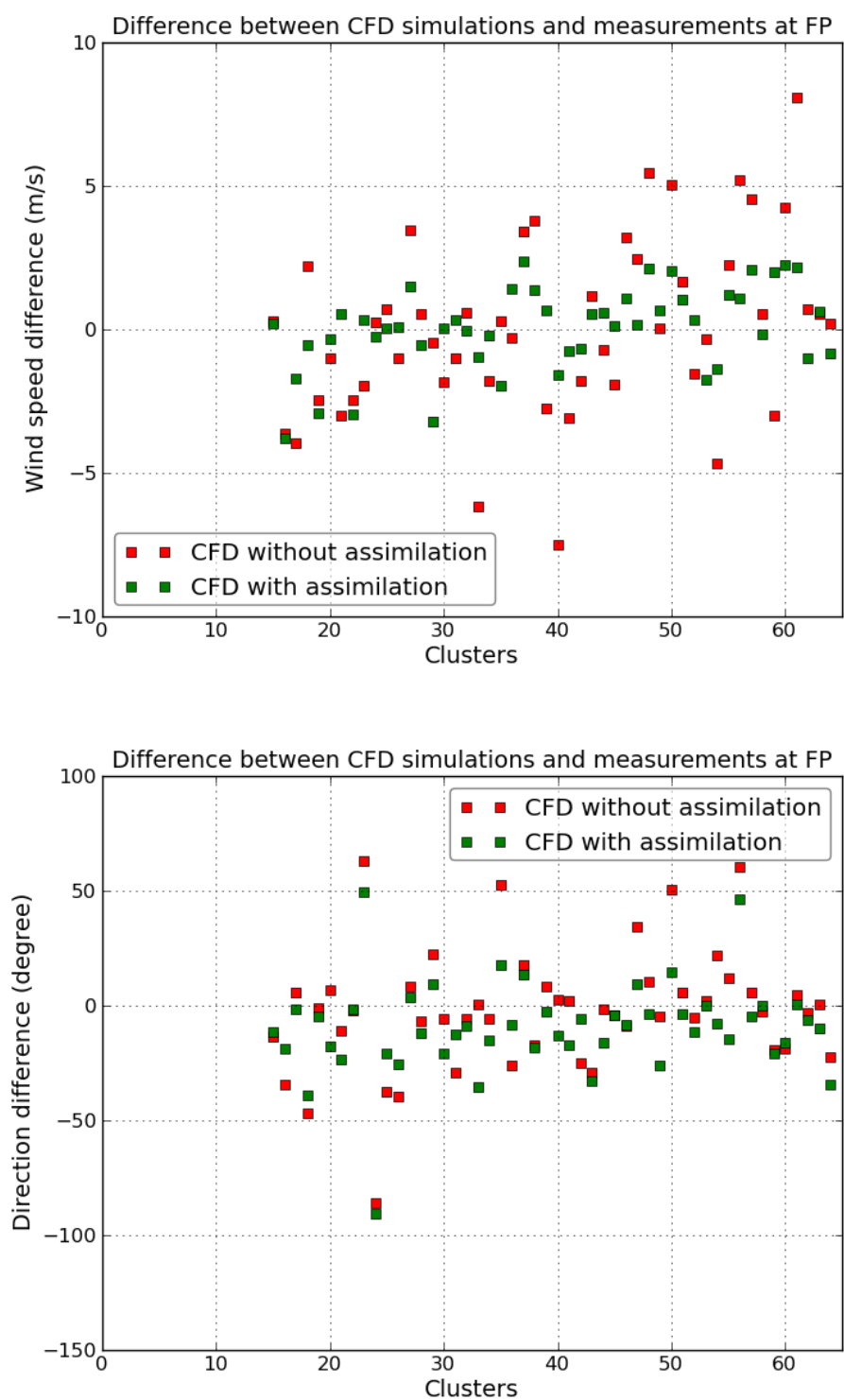


Figure 5.12: Same as figure 5.10 but for FP(50m).

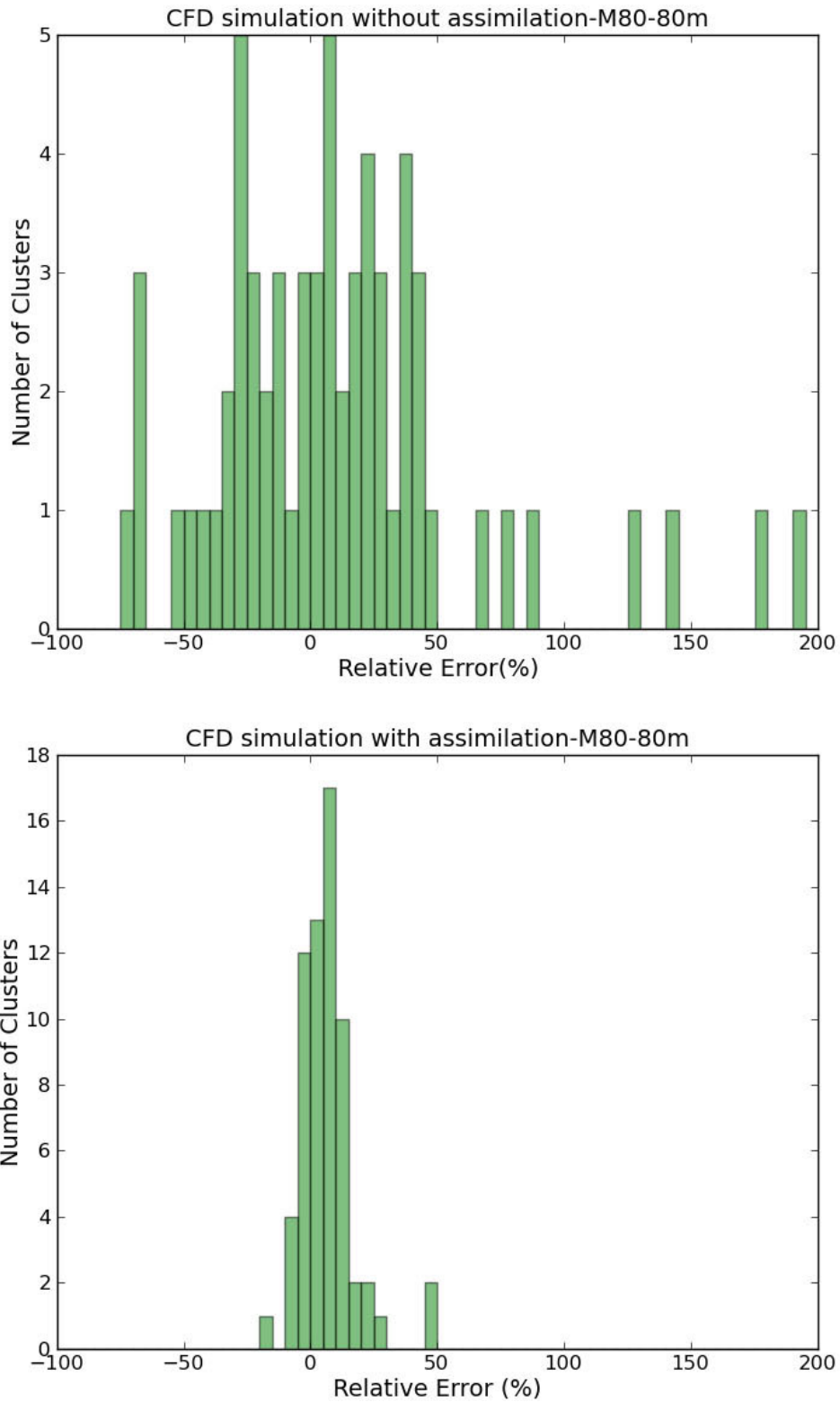


Figure 5.13: Wind speed relative error distribution for the 64 clusters at M80 (80m) location a) CFD simulations without assimilation b) CFD simulations with cup anemometers data assimilation.

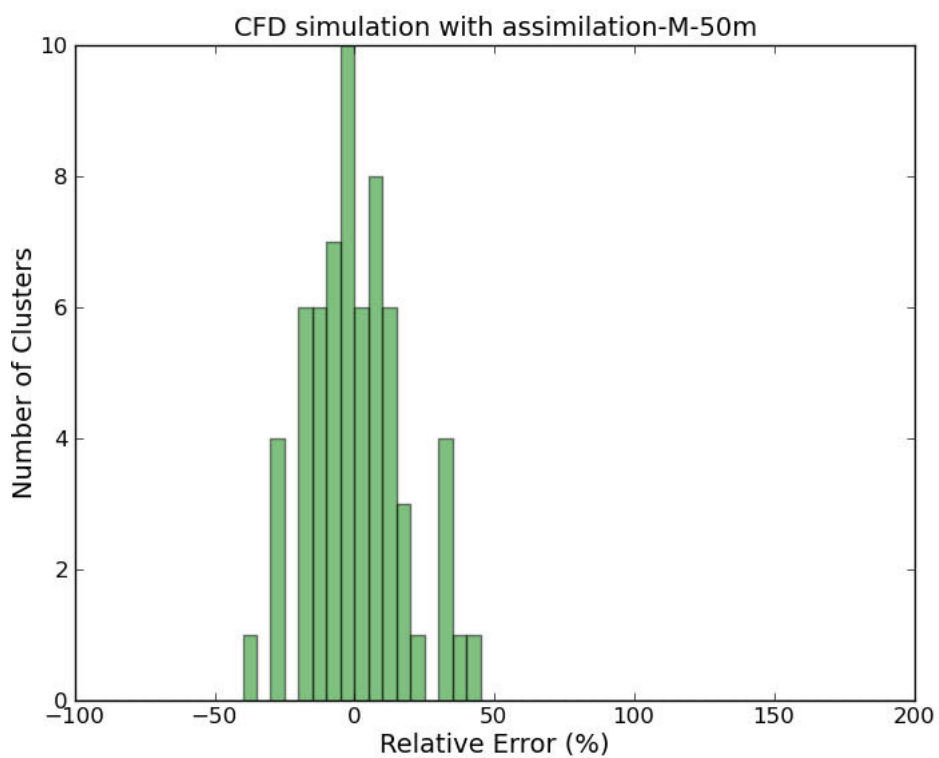
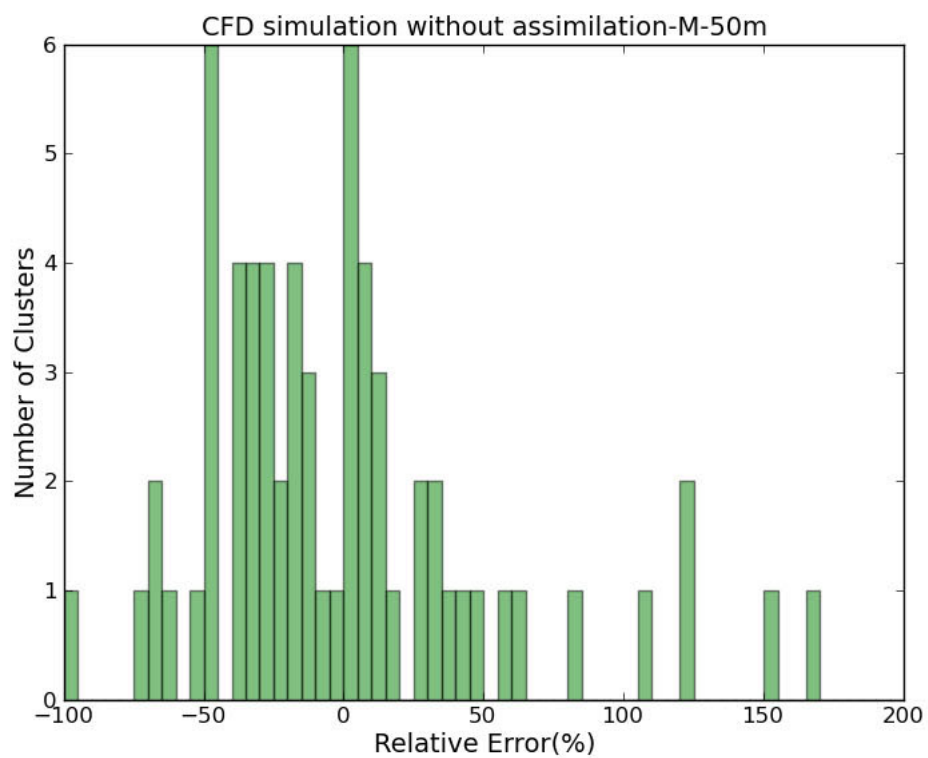


Figure 5.14: Same as figure 5.13 but for M(50m)

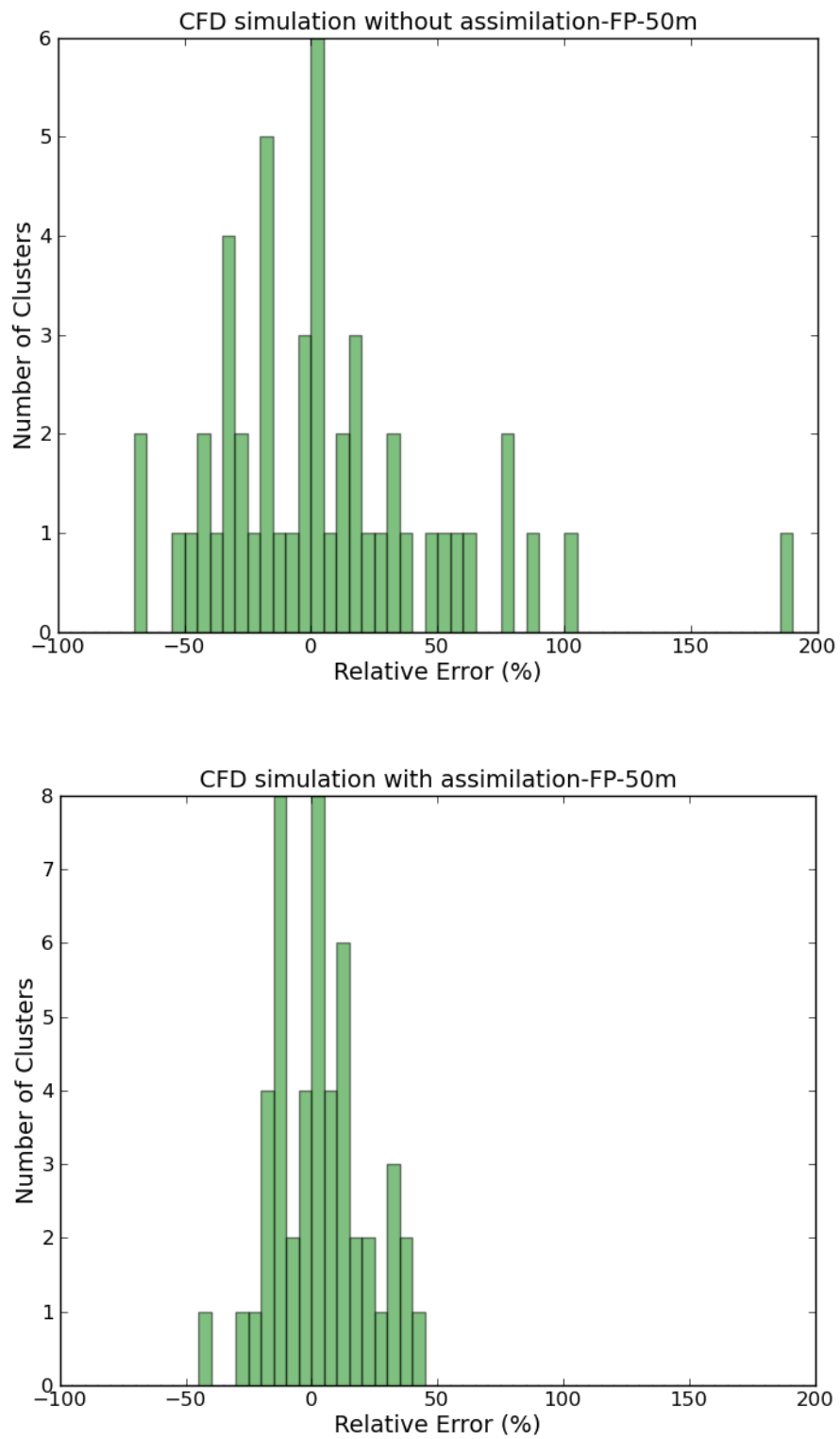


Figure 5.15: Same as figure 5.10 but for FP(50m).

Figure 5.13-5.15 represents the wind speed relative error distribution for the 64 clusters at M80, M and FP mast locations. In the figures 5.13-5.15, (a) represents CFD simulation without assimilation and (b) represents CFD simulation with assimilation. At M80, CFD simulation without assimilation shows high relative error for some situations (up to 200%) (figure 5.13a) and the standard deviation of the distribution is large. Figure 5.13b shows the influence of assimilation at the nudged location (M80), reducing the relative error compared to CFD without assimilation. A maximum relative error of 50% is observed at M80 location and the relative error is within  $\pm 20\%$  for about 75% of the cluster centers. The majority of cluster centers have a positive bias compared to the CFD simulation without assimilation. This positive bias in a majority of cluster centers in CFD simulation with assimilation is related to the strength of the nudging. Too strong nudging results in higher positive bias (not shown in the manuscript) and sensitivity analysis were carried out to minimize the positive bias. For CFD simulation with assimilation, cup measurement were nudged only at 50 m and Cressman spread weight drops rapidly to zero close to the ground. The highest relative errors in both cases correspond to situations with low wind speed of  $\approx 2\text{m/s}$  which are not important for wind energy applications. In some cluster centers CFD simulations without assimilation have predicted very well in comparison with measurements and have slightly higher relative error in CFD simulation with assimilation.

At M and FP location, simulation without assimilation (figure 5.14a and 5.15a) shows higher relative error compared to simulation with assimilation (figure 5.14b and 5.15b). Influence of nudging at M80 location can be noticed at the M and FP mast location in terms of relative error. At M location the CFD simulation without assimilation has relative error within  $\pm 20\%$  for 36% of the cluster centers, and this proportion increases up to 81% using M80 mast data assimilation. The extremes values of error ( $-100\%$  and  $170\%$ ) are reduced to  $-40\%$  and  $45\%$  in CFD simulation with assimilation. At the FP location (figure 5.15a), CFD simulation without assimilation has a relative error within  $\pm 20\%$  for 44% of the cluster centers, while it increases up to 76% with assimilation. The

extreme values ( $-70\%$  and  $190\%$ ) are reduced to  $-45\%$  and  $45\%$  in CFD simulation with assimilation.

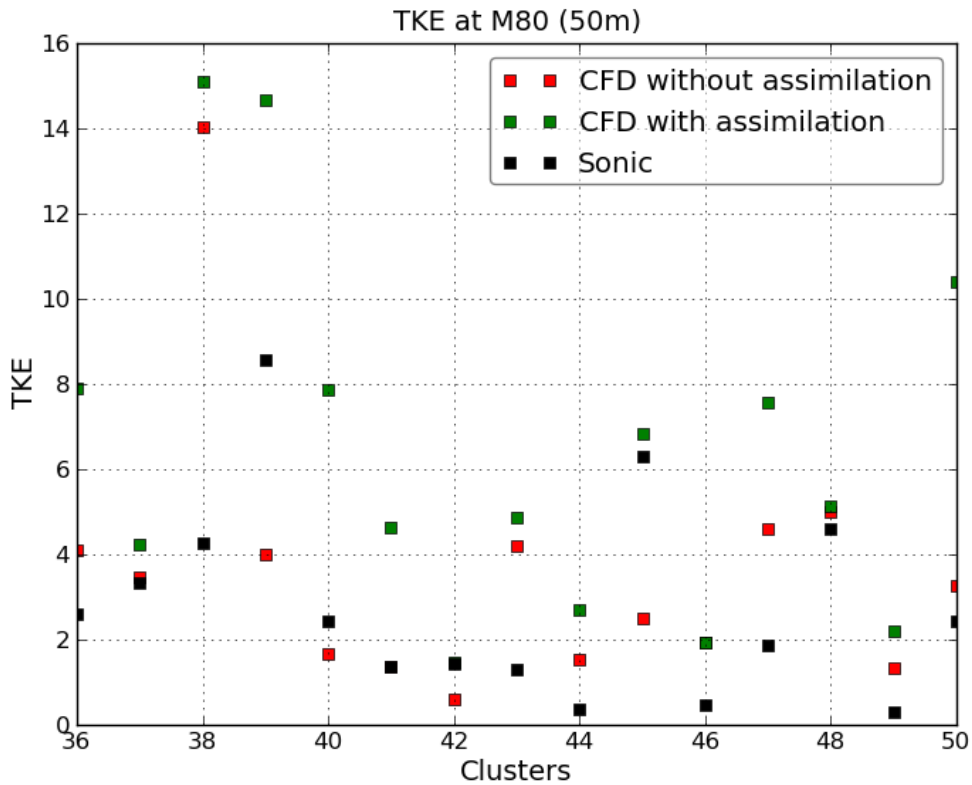


Figure 5.16: Turbulent kinetic energy at M80 (50 m) for CFD simulations without assimilation, CFD simulations with cup assimilation and sonic measurements.

Figure 5.16 show the turbulent kinetic energy (TKE) at M80 location (50 m) for CFD simulation without cup assimilation, CFD simulation with cup assimilation and sonic measurements. Large differences are seen for some cluster centers between the sonic measurements and CFD simulations without assimilation. It should be noticed that TKE from sonic measurements are 10 minutes averaged while TKE from CFD simulations are computed from Reynolds averaged solutions. As the influence of wind speed assimilation, CFD simulation with cup assimilation has predicted higher TKE compared to CFD simulation without assimilation in almost all the cluster centers. This indicate that the assimilation by nudging tends to increase turbulence (which is not currently included in the nudging procedure).

### Calculating yearly averaged wind speeds

After the complete simulation and comparisons with the measurement of the individual clusters, the mean wind speed over the year 2007 is calculated and compared with mean wind speed from measurements, WAsP and Laporte (2008). Two methods are used to calculate the annual mean wind speed as in Laporte (2008). In the first method, we consider that every meteorological situation belongs to a cluster that has the same wind speed as the cluster center wind speed. The wind speed of each of the 8760 hourly situations ( $U(P_j)$ ) is taken as the wind speed calculated for its cluster center  $U(C_i)$ :

$$U(P_j \in cluster_i) = U(C_i) \quad (5.1)$$

$$\bar{U} = \frac{1}{N} \sum_{j=1}^N U(P_j) \quad (5.2)$$

where  $U$  is annual mean wind speed and  $N$  is number of hourly situations.

In the second method, we consider that the wind speed of a situation is a weighted sum of all center wind speeds, the weight is a function of the distance  $r_i$  from the cluster centers and  $W_i$  is the weighting function. This calculates more precisely the wind speeds corresponding to every situation.

$$U(P_j) = \frac{\sum_i W_i U(C_i)}{\sum_i W_i} \quad (5.3)$$

The weighting function suggested by Wendum and Moussafir (1985) is used here:

$$W_i = \frac{e^{-r_i^\beta}}{r_i^\alpha} \quad (5.4)$$

where  $\alpha$ ,  $\beta$  and  $\gamma$  are adjusting constants of the model and default values are used ( $\alpha = \beta = \gamma = 1$ ). This weighting function takes into account all the cluster centers but it quickly decreases outwards such that the contribution of distant cluster center is almost negligible. In Laporte (2008), the first method showed the best results.

Table 5.2 Comparison between the average wind speeds measured at the masts location, WAsP results, Laporte (2008) results and present methodology (CFD simulations without and with assimilation during the year 2007).

	Average over 8760								
	M80-50m	% Error							
<b>Measurement</b>		8.32		8.39		8.09		7.72	
<b>WAsP</b>									
Ref: M mast				9.39	11.9			8.20	6.2
Ref: FP mast				8.40	0.2	6.98	-13.7		
Ref: M80 mast						7.17	-11.4	7.41	-4.2
Laporte (2008)	Centered	7.67	-7.82	8.00	-4.62	7.13	-11.87	7.45	-3.55
Laporte (2008)	Weighted	7,38	-11,28	7,70	-8,26	6,85	-15,31	7,20	-6,68
<b>CFD</b>	Centered	8.39	0.94	8.60	2.53	7.20	-10.96	7.82	1.39
<b>CFD</b>	Weighted	8.47	1.75	8.67	3.33	7.29	-9.90	7.89	2.22
<b>CFD + Nudging</b>	Centered	8.77	5.62	8.99	5.75	8.22	1.65	7.72	0.03
<b>CFD + Nudging</b>	Weighted	8.78	5.52	9.01	7.35	8.24	1.85	7.73	0.12

Table 5.2 shows the annual averaged wind speed over the year 2007 calculated from measurements, WAsP results (which were provided by EDF-EN), previous methodology proposed by Laporte (2008) and current methodology using CFD simulations without and with assimilation for the same site. In WAsP results for each mast two results are available corresponding to the two possible reference masts as input data. The relative error for WAsP ranges from 0% to 14%. In the

previous results of Laporte (2008) using coupling mesoscale and microscale model, the relative error ranges from 4% and 12% (considering the centered average).

In the current methodology, CFD simulation without assimilation (represented as CFD in the table 5.2) shows that the relative error ranges from 1% to 11% (with the centered average which gives the best results also in this computation). At M80 and FP location, CFD simulation without assimilation predicted relative error from 1% to 2% and relative error ranges from 10% to 11% at M location. The current methodology with improved coupling method (Cressman interpolation for the inlet boundary conditions) and fine grid has predicted smaller relative error than in Laporte (2008). In CFD simulations with assimilation (represented as CFD+nudging in table 5.2), the calculated annual averaged wind speed relative error at M80 is about 6%, 1.6% at M and 0.03% at FP. Assimilating M80 cup measurements in CFD simulations has significantly reduced relative error at M and FP compared to CFD simulations without assimilation. The highest relative error (5.75%) is obtained at M80, which is the assimilation location. This is due to the positive bias in majority of clusters introduced by the assimilation. This positive bias in a majority of cluster centers in CFD simulation with assimilation is related to the strength of the nudging. Too strong nudging results in higher positive bias (not shown in the manuscript) and sensitivity analysis were carried out to minimize the positive bias. Overall CFD simulations with assimilation have improved the annual average wind speed at the mast locations.

Figure 5.17 and 5.18 show the annual averaged wind speed and turbulent kinetic energy at 80m above the ground for (a) CFD simulations without assimilation and (b) CFD simulations with assimilation. Wind speed map (in figure 5.17a and 5.17b) shows some difference in the assimilation zone and reduced wind speed downstream of the assimilation zone. Turbulent kinetic energy map (figure 5.18a and 5.18b) shows increased turbulent kinetic energy in the assimilation zone in the CFD with assimilation compared to CFD

simulation without assimilation. This is also shown in the figure 5.16 for the 15 cluster centers in comparison with the sonic anemometer measurements. Assimilating wind speed measurements into the CFD model has increased the turbulent kinetic energy inside the assimilation zone due to larger gradients. It is possible that this effect might be reduced if the turbulence measurements were also introduced in the data assimilation.

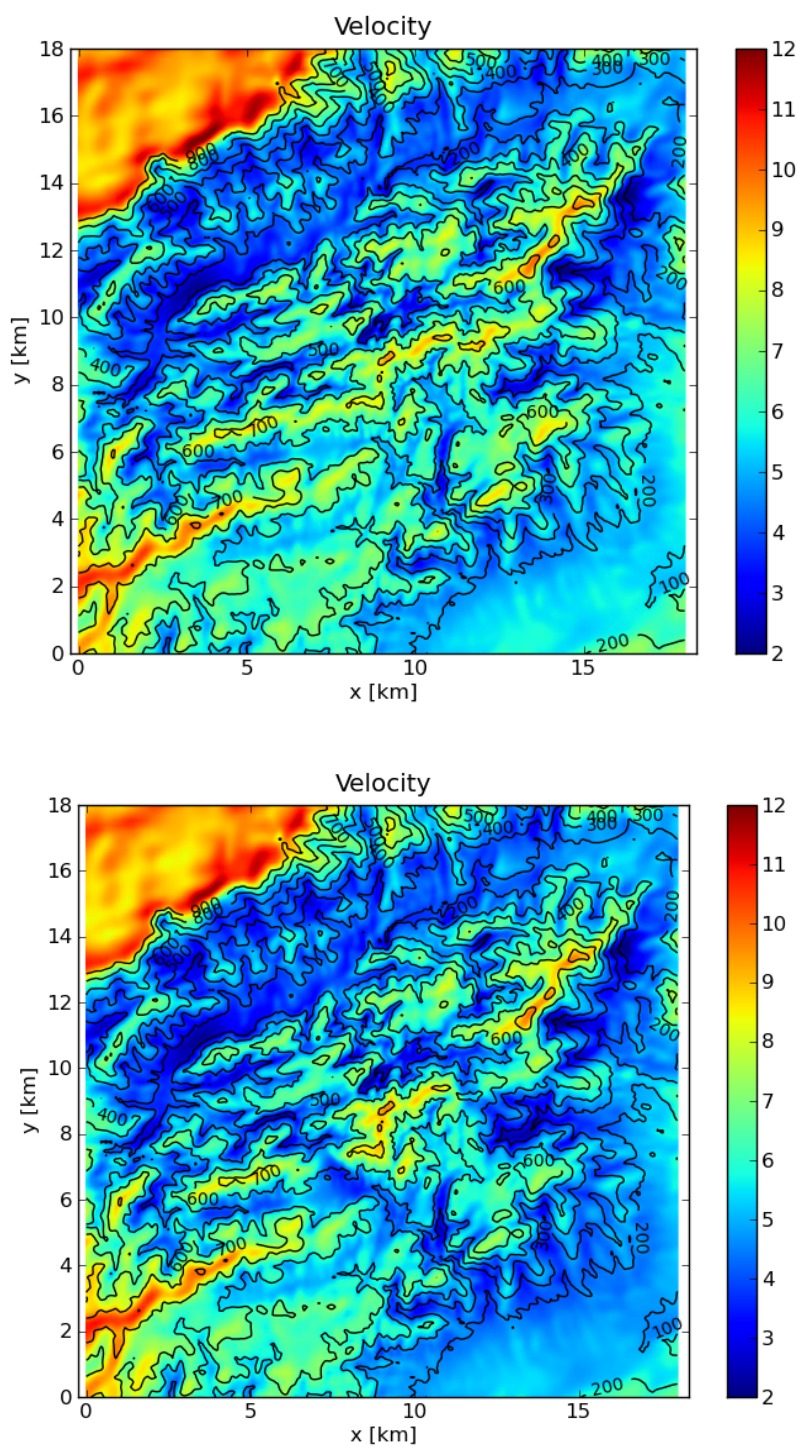


Figure 5.17: Annual average wind speed at 80m above the ground a) CFD simulation without assimilation b) CFD simulation with assimilation

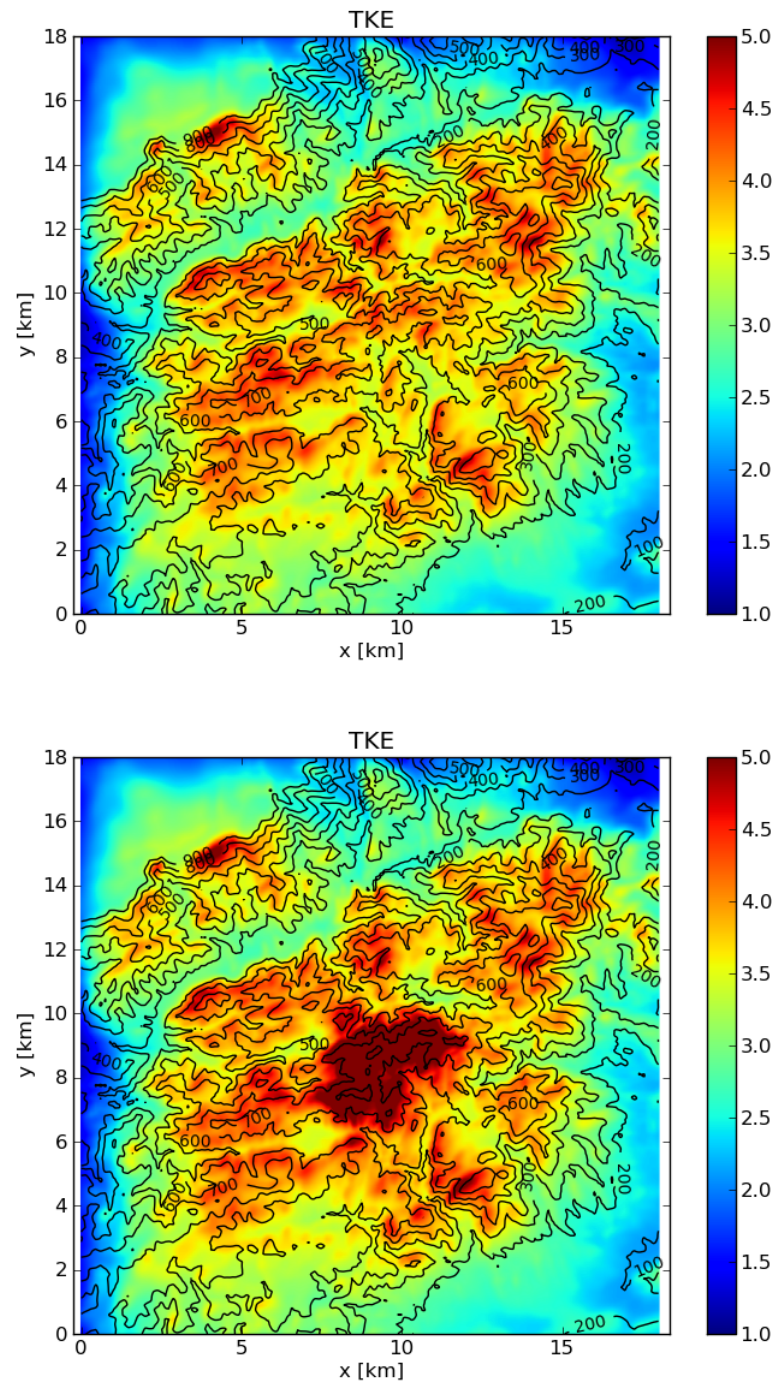


Figure 5.18: Annual average TKE at 80m above the ground a) CFD simulation without assimilation b) CFD simulation with assimilation

## 6. Conclusion and Future work

A new methodology has been developed for improving the prediction of annual average wind speed over a complex terrain using coupled mesoscale and microscale model using field measurements assimilation into the micro scale (CFD) model. To better use all the operational mesoscale model data on the microscale CFD grid, a new coupling method, based on Cressman interpolation of all the vertical profiles surrounding the site, was developed and implemented. This coupling method is applicable for any type of terrain but it provides benefits especially in complex terrain. In this work, it was tested on a very complex terrain in southern France, where field measurements were provided by 3 masts and 2 sodars. To improve further the CFD model prediction a data assimilation technique is used. It uses field measurements data from the site to modify the CFD solution towards the measurements (nudging). The comparison of annual averaged wind speed was carried out for the year 2007 using measurements, WASP results, methodology proposed by [Laporte \(2008\)](#) and current methodology using CFD simulations without assimilation and CFD simulations with assimilation. The models considered in this work were the mesoscale model ALADIN and the open source CFD code Code\_Saturne, but the methodology is applicable to other models.

Sensitivity analyses were carried out for: grid size, determination of the optimum radius of influence for the Cressman interpolation at inlet boundary and testing different coupling methods. Nudging technique was implemented into the CFD model and sensitivity analysis were carried out to optimise the radius of influence of the volumetric Cressman interpolation, nudging coefficient and Cressman spreading function. The sensitivity analyses were discussed in the chapter 4 for a case of northwesterly wind direction:

- Grid independence: Two of the four tested grids are clearly unable to predict the wake characteristics and unable to capture the speed-up on the top of steep slopes. Horizontal resolution of 15 m in the center part of

the domain and vertical resolution of 1,5 m near the ground allow to capture wake characteristics, its influence on the surroundings and predicted wind speed accurately on the top of steep slopes.

- Cressman interpolation (radius of influence sensitivity): Cressman interpolation was developed and implemented into *Code\_Saturne* to impose the operational mesoscale model data on microscale CFD grid. It uses multiple ALADIN profiles to calculate the inlet boundary faces values using weights depending on longitudinal and vertical radius of influence. These two parameters determine the radius of influence of each ALADIN grid point on the inlet boundary face. Sensitivity analysis was carried out with longitudinal radius of 2000, 4250, 8500 and 10500 m and vertical radius of 100 m and 200 m to determine the optimum radii. Longitudinal radius of 8500 m and vertical radius of 100 m were chosen for all the simulations. This sensitivity analysis has to be conducted for every site in case the domain and mesoscale grid are changed.
- Coupling method: Three methods were developed and implemented to impose the operational mesoscale wind profile on microscale CFD grid – translation, extrapolation and Cressman interpolation. Translation and extrapolation use a single mesoscale profile as inlet boundary and results vary depending on the chosen mesoscale grid point. Cressman interpolation takes into account both the horizontal gradients in the mesoscale fields and the influence of topography. Cressman interpolation was used for calculation of yearly average wind speed using CFD simulations.
- Data assimilation: Nudging technique was implemented in *Code\_Saturne*. Measurements from one mast were assimilated (cup or sonic anemometers measurements), and the simulation results were compared to the measurements on two other masts. First, sensitivity

analysis was carried out to determine the optimal longitudinal radius of influence and vertical radius of influence to interpolate sonic  $u$  and  $v$  components using volumetric Cressman interpolation and also for the nudging coefficient (relaxation time). Parameter variations of sonic and cup anemometer data assimilation were analyzed in chapter 5.1. The difference in measurement heights between sonic and cup anemometer requires sensitivity analysis of nudging parameters for the cup assimilation. Importantly, 10 m measurement data is not available in the cup anemometer measurements. In cup anemometer nudging, a vertical radius of influence of 10 m is used, in order to force the Cressman spreading function to be 0 close to the ground. This will only nudge the cup measurements close to the heights where the measurements are available (at 50 m). A larger value of nudging coefficient is necessary for strong forcing in cup measurements assimilation. The large difference between the two values of nudging coefficient used for sonic and cup anemometer nudging is due to the different vertical radius of influence. Hence the CFD model requires different forcing (nudging coefficient) for correcting the CFD solution depending on the type and height of measurement. It underlines the necessity to adapt the nudging parameters to the site configuration (locations of the future wind turbines and of the field measurements).

CFD simulations for northwesterly and southeasterly wind directions using Cressman interpolation for inlet boundary, without and with assimilation were discussed in chapter 4.2. Assimilation of sonic field measurements has modified the wind speed and direction in the assimilation zone in both cases. The results from CFD simulation with assimilation produced very good agreement with measurements at the 3 masts locations.

Annual wind speeds were calculated using the methodology without and with assimilation. Clustering process of the yearly mesoscale data for the site reduces the number of situations necessary to simulate the representation for 1

year. At the nudging location (M80), CFD simulations with assimilation have lower mean average wind speed error and wind direction difference compared to CFD simulations without assimilation for all the 64 clusters. CFD simulations without assimilation have higher difference in wind speed and direction at both nearby (M & FP) masts and good improvements are observed with CFD simulations with assimilation in wind speed and direction.

CFD simulation without assimilation shows high relative error for some situations and the standard deviation of the errors distribution is large. The data assimilation provides a strong reduction of this standard deviation compared to CFD without assimilation. Concerning turbulence, CFD simulation with cup assimilation has predicted higher TKE compared to CFD simulation without assimilation in almost all the clusters centers. It is possible that this effect might be reduced if the turbulence measurements were also introduced in the data assimilation.

The annual averaged wind speed over the year 2007 was calculated from measurements, WAsP results (which were provided by EDF-Energies Nouvelles), previous methodology proposed by Laporte (2008) and current methodology using CFD simulations without assimilation and CFD simulations with assimilation. The relative error for WAsP ranges from 0% to 14%. In previous methodology proposed by Laporte (2008) in which field measurements were not assimilated but were used to correct the ALADIN data imposed at the inlet boundaries, the relative error ranges from 4% and 12%. In the current methodology at M80 and FP mast locations, CFD simulation without assimilation predicted relative error from 1% to 3% and relative error ranges from 10% to 11% at M location. Thus, the current methodology with Cressman interpolation coupling method has predicted the annual wind speed with a smaller relative error than in the previous methodology at 2 of the 3 masts.

In CFD simulations with assimilation the calculated annual averaged wind speed relative error at M80 is about 6%, 1.6% at M and 0.03% at FP.

Assimilating M80 cup measurements in the CFD simulations has significantly reduced relative error at M and FP compared to CFD simulations without assimilation. The highest relative error obtained at the assimilation location is due to the positive bias in majority of clusters introduced by the assimilation. This positive bias, which has been reduced by decreasing the vertical radius of influence, is related to the strength of the nudging. Too strong nudging results in higher positive bias and sensitivity analysis were carried out to minimize the positive bias. Overall CFD simulations with assimilation have improved the annual average wind speed prediction at the mast locations.

Further work should first focus on the introduction of atmospheric stability in this methodology. The CFD code Code\_Saturne is able to take into account thermal stability. However some work is needed in order to include it in the mesoscale-CFD coupling, in order to impose inlet and ground boundary conditions for temperature, which is not an easy task especially in complex terrain. Temperature can also be included in the assimilation process. The influence of turbulence measurements assimilation should also be investigated. Another possible improvement will consist in using a forest canopy model. Such a model has already been tested with success in Code\_Saturne on another site (Zaïdi et al., 2013). Finally, applications on other sites are necessary in order to strengthen the validation of this wind resource assessment methodology.



## References

Abiven, C., Palma, J.M.L.M., Brady, O., 2011: High-frequency field measurements and time-dependent computational modeling for wind turbine siting. *J. Wind Eng. Ind. Aerodyn.*, 99,123-129.

Archambeau, F., Méchitoua, N., Sakiz, M., 2003: Code\_Saturne: A finite volume code for the computation of turbulent compressible flows – industrial applications. *Int. J. Finite Volumes*, 1, 1-62.

Atkinson, B.W., 1981: *Meso-scale Atmospheric Circulations*, Academic Press, 495pp.

Ayotte, K.W., Taylor, P.A., 1995: A mixed spectral finite-difference 3D model of neutral planetary boundary-layer flow over topography. *J. Atmos. Sci.*, 52, 3523-3537.

Ayotte, K.W., 2002: A nonlinear wind flow model for wind energy resource assessment in steep terrain. In *Proceedings of global windpower conference*, Paris, France.

Azad, R.S., 1993: *The atmospheric boundary layer for engineers*, Springer, 574pp.

Badger, J., Hahmann, A., Larsen, X.G., Diaz, A.P., Batchvarova, E., Gryning, S., Floors, R., Jørgensen, H.E., 2011: Comprehensive utilization of mesoscale modeling for wind energy applications. In *Proceedings of European Wind Energy Conference.*, Brussels, Belgium.

Baldwin, B.S., and Lomax, H., 1978: Thin Layer Approximation and Algebraic Model for Separated Turbulent Flows. *American Institute of Aeronautics and Astronautics*, 16<sup>th</sup> Aerospace Sciences Meeting, 78-257pp.

Bechmann, A., Sorensen, N.N., Johansen, J., 2007: Atmospheric flow over Terrain using Hybrid RANS/LES. In Proceedings of European Wind Energy Conference., Milan, Italy.

Beljaars, A.C.M., Walmsely, J.L., Taylor, P.A., 1987: A mixed spectral finite-difference model for neutral stratified boundary layer flow over roughness changes and topography. *Boundary-Layer Meteorol.*, 38, 273-303.

Berge, E., Gravdahl, A.R., Schelling, J., Tallhaug, L., Undheim, O., 2006: Wind in complex terrain. A comparison of WAsP and two CFD-models. In Proceedings of the European Wind Energy Conference, Athens, Greece.

Bitsuamlak, G. T., Stathopoulos, T., Bédard, C., 2004: Numerical Evaluation of Wind Flow over Complex Terrain: Review. *J. Aerosp. Eng.*, 17, 135-145.

Boussinesq, 1877: Theorie de l'écoulement tourbillant. *Memoires presentes par divers savants Acad.Sci.Inst.Fr.*, 23, 45-50.

Bowen, A.J., Mortensen, N.G., Niels, G., 1996: Exploring the limits of WAsP the wind atlas analysis and application program, In Proceedings of the European Wind Energy Conference, Gøteborg, Sweden.

Bowen, A.J., Mortensen, N.G., 2004: WAsP prediction errors due to site orography, Riso National Laboratory, Denmark.

Brower, M.C., 2012: Wind resource assessment: A practical guide to developing wind project. John Wiley & Sons, 296pp.

Burton, T., Sharpe, D., Jenkins, N., Bossanyi, E., 2011: Wind Energy Handbook. John Wiley, 780pp.

Cabezón, D., Iniesta, A., Ferrer, E., Martí, I., 2006: Comparing linear and non linear wind flow models, In Proceedings of European Wind Energy Conference, Athens, Greece.

Calaf, M., Meneveau, C., Meyers, J., 2010: Large eddy simulation study of fully developed wind-turbine array boundary layers, *Phys. Fluids.*, 22, 015110.

Cionco, R.M., Luces, S.A., 2002: Coupled Mesoscale-Microscale model to compute neighborhood scale wind fields, U.S. Army Research Laboratory, White Sands Missile Range, NM 88002-5501.

Cochran, L., Derickson, R., 2011: A physical modelers view of computational wind engineering. *J. Wind Eng. Ind. Aerodyn.*, 99, 139-153.

Coirier, W.J., Kim, S., Marella, S., Mayes, J., Chen, F., Michalakes, J., Miao, S., Bettencourt, M., 2007: Progress Towards coupled mesoscale and microscale modeling capability, CFD Research Corporation, National centre for Atmospheric Research, Bettencourt Consulting, LLC, USA.

Cressman, G.P., 1959: An operational objective analysis system. *Mon. Wea. Rev.*, 87, 367-374.

Dallozzo, 2013: Modélisation d'écoulements atmosphériques stratifiés par large-eddy simulation à l'aide de *Code\_Saturne*, Université Paris-Est, Paris, France, PhD Thesis.

Durrán, D.R., 1990: Mountain waves and downslope winds, Atmospheric processes over complex terrain. American Meteorological Society, Boston, 323 pp.

EWEA, 2009: Wind energy – The facts, Part-1, Technology, Routledge, 488pp.

EWEA, 2010: Wind in power: 2010, European statistics, EWEA report.

EWEA, 2013: Wind in power: 2012, European statistics, EWEA report.

Ferziger, J.H., 1993: Simulation of complex turbulent flow: Recent advances and prospects in wind engineering. *J. Wind Eng. Ind. Aerodyn.*, 46-48, 195-212.

Finardi, S., Morselli, M.G., Jeannot, P., 1997: Wind Flow Models over Complex Terrain for Dispersion Calculations, Pre-processing of Meteorological Data for Dispersion Models, Cost Action 710.

Garrad Hassan <http://www.gl-garradhassan.com/en/index.php>

Ghia, U., Ghia, K.N., Shin, C.T., 1982: High-Re solution for incompressible flow using the Navier-Stokes Equation and a Multigrid method. *Journal of computational Physics.*, 48, 387-411.

GWEC, 2012: Global wind statistics 2012, GWEC.

Hanjalic, K., Kejeres, S., 2008: Some developments in turbulence modeling for wind and environmental engineering. *J. Wind Eng. Ind. Aerodyn.*, 96, 1537-1570.

Haupt, S.E., Zajaczowski, F.J., Schmehl, K. J., 2011: A preliminary study of assimilating numerical weather prediction data into computational fluid dynamics model for wind prediction. *J. Wind Eng. Ind. Aerodyn.*, 99, 320-329.

Hong, S., Lee, I., Hwang, H., Seo, I., Bitog, J., Kwon, K., Song, J., Moon, O., Kim, K., Ko, H., 2011: CFD modeling of livestock odour dispersion over comple terrain, Part I: Topography modeling. *J. Wind Eng. Ind. Aerodyn.*, 108, 253-264.

Ivanell, S.S.A., 2009: Numerical computation of Wind turbine wakes, Phd Thesis, Royal Institute of Technology, Sweden.

Jackson, P.S., Hunt, J.C.R., 1975: Turbulent Wind Flow over Low Hill Quart. J. R. Meteorological Society. 101, 929-955.

Jain, A.K., Murty, M.N., Flynn, P.J., 1999: Data Clustering: review, ACM computing surveys, 31.

Kalnay, E., 2007: Atmospheric Modeling, Data Assimilation and Predictability, Cambridge University Press, 364pp.

Laporte L., 2008: Application d'un code de CFD atmospherique à l'estimation du productible éolien en terrain complexe, PhD Thesis, Université Paris-Est, France.

Laporte, L., Dupont, E., Carissimo, B., Musson-Genon, L., Seclier, C., 2009: Atmospheric CFD simulation coupled to mesoscale analyses for wind resource assessment in complex terrain. In Proceedings of European Wind Energy Conference, Marseille, France.

Launder, B. E., Reece, G. J., Rodi, W., 1975: Progress in the Development of a Reynolds-Stress Turbulent Closure. Journal of Fluid Mechanics., 68, 537-566.

Launder, B.E., Spalding, D.B., 1974: The numerical computation of turbulent flows, Computer Methods in Applied Mechanics and Engineering., 3, 269-289.

Liu, Y., Warner, T., Liu, Y., Vincent, C., Wu, W., Mahoney, B., Swerdlin, S., Parks, K., Boehnert, J., 2011: Simultaneous nested modeling from the synoptic scale to the LES scale for wind energy applications. J. Wind Eng. Ind. Aerodyn., 99, 308-319.

Montes, E., Arnedo, A., Cordon, R., Zubiaur, R., 2009: Influence wind shear and seasonality on the power curve and annual energy production of wind turbine. In Proceedings of European Wind Energy Conference, Marseille, France.

Moussiopoulos, N., 2003: Air quality in cities, SATURN/EUROTRAC-2, subproject final report. Springer, 298pp.

Murakami, S., Mochida, A., Kato, S., 2003: Development of local area wind prediction system for selecting suitable site for windmill. J. Wind Eng. Ind. Aerodyn., 91, 1759-1775.

NREL, 1997: Wind resource assessment handbook, Fundamentals fro conducting a successful monitoring program. Golden, CO, USA, 77pp.

NYSERDA, 2010: Wind resources assessment Handbook, New York state energy research and development authority. NY, USA.

O'Sullivan, J.P., Pecnik, R., Iaccarino, G., 2010: Investigating turbulence in wind flow over complex terrain. Centre for turbulence Research, In Proceedings of the summer program, Stanford University, 129-139.

Oke, T. R., 1987: Boundary Layer Climates. Routledge, 464pp.

Orlanski, I., 1975: A rational subdivision of scales for atmospheric processes. B. Am. Meteorol.Soc., 56, 527–530.

Palma J.M.L.M., Castro F.A., Riberio L.F., Rodrigues A.H., Pinto A.P., 2008: Linear and nonlinear models in wind resources assessment and wind turbine micro-siting in complex terrain, J. Wind Eng. Ind. Aerodyn., 96, 2308-2326.

Philipps, G.T., 1979: A preliminary users guide for the NOABL objective analysis code. Report from science application, Ins., La Jolla, California, USA, 115pp.

Pielke R.A., 1984: Mesoscale Meteorology Modeling, International Geophysics, Academic Press, 676pp.

Politis, E.S., Chaviaropoulos, P.K., 2008: Micrositing and wind turbine classification in complex terrain, In Proceedings of European Wind Energy Conference, Brussels, Belgium.

Porté-Angel, F., Wu, Y., Lu, H., Conzemius, R.J., 2011: Large-eddy simulation of atmospheric boundary layer flow through wind turbine and wind farms. *J. Wind Eng. Ind. Aerodyn.*, 99, 154-168.

Prandtl, 1925: Über die ausgebildete turbulenz. *ZAMM*. 5, 136-139pp.

Probst, O., Cárdenas, D., 2010: State of the Art and Trends in Wind Resource Assessment, *Energies*, 3, 1087-1141.

Qu, Y., 2011: Three-dimensional modeling of radiative and convective exchange in the urban atmosphere, Université Paris-Est, Paris, France, PhD Thesis.

Randerson, D., 1976: An overview of regional-scale numerical models. *Bull. Am. Met. Soc.*, 57, 797-804.

Rodrigo, J.S., Cabezon, D., Lozano, S., Marti, I., 2009: Parameterization of the atmospheric boundary layer for offshore wind resources assessment with limited-length-scale  $k$ - $\epsilon$  model, In Proceedings of European Wind Energy Conference., Marseille, France.

Rodrigo, J.S., Garcia, B., Cabezon, D., Lozano, S., Marti, I., 2010: Downscaling mesoscale simulation with CFD for high resolution regional wind mapping. In Proceedings of European Wind Energy Conference., Warsaw, Poland.

Rodrigues, V., Santos, S., Palma, J., Castro, F., Miranda, P., Rodrigues, A., 2008: Short-term forecasting of a wind farm output using CFD, In Proceedings of European Wind Energy Conference, Brussels, Belgium.

Schlünzen, K.H., 1997: On the validation of high-resolution atmospheric mesoscale models. *J. Wind Eng. Ind. Aerodyn.*, 67 & 68, 479-492.

Schlünzen, K.H., Grawea, D., Bohnenstengel, S.I., Schlüter, I., Koppmann, R., 2011: Joint modelling of obstacle induced and mesoscale changes-Current limits and challenges. *J. Wind Eng. Ind. Aerodyn.*, 99 (4), 217–225.

Sempreviva, A.M., Barthelmie, R.J., Pryor, S.C., 2008: Review of Methodologies for Offshore Wind Resource Assessment in European Seas. *Surv Geophys.*, 29, 471–497.

Smagorinsky, J., 1963: General circulation experiments with the primitive equation. *Monthly weather Review.* 93, 99-165.

Smith, A.M.O., Cebeci, T., 1967: Numerical solution of the turbulent boundary layer equations, Douglas aircraft division report, DAC 33735, McDonnell Douglas, 284pp.

Speziale, C.G., 1998: Turbulence modeling for time dependent RANS and VLES: A review. *Proceedings from the American Institute of Aeronautics and Astronautics.*, 36, 173-184.

Sreevalsa E., 2010: Wind resource assessment, Sari energy

Stauffer, D.R., Bao, J.W., 1993: Optimal determination of nudging coefficients using the adjoint equations. *Tellus* 45A, 358-369.

Stovall, T.D., Pawlas, G., Moriarty, P.J., 2010: Wind farm wake simulations in OpenFOAM. Proceedings from the American Institute of Aeronautics and Astronautics., Florida, USA.

Stull, R.B., 1988: An Introduction to Boundary Layer Meteorology, Kluwer Academic Publishers, 666pp.

Sumner, J.C., Watters, S., Masson, C., 2010: CFD in wind energy: the virtual, multiscale wind tunnel. *Energies.*, 3, 989-1013.

Tammeli, B., Bergstrom, H., Botta, G., Douvikas, D., Hyvonen, R., Rathman, O., Strack, M., 2001: Verification on wind energy predictions produced by WASP and some mesoscale models in European mountains. European Union Wind Energy Conference, Copenhagen, Denmark.

Taylor, P.A., Walmsley, J.K., Salmon, J.R., 1983: A simple model of neutrally stratified boundary layer flow over real terrain incorporating wave number-dependent scaling. *Boundary-Layer Meteorol.*, 26, 169-189.

Tewari, M., Kusaka, H., Chen, F., Coirier, W.J., Kim, S., Wyszogrodzki, A.A., Warner, T.T., 2010: Impact of coupling a microscale computational fluid dynamics model with a mesoscale model on urban scale contaminant transport and dispersion. *Atmospheric Research.*, 96, 656-664.

Troen, I., 1990: A high resolution spectral model for flow in complex terrain. In Proceedings from the 9th symposium on turbulence and diffusion, Roskilde, Denmark.

Troen, I., Petersen, E.L., 1989: European wind atlas. Report from the Risoe national laboratory, Roskilde, Denmark.

Van der Hoven, I., 1957: Power spectrum of horizontal wind speed in the frequency range from 0.0007 to 900 cycles per hour. *Journal of Meteorology* 14:160–1

Versteeg, H., Malalasekera, W., 2007: *An Introduction to Computational Fluid Dynamics: The Finite Volume Method*. Prentice Hall, 520 pp.

Wakes, S.J., Maegli, T., Dickinson, K.J., Hilton, M.J., 2010: Numerical modeling of wind flow over complex topography. *Environmental Modeling & Software.*, 25, 237-247.

Walmsley, J.L., Salmon, J.R., Taylor, P.A., 1982, On the application of a model of boundary-layer flow over low hills to real terrain, *Boundary-Layer Meteorol.*, 23, 17–46.

Wendum, D., Moussafir, J., 1985: Méthods d'interpolation spatiale utilisables pour les variables mesurées en météorologie à moyenne échelle. Rapport technique HE :32-85.22, EDF R&D.

Whiteman, C.D., 1990: Observation of thermally developed wind system in mountainous terrain, *Atmospheric processes over complex terrain*, American Meteorological Society, Boston, USA, 323pp.

Whiteman, C.D., Doran, J.C., 1993: The relationship between overlying synoptic-scale flows and winds within a valley. *J. Appl. Meteorol.*, 32, 1669-1683.

Wilcox, D.C., 1993: *Turbulence Modeling for CFD*, DCW Industries, Inc. 522pp.

WWEA, 2011: World Wind Energy Report 2010, World Wind Energy Association.

Yamada, T., Koike, K., 2011: Downscaling mesoscale meteorological models for computational wind engineering application. *J. Wind Eng. Ind. Aerodyn.*, 99, 199-216.

Zaïdi, H., Dupont, E., Milliez, M., Musson-Genon, L., Carissimo, B., 2013: Numerical simulation of the microscale heterogeneities of turbulence observed on a complex site. *Boundary Layer Meteorology.*, 147, 237-259.

Zdunkowski, W., Bott. A., 2003: Dynamics of the atmosphere: A course in Theoretical Meteorology. Cambridge University Press, 738pp.